

# Electromagnetic compatibility and printed circuit boards

***Citation for published version (APA):***

Horck, van, F. B. M. (1998). *Electromagnetic compatibility and printed circuit boards*. [Phd Thesis 1 (Research TU/e / Graduation TU/e), Electrical Engineering]. Technische Universiteit Eindhoven.  
<https://doi.org/10.6100/IR510999>

***DOI:***

[10.6100/IR510999](https://doi.org/10.6100/IR510999)

***Document status and date:***

Published: 01/01/1998

***Document Version:***

Publisher's PDF, also known as Version of Record (includes final page, issue and volume numbers)

***Please check the document version of this publication:***

- A submitted manuscript is the version of the article upon submission and before peer-review. There can be important differences between the submitted version and the official published version of record. People interested in the research are advised to contact the author for the final version of the publication, or visit the DOI to the publisher's website.
- The final author version and the galley proof are versions of the publication after peer review.
- The final published version features the final layout of the paper including the volume, issue and page numbers.

[Link to publication](#)

***General rights***

Copyright and moral rights for the publications made accessible in the public portal are retained by the authors and/or other copyright owners and it is a condition of accessing publications that users recognise and abide by the legal requirements associated with these rights.

- Users may download and print one copy of any publication from the public portal for the purpose of private study or research.
- You may not further distribute the material or use it for any profit-making activity or commercial gain
- You may freely distribute the URL identifying the publication in the public portal.

If the publication is distributed under the terms of Article 25fa of the Dutch Copyright Act, indicated by the "Taverne" license above, please follow below link for the End User Agreement:

[www.tue.nl/taverne](http://www.tue.nl/taverne)

***Take down policy***

If you believe that this document breaches copyright please contact us at:

[openaccess@tue.nl](mailto:openaccess@tue.nl)

providing details and we will investigate your claim.

# Electromagnetic Compatibility and Printed Circuit Boards

Cover : Top view of HLL demonstration board; magnification 117 percent.  
Designed by Ben Mobach of the University Press Facilities.

# Electromagnetic Compatibility and Printed Circuit Boards

## PROEFSCHRIFT

ter verkrijging van de graad van doctor aan de  
Technische Universiteit Eindhoven, op gezag van de  
Rector Magnificus, prof.dr. M. Rem, voor een  
commissie aangewezen door het College voor  
Promoties in het openbaar te verdedigen  
op donderdag 4 juni 1998 om 16.00 uur

door

Frank B.M. van Horck

geboren te Grubbenvorst

Dit proefschrift is goedgekeurd  
door de promotoren:

prof.dr.ir. P.C.T. van der Laan  
en  
prof.dr. P.J. Degauque

copromotor: dr. A.P.J. van Deursen

CIP-DATA LIBRARY TECHNISCHE UNIVERSITEIT EINDHOVEN

Horck, Frank B.M. van

Electromagnetic compatibility and printed circuit boards / by Frank B.M. van  
Horck. - Eindhoven : Technische Universiteit Eindhoven, 1998.


Proefschrift. - ISBN 90-386-0450-5

NUGI 832

Trefw.: elektromagnetische interferentie / gedrukte bedrading / elektromagnetische  
koppelingen / elektrische afscherming.

Subject headings: electromagnetic compatibility / printed circuits / crosstalk /  
electromagnetic shielding.

In Nature's infinite book of secrecy a little I can read  
*William Shakespeare*

These investigations have been funded by the Dutch Technology Foundation  as project ‘Reliable protection of micro-electronics against electromagnetic disturbances’ under grant ETN11.2508.

The connector work has been partially funded by Berg Electronics B.V. in 's-Hertogenbosch.

# Contents

|  |            |
|--|------------|
| <b>Summary</b>   | <b>vii</b> |
| <b>Samenvatting</b>  | <b>ix</b>  |
| <b>1 Introduction</b>  | <b>1</b>   |
| <b>2 A rapid method for measuring the transfer impedance of connectors</b>                                       | <b>5</b>   |
| 2.1 Introduction . . . . .   | 5          |
| 2.2 Current sensor and actual setup . . . . .  | 7          |
| 2.3 Test of the setup . . . . .  | 9          |
| 2.4 Practical connectors . . . . .   | 13         |
| 2.5 Conclusions . . . . .  | 17         |
| <b>3 Prediction of common-mode currents in cables attached to a PCB by means of a transmission-line approach</b> | <b>19</b>  |
| 3.1 Introduction . . . . .   | 19         |
| 3.2 Low-frequency CM to DM coupling . . . . .  | 22         |
| 3.3 Conducted emission . . . . .   | 25         |
| 3.4 Transmission-line approach . . . . .   | 28         |
| 3.5 Results for bare PCB's . . . . .   | 31         |
| 3.5.1 Straight tracks . . . . .  | 31         |
| 3.5.2 More complicated tracks . . . . .  | 32         |
| 3.5.3 Ground track . . . . .   | 36         |
| 3.6 Demonstration boards with digital logic . . . . .  | 37         |
| 3.7 Additional coupling effects . . . . .  | 40         |
| 3.8 Concluding remarks . . . . .   | 41         |
| <b>4 Crosstalk on a multilayer printed circuit board and the current distribution in the ground plane</b>        | <b>43</b>  |
| 4.1 Introduction . . . . .   | 43         |
| 4.2 Current Distribution and $Z_t$ . . . . .   | 45         |
| 4.3 Mathematical description . . . . .   | 50         |
| 4.3.1 The half space and the infinite plate . . . . .  | 50         |
| 4.3.2 The strip of finite width . . . . .  | 52         |
| 4.3.3 Mutual inductance . . . . .  | 54         |
| 4.4 Influence of a nearby metallic plate on the DM-to-DM crosstalk . . . . .                                     | 54         |
| 4.5 A DM track between two planes . . . . .  | 57         |
| 4.6 High-frequency effects of the crosstalk . . . . .  | 60         |
| 4.6.1 Transmission-line description . . . . .  | 60         |



|          |   |            |
|----------|---|------------|
| 4.6.2    | TL parameters . . . . .                                   | 61         |
| 4.6.3    | Short-circuit case . . . . .                              | 63         |
| 4.6.4    | Characteristic-termination case . . . . .                 | 63         |
| 4.7      | More complicated tracks . . . . .                         | 65         |
| 4.8      | Concluding remarks . . . . .                              | 67         |
| <b>5</b> | <b>Implementation of EMC analysis into a design phase</b> | <b>71</b>  |
| 5.1      | Introduction . . . . .                                    | 71         |
| 5.2      | Global description . . . . .                              | 71         |
| 5.3      | Placement and layout phase . . . . .                      | 72         |
| <b>6</b> | <b>General conclusions</b>                                | <b>75</b>  |
| <b>A</b> | <b>Conformal mapping</b>                                  | <b>77</b>  |
| A.1      | Parallel plates . . . . .                                 | 77         |
| A.2      | Approximate solution . . . . .                            | 78         |
| A.3      | Joukowski transformation . . . . .                        | 81         |
| A.4      | H-field lines for d.c. . . . .                            | 82         |
| A.5      | CM current . . . . .                                      | 82         |
| A.6      | Track between two planes . . . . .                        | 83         |
| <b>B</b> | <b>Electrostatic potential theory and capacitance</b>     | <b>85</b>  |
| B.1      | Analytical treatment . . . . .                            | 85         |
| B.2      | Numerical implementation . . . . .                        | 87         |
| B.3      | Discretization . . . . .                                  | 90         |
| B.4      | Numerical and approximate analytical solution . . . . .   | 94         |
| <b>C</b> | <b>Fourier-transformation techniques</b>                  | <b>95</b>  |
| C.1      | Carson's approach . . . . .                               | 95         |
| C.2      | Ground plane of finite thickness . . . . .                | 96         |
| C.3      | Injection wire between two plates . . . . .               | 97         |
| <b>D</b> | <b>Method of Moments</b>                                  | <b>99</b>  |
|          | <b>Bibliography</b>                                       | <b>101</b> |
|          | <b>List of symbols</b>                                    | <b>107</b> |
|          | <b>Acknowledgement</b>                                    | <b>113</b> |
|          | <b>Curriculum vitae</b>                                   | <b>115</b> |

## Summary

Modern electronic equipment is more and more based on high-speed digital logic. Electrical disturbances from outside the equipment may couple in, predominantly via the attached cables. On the other hand, the high-speed signals inside the device leak partially to the outside environment via the same cables. The relevant coupling mechanisms are analyzed by electromagnetic compatibility (EMC) methods. The goal of the EMC research, described in this thesis, is to study the coupling from a printed circuit board (PCB) to its cables and the environment and to study the crosstalk on the board; by theoretical and experimental methods. The calculations are compared with extensive measurements throughout the thesis. The linear electromagnetic couplings are described by a transfer impedance; the transfer impedance links the disturbing currents and the voltages induced by those currents.

A common-mode (CM) current through a cable may couple into the equipment via the transfer impedance of the connector. In this thesis a new, rapid, and sensitive workbench setup is presented to determine the transfer impedance of connectors.

The generation of a CM current by the differential-mode (DM) circuits on a PCB can also be described by a generalized transfer impedance. The CM circuit is formed by the ground plane of the PCB, a large metallic plane in the vicinity of the PCB, and the cable modeled as a  $150\ \Omega$  impedance. The coupling or crosstalk from one DM circuit on a PCB to another DM circuit is also given by a transfer impedance; the current distribution in the ground plane is important for this coupling. For low frequencies, i.e. when resonances do not show up, simple analytical expressions for the transfer impedances are given. These expressions are valuable to estimate the EMC properties of PCB's. The high-frequency models are based on transmission-line (TL) theory; approximations for the TL parameters considerably speed up the computations.

The rapid and efficient TL method with the analytical expressions can in principle be incorporated into a PCB design program. Such a program should generate warnings when a layout results in a too large CM current.



# Samenvatting

Moderne elektronische apparatuur bevat tegenwoordig steeds meer snelle digitale elektronica. Elektrische storingen van buiten de apparatuur koppelen hoofdzakelijk via de kabels in. Anderzijds zal een gedeelte van de snelle signalen binnen in het apparaat via dezelfde kabels naar buiten koppelen. In het vakgebied elektromagnetische compatibiliteit (EMC) worden de relevante koppelingsmechanismen geanalyseerd. Het EMC-onderzoek beschreven in dit proefschrift heeft als doel de bestudering van de koppelingen tussen een printplaat (Engels: Printed circuit board, PCB) en zijn omgeving enerzijds en de koppelingen op de PCB zelf anderzijds. De analyse is gebaseerd op theorie en experimenten; de berekeningen en de ontwikkelde modellen worden in dit proefschrift geverifieerd aan vele metingen. De lineaire elektromagnetische koppelingen worden gegeven door een transferimpedantie. Deze transferimpedantie geeft het verband tussen de stoorstromen en de geïnduceerde spanningen veroorzaakt door deze stromen.

Een common-mode (CM) stroom door een kabel koppelt o.a. via de transferimpedantie van de connector in. In dit proefschrift wordt een nieuwe, snelle en gevoelige meetopstelling gegeven ter bepaling van de transferimpedantie van connectoren.

Signaalstromen door de sporen van differential-mode (DM) circuits op een PCB met een continu aardvlak wekken via een gegeneraliseerde transferimpedantie een stoorstroom op in het CM-circuit. Dit CM-circuit wordt gevormd door het aardvlak, een groot metalen vlak in de nabijheid van de print en een kabel gemodelleerd als een  $150\ \Omega$  impedantie. De koppeling of overspraak van een DM-circuit op de print naar een ander DM-circuit kan eveneens beschreven worden met een transferimpedantie; de stroomverdeling in het aardvlak is zeer belangrijk voor deze overspraak. Eenvoudige analytische uitdrukkingen voor de transferimpedanties worden gegeven en zijn geldig zolang geen resonantie-effecten optreden. Dit houdt in dat deze uitdrukkingen geldig zijn voor lage frequenties en waardevol zijn voor een schatting van de EMC eigenschappen van PCB's. Berekeningen voor hoge frequenties worden uitgevoerd m.b.v. een transmissielijn-model (TL); benaderingen voor de TL parameters verhogen de snelheid van de berekeningen aanzienlijk.

De snelle en efficiënte TL methode met analytische uitdrukkingen kan in principe geïmplementeerd worden in een PCB ontwerp-programma. Het programma dient te waarschuwen als een layout tot een te grote CM-stroom zal leiden.



# Chapter 1

## Introduction

Electrical and electronic equipment generally emits electromagnetic (EM) fields and is susceptible to external fields. The goal of electromagnetic compatibility (EMC) is (i) to limit the emission of the equipment which should not pollute the environment excessively and (ii) to increase the immunity threshold of equipment. In short EMC should ensure the reliable operation of equipment. According to the IEC (International Electrotechnical Commission), EMC is defined by [IEC90, Section 161-01]

*the ability of an equipment or system to function satisfactorily in its electromagnetic environment without introducing intolerable electromagnetic disturbances to anything in that environment.*

Digital electronics and computers penetrate our society and our economy more and more. The trend of increasing speed of computer hardware and of complexity of the software seems to have begun in earnest. Unfortunately, the increasing speed of (digital) electronics also results in more troublesome EM fields. Furthermore, the submicron technologies on integrated circuits (IC's) require a lower supply voltage of digital logic; approximately 1 Volt in the near future [Dav95]. As a result the noise margin of digital logic decreases; the IC's become more susceptible to external disturbance.

To analyze the emission and immunity problems, some tests have been proposed which more or less represent the actual EM environment. Since January 1996 all electrical equipment put on the European market must satisfy statutory requirements [EEC89]; compliance with the tests and associated standards is one way to meet these requirements. To overcome the emission/immunity problem, a basic knowledge of EMC is necessary; for text books on EMC see e.g. [Ott88, Goe92, Pau92a, Wil96]. These books also give a brief description of the European [Wil96] and American [Pau92a] test methods and standards.

Earlier studies at the Eindhoven University of Technology focused on grounding structures and current flow [Laa87, Hou89, Laa93, Hel95]. The approach turned out to be successful to overcome many practical EMC problems of different complexity and physical size, e.g. from TV electronics to a nuclear plant.

The disturbance current flows in a closed loop (see also Fig. 1.1) and generates interference voltages at the terminals of sensitive equipment. These terminals may be the signal inputs of a device, as well as the power-supply input(s) or the signal outputs of that device. The ratio of the interference voltage at a terminal and the disturbance current is denoted by the term transfer impedance  $Z_t$ ; the fields are assumed weak enough to avoid non-linearity effects. Essentially the method relies on a reduction of  $Z_t$ . Note that the transfer impedance remains meaningful at high frequencies if the disturbance current is considered at the right location.

The counterpart of the transfer impedance is the transfer admittance  $Y_t$  defined as the ratio of the current to a terminal caused by a disturbing voltage. For open structures such as Printed Circuit Boards (PCB's),  $Y_t$  must be included in order to correctly describe capacitive and thereby also resonance effects. We incorporate the current generated by the electrical field into a total transfer impedance  $Z_T$  (closely related to the effective transfer impedance  $Z_{TE}$ , see [Hal92]); again  $Z_T$  is the ratio of the interference voltage at a terminal and the disturbance current.

In this thesis we will apply the  $Z_T$  concept to multilayer printed circuit boards with one continuous ground plane GP. The tracks and the ground plane of the PCB's in electronic systems interconnect the devices or components on the board (see Fig. 1.1). The tracks and the devices form closed loops for the signal currents, a fact which is forgotten by some designers who assume that the currents through the tracks are dumped in a mysterious 'ground'. In EMC terminology the closed signal loops are called the differential-mode (DM) circuits. Cables between PCB's or apparatus are primarily intended to transport DM signals. However, each cable is also a part of a larger circuit which closes via the environment of the PCB (parasitic capacitances in Fig. 1.1) or via ground leads; the large metallic plane below GP in Fig. 1.1 is often a nearby cabinet panel, e.g. in a computer. The current in this circuit is a net current through the cable, the common mode (CM) current in EMC terms. Because of their length, the cables act as efficient antennas for the CM currents, often producing more emission than the PCB itself. This fact is the basis of precompliance EMC tests for emission and immunity; CM currents are measured or injected in cables attached to apparatus or (sub)systems.

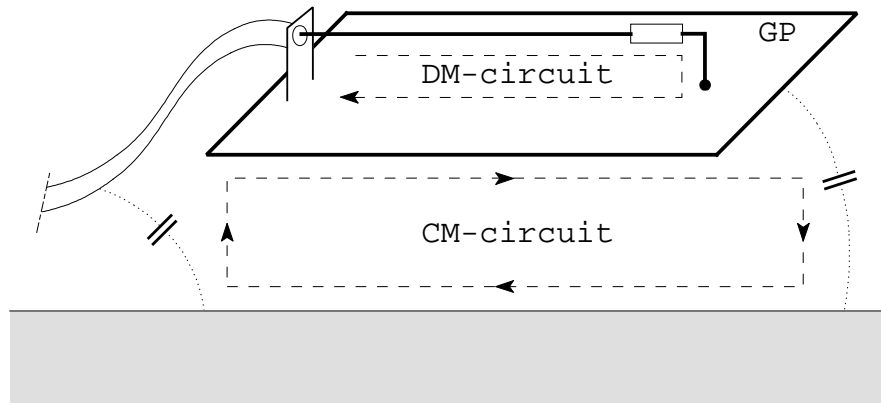


**Figure 1.1.** Differential-mode (DM) and common-mode (CM) definition. The CM current path closes via the ground plane (GP), the cable shield, the parasitic capacitances and the metallic plane below GP.

In addition to the DM-CM and CM-DM coupling, the on board coupling or crosstalk is important from a signal integrity point of view. The current distribution in the GP generated by the DM current through a signal track gives fundamental insight in the crosstalk process and can be used to find the DM-DM transfer impedance  $Z_T(\text{DM-DM})$ .

Our main objective is to study the coupling from DM circuits to the CM circuit and vice versa. The coupling from the tracks often dominates the one from the components. By means of the CM-DM transfer impedance  $Z_T(\text{CM-DM})$  we find the voltage induced over a sensitive terminal on the PCB as a result of the injected CM current. This CM current also

flows through the shield of the connector attached to the cable. Therefore, the  $Z_T$  of the connector and the cable must also be considered, although for a good connector correctly mounted on the board, the  $Z_T(\text{CM-DM})$  of the board will be greater than the  $Z_T$  of that connector.

In chapter 2 a new small and inexpensive workbench setup is given to measure the transfer impedance of shielded connectors. Chapter 3 continues with the couplings from a multilayer PCB to the environment and concentrates on the CM current caused by DM currents through the tracks on the board. A practical rule-of-thumb will be given for the maximum permissible CM current. The developed models and calculations are verified by measurements. The crosstalk and the current distribution in the ground plane are studied in Chapter 4; the theory is again verified by measurements. The investigations in this chapter indicated the importance of the indirect DM to CM to DM coupling, i.e. a DM current induces a current in the CM circuit formed by the GP and return path far away, this CM current in turn induces a disturbing voltage in another DM circuit on the board. The models of Chapters 3 and 4 are well suited for implementation already during the design phase of a product. In Chapter 5 we describe briefly how a possible implementation could be done in practice.

A major part of this thesis has been published earlier as EUT (Eindhoven University of Technology) reports [Hor96a, Hor97a]. These reports showed the chronological progress of the work. The two reports were later rewritten as two articles which have been submitted to the *IEEE Transactions on Electromagnetic Compatibility*; Chapters 3 and 4 give these papers where the numbering of sections etc. has been changed in order to conform to the format of this thesis and where some text has been slightly changed. Chapter 2 presents the research performed for Berg Electronics; the contents of this chapter has been accepted for publication in the *IEEE Transactions on Electromagnetic Compatibility*.





# Chapter 2

## A rapid method for measuring the transfer impedance of connectors

### Abstract

An inexpensive, simple, and sensitive workbench setup has been developed to determine the transfer impedance  $Z_T$  of shielded connectors. The injection current is measured by an inductive sensor integrated in the setup. The induced voltage is determined by a spectrum/network analyzer. The overall sensitivity is  $3\ \mu\Omega$ ; the frequency range is up to 1 GHz. No special calibration samples are needed. As a demonstration the  $Z_T$  is measured for both a coaxial tube with a small hole in the shield which provides a mutual inductance of 0.1 pH, and for some common connectors. Improvements in the design of the shield of a telecommunication connector are presented.

### 2.1 Introduction

The quality of a shielded connector can be characterized by a transfer impedance  $Z_T$ . See Szentkuti [Sze92] for a short overview of the  $Z_T$  concept applied to cables and connectors and Halme [Hal92] for an overview of several methods in accordance with standardization documents. Commonly used are the matched-triaxial method and the line-injection method, see also [Hal92, Sze92]. These methods are not well suited to quickly judge improvements in the prototype of a small high-frequency (HF) connector under development, since the construction of the setup is time consuming. The primary incentive of this work was the need for a rapid, simple, accurate, and sensitive method to judge changes in prototypes of small shielded twin lead telecommunication connectors which can be stacked into large arrays on printed circuit boards [Hor96c]; the requested upper frequency was 1 GHz.

Figure 2.1 shows a schematic side view and top view of our setup. A common-mode current  $I_{CM}$  is injected from the left into the shield of the connector under test (DUT). The current path continues in a folded plate (1 mm brass) which acts as an inductive current sensor (via the flux through the hatched surface), and returns via the brass base plate of the setup.

In our setup both the common-mode current  $I_{CM}$  over the connector shield and the resulting differential-mode voltage  $V_{DM}$  generated between the inner lead and the shield are measured directly. The transfer impedance  $Z_T$  follows from the relation

$$Z_T = \frac{V_{DM}}{I_{CM}}. \quad (2.1)$$

---

A patent for this method has been filed.

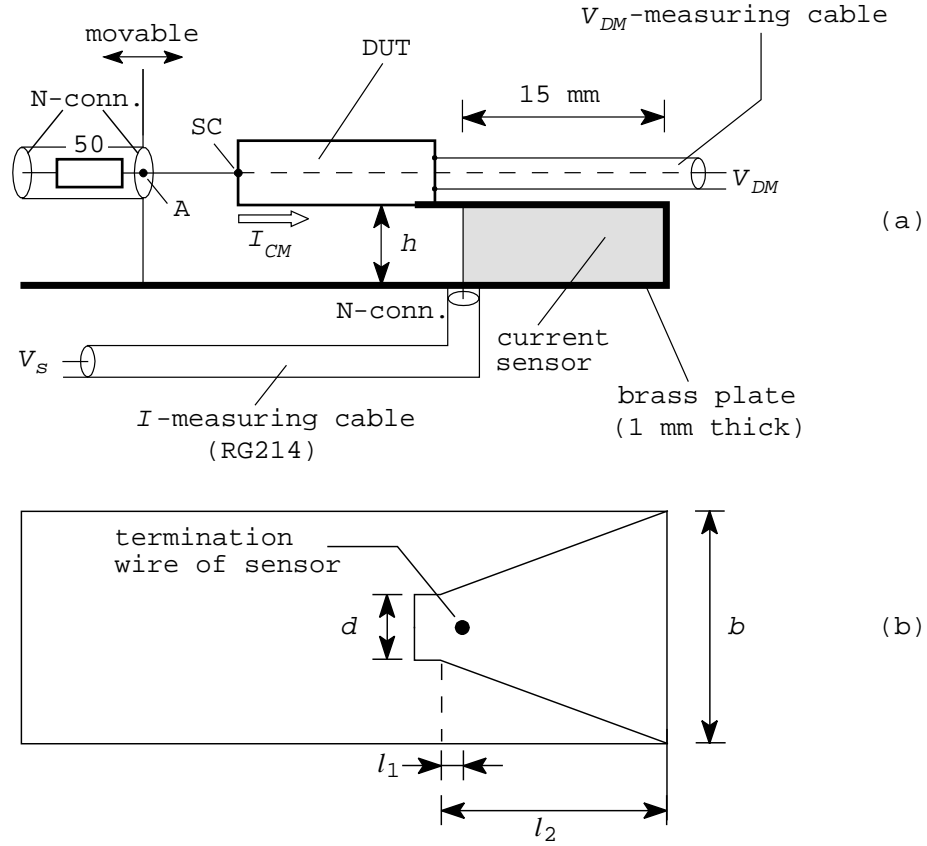


**Figure 2.1.** a) Schematic side view of the setup; the horizontal and vertical dimensions are not proportional for clearness. The current  $I_{CM}$  generated by the tracking generator of a spectrum/network analyzer, is injected at the left and flows through the shield of the connector (device) under test (DUT); the generator is protected by the 50  $\Omega$  series resistor between two N-connectors (see also Figs. 2.4 and 2.5). The injection current returns through the inductive current sensor (flux in the hatched area) and the base plate. The inner conductor(s) of the DUT is (are) shorted to the shield at the left (SC). A short coax cable with low  $Z_T$  (e.g. semi-rigid) carries the generated differential-mode signal  $V_{DM}$  to the measuring equipment (see also the perspective view in Fig. 2.4). The current sensor output  $V_s$  is also measured by the network analyzer. b) Top view of the sensor, with dimensions  $b$ ,  $d$ ,  $l_1$ , and  $l_2$ .

The sensitivity of the current sensor can be calculated from the dimensions or can be directly measured (Section 2.2); this has to be done only once. Test connectors are easily exchanged. No matching impedances, or estimates of injection losses are required as in the triaxial or line-injection method.

Due to the proximity of the base plate, the current distribution over the DUT is concentrated at the lower part of the shield; as in the line-injection method where the current concentration is even more pronounced. In the triaxial setup the injected current is homogeneously distributed over the connector shield. However, even there a rectangular cross-section of the DUT causes  $I_{CM}$  to concentrate at the edges. The line-injection method and the triaxial method can be regarded as extreme cases concerning their  $I_{CM}$  distribution; the method we propose is an intermediate case. The  $Z_T$ 's obtained by the three methods, or at different orientations in a single setup, can be compared, but only with great care.

Our method measures directly  $Z_T$  up to 1 GHz, if the total length between point A and

the rightmost end of the current sensor is smaller than about 3 cm (see Fig. 2.1). For larger lengths, higher frequencies or materials with larger relative permittivity  $\varepsilon_r$ , wavelength effects become prominent (see also Section 2.3 at the end). At still higher frequencies resonances show up [Hal88, Sze92]. To avoid these effects, the circuits for current and voltage measurement must be terminated properly; Eicher and Boillot [Eic92] measured  $Z_T$ 's of cables up to 20 GHz by means of the (matched) line-injection method. Nevertheless, our method suits relative measurements very well since often improvements in the shield of a connector can already be seen below 1 GHz, and will remain effective in the multi-GHz range.

Details of the current measurement are discussed in Section 2.2. An EMC cabinet around the setup reduces interference in the measuring equipment. A tube with a small hole [Hoe88, Hoe91] demonstrates both the correct operation (Section 2.3) and the high sensitivity of a few  $\mu\Omega$ . Results for single or multi-pin connectors are shown in Section 2.4, in terms of relative or absolute measurement of  $Z_T$ .

All measurements were performed with an HP4396A spectrum/network analyzer with two low-noise inputs (0.13  $\mu\text{V}$  or -125 dBm at 10 Hz bandwidth), a reference input and a tracking generator output (+20 dBm). For the calibration a 300 kHz-1.82 GHz S-parameter set was used.

## 2.2 Current sensor and actual setup

The inductances in the circuit model of Fig. 2.2a represent the current sensor (flux area hatched in Fig. 2.1a) with mutual inductance  $M$

$$M \approx \mu_0 \frac{l_2 h}{b - d} \ln \frac{l_2}{l_1 + \frac{d}{b}(l_2 - l_1)}, \quad (2.2)$$

in which  $h$  the height of the sensor (Fig. 2.1). The output impedance of the sensor, seen at the N-connector, is a self inductance  $L$ . In the  $Z$ -representation [And67] of Fig. 2.2b the impedances are  $Z_{21} = j\omega M$  and  $Z_{22} = j\omega L$ . The injected current follows from the relation

$$I_{CM} = \frac{R + j\omega L}{j\omega M R} V_s, \quad (2.3)$$

where  $V_s$  is the measured voltage from the sensor and  $R$  represents the 50  $\Omega$  characteristic termination of the sensor cable at the network analyzer. The inductances  $M$  and  $L$  are characteristics of the sensor only and have to be determined once. The impedance  $Z_{11}$  in Fig. 2.2b depends on the layout of the injection circuit and includes the 50  $\Omega$  protection resistor;  $Z_{11}$  does not influence the current measurement as it merely presents an additional load to the generator.

A typical sensor had dimensions  $l_1 = 5$  mm,  $l_2 = 15$  mm,  $b = 50$  mm,  $d = 10$  mm, and  $h = 4$  mm (see Fig. 2.1). The impedances  $Z_{21}$  and  $Z_{22}$  were measured with an S-parameter set (Fig. 2.3, see also [Hor96c]); for this measurement the 50  $\Omega$  protection resistor was removed.

We obtained  $L = 5$  nH and  $M = 1.56$  nH, in good agreement with Eq. (2.2) which gave  $M = 1.4$  nH. For other current sensors, the maximum deviation in  $M$  was  $\pm 20$  percent.

The length of the sensor is maximally 1.5 cm. If the total length of the DUT and the sensor is less than approx. 3 cm, transmission-line (TL) effects can be neglected up to 1 GHz in the CM circuit. The wave impedances of the connector and of the  $V_{DM}$ -measuring cable

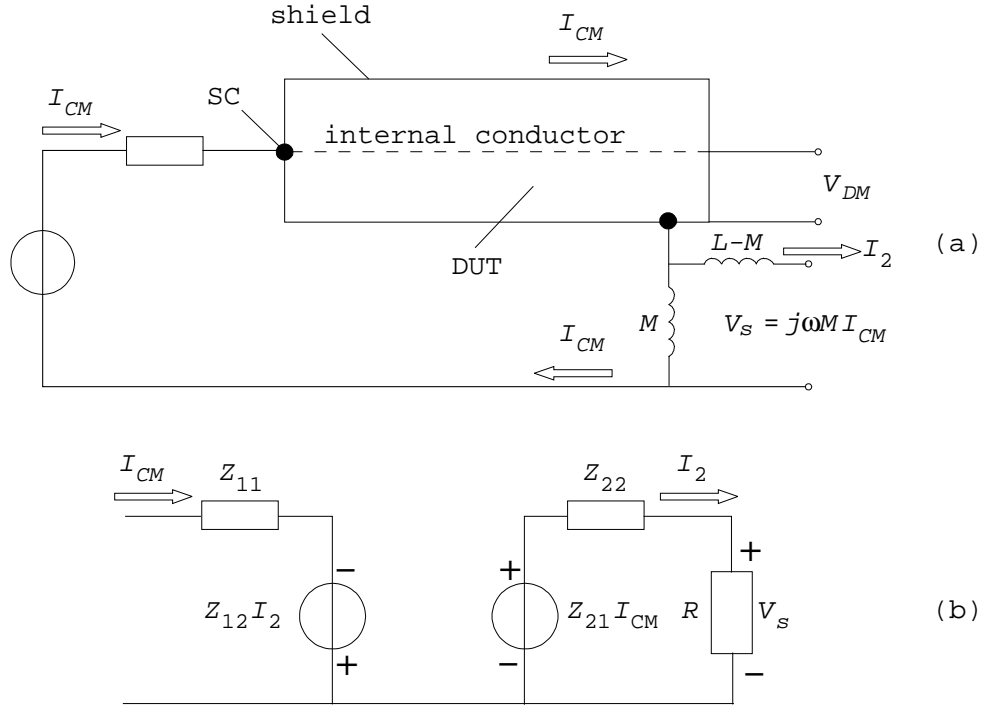


**Figure 2.2.** a) Schematic diagram of the  $Z_T$  measurement setup shown in Fig. 2.1. The internal conductor is short circuited (SC) against the shield at injection side. The common-mode current  $I_{CM}$  is measured by means of a current sensor represented by the two coils. The differential mode voltage  $V_{DM}$  generated is measured directly. b)  $Z$ -representation of the sensor.

(terminated into  $50\ \Omega$ ) are generally not matched. However, for a DUT of 1.5 cm length with a standard dielectric such as teflon ( $\epsilon_r = 2.25$ ), TL effects can be neglected up to 1 GHz. This was verified by experiments. High  $\epsilon_r$  materials may require a closer look.

We first tested the open setup of Fig. 2.1a without any test connector. The current injection pin (A in Fig. 2.1a) was directly connected to the sensor. A short circuited DM-measuring cable (double braid RG223) was also connected there. All cables between the setup and the network analyzer were about 0.5 m long. With this open structure, the injection current generated a CM current over the cables. The resulting DM voltage at the network analyzer was mostly due to the transfer impedance of the input modules of the analyzer. The overall  $Z_T$  was dominantly inductive, equivalent to 0.4 pH or 2.5 m $\Omega$  at 1 GHz. This open setup still allows to test connectors with appreciable  $M$ .

To lower the  $Z_T$  threshold, the setup was placed in a brass EMC box (Fig. 2.4); a commercial steel lid was in good contact with the box. The shields of both the current injection input and the  $V_{DM}$  cable were connected to the box wall over  $360^\circ$ . This compromised the flexibility in mounting samples of different length, but reduced the remaining coupling to less than or equal to the noise level of the analyzer, corresponding to a  $|Z_T|$  of 3  $\mu\Omega$ . A ferrite ring around the  $V_{DM}$  cable inside the box ensured correct operation of the current sensor. A single ring (TR/TRCN-28-16-20) provided a sufficiently high impedance compared to the current sensor over the whole spectral range. This was experimentally demonstrated by a small inductive loop (5 mm  $\times$  10 mm) near the N-connector tube (Fig. 2.5) which measured the current through the cable there. With a ferrite ring the current through the

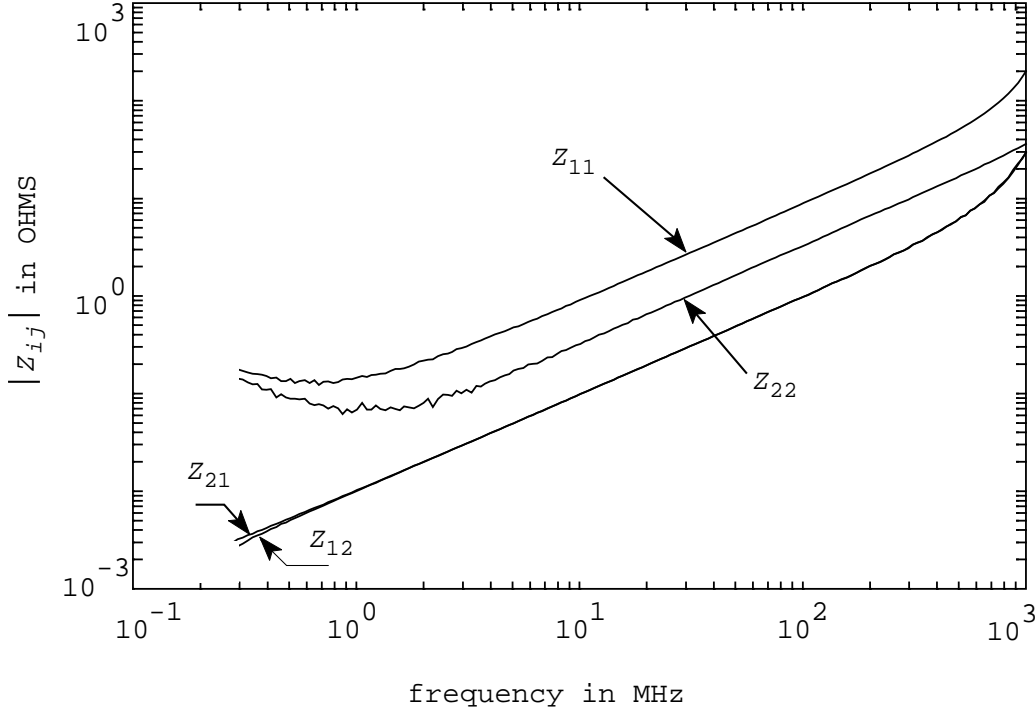


**Figure 2.3.** Measured  $Z$ -parameters of the network given in Fig. 2.2b. The  $50\ \Omega$  resistor is not included in  $Z_{11}$ .

cable was less than -28 dB of the CM current through the tube. Without ring this ratio was about -11 dB; even this resulted in an error of only 27 percent or -11 dB in the CM current measurement.

As another solution which retains the full flexibility of sample mounting, one could install a second ferrite ring around the injection connector and omit the  $360^\circ$  connection of the cable shields. This was not investigated in full detail.

### 2.3 Test of the setup

We tested the setup in the EMC-box with a DUT made of a solid walled brass tube around a central conductor, and a similar tube with one hole as in Fig. 2.4, or several holes in a row; for a side view see Fig. 2.5. The characteristic impedance formed by the central conductor and the inner tube-wall was  $50\ \Omega$ . The tube parameters were: length  $l_t = 3\text{ cm}$ , conductivity  $\sigma = 1.43 \cdot 10^7\ \Omega^{-1}\text{m}^{-1}$ , inner radius  $r_i = 5\text{ mm}$  and wall thickness  $t$  about  $100\ \mu\text{m}$  which slightly varied over the circumference due to machining problems. The single hole radius,  $r_h$ , varied between 0.5 and 2 mm. In this section we only consider the HF part of  $Z_T$ , for the low frequencies see [Hor96c].

The measured and calculated  $Z_T$ 's for a solid walled tube are given in Fig. 2.6. For a homogeneous current distribution the  $Z_T$  is given by [Kad59, Eq. (L.25)]

$$Z_T = R_{DC} \frac{kt}{\sinh kt}, \quad (2.4)$$

where  $R_{DC} = l_t / 2\pi\sigma r_i t$  is the d.c. resistance,  $k = (1 + j)/\delta$ , and  $\delta = \sqrt{2/\omega\sigma\mu_0}$  the skin depth. Measurement and calculation correspond well;  $|Z_T|$ 's down to approx.  $3\ \mu\Omega$  can be

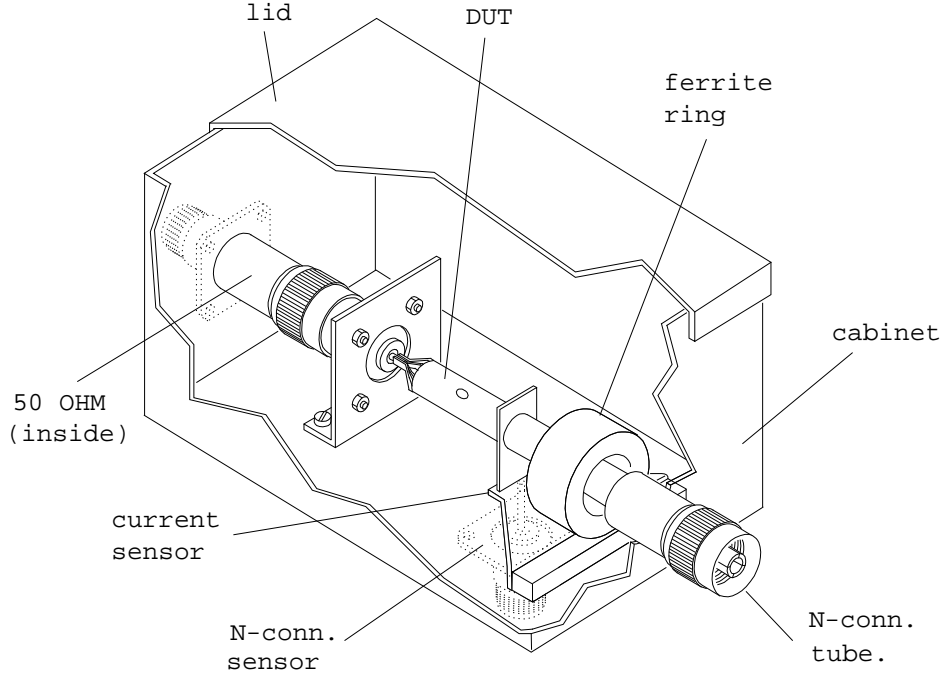


**Figure 2.4.** Perspective drawing of the sensor and tube with a hole as DUT in an EMC-box (1 mm brass plate, dimensions  $120 \times 65 \times 61 \text{ mm}^3$ ); see Fig. 2.5 for a side view. The box is closed by a standard galvanized steel lid with springs around the perimeter. The  $50 \Omega$  resistor is placed between two standard N-connectors; the shields of these connectors were interconnected by a short brass tube around the resistor. The shield of the  $V_{DM}$  cable was also connected over the full perimeter with the box. The ferrite ring around the cable provides a high impedance for the common-mode current.

measured in a single spectral scan of the network analyzer.

In Fig. 2.6 we also present the transfer impedances of a tube with a  $r_h = 0.5 \text{ mm}$  hole at position 1 (Fig. 2.5, hole down) and 2 (hole up). For high frequencies the inductive coupling through the hole becomes dominant. Since the sensor presents a low impedance path for the CM current, the electric field is small around the hole and we may neglect the capacitive coupling. Kaden [Kad59, Eq. (H.188)] gives the mutual inductance  $M_h$  caused by a hole:

$$M_h = \frac{\mu_0 r_h^3}{3\pi^2 r_i^2}. \quad (2.5)$$

Two corrections apply in our case:

a) The proximity of the base plane increases the magnetic field strength under the tube; this results in a larger mutual coupling when the hole is at position 1, and a smaller coupling at position 2. In case of a very wide base plane, neglecting the upright walls or lid, image theory yields the exact field amplification  $A_1$  at position 1 [Ses71, Section 7.3]

$$A_1 = \frac{h_t + r_o}{\sqrt{h_t^2 - r_o^2}}, \quad (2.6)$$

where  $h_t$  is the distance between the axis of the tube and the base (Fig. 2.5) and  $r_o = r_i + t$  the outer radius of the tube. The field amplification factor equals  $A_1 = 1.36$  in our setup with  $h_t = 17 \text{ mm}$  and  $r_o \approx 5.1 \text{ mm}$ . The field attenuation at position 2 is the inverse of this expression.

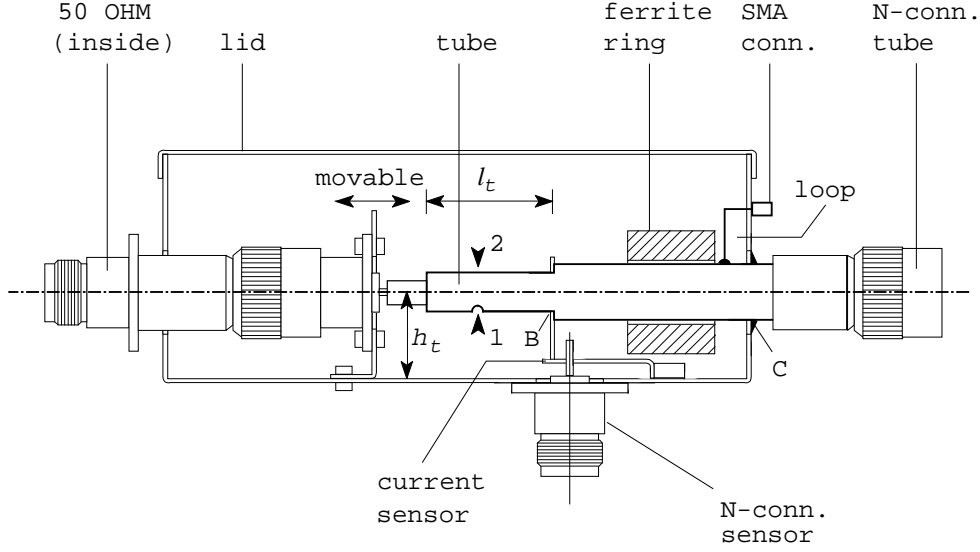


**Figure 2.5.** Side view of the test connector (Fig. 2.4) in the EMC box. The  $V_{DM}$ -measuring cable (see also Fig. 2.1) is connected over its full perimeter to the outside of the box (point C); the N-connector tube is connected to the cable. The inductive loop at the right side in the box of length 5 mm and height 10 mm is terminated into an SMA connector at the outside.

b) For small radii  $r_h$ , the finite wall thickness also reduces  $M_h$ . This so called ‘Kamin dämpfung’ (chimney attenuation) is approximately given by [Kad59, Eq. (H.171)]

$$A_2 \approx e^{-1.84 \frac{t}{r_h}}, \quad (2.7)$$

valid for  $t/r_h > 0.5$ . In a more detailed analysis, McDonald [Don72] obtained a reduction of approximately 16 percent for the magnetic dipole moment which describes the field inside the tube; or,  $A'_2 = 0.84A_2$ . A wall thickness  $t = 0.12$  mm results in  $A'_2 = 0.64$  for a 1 mm hole ( $r_h = 0.5$  mm). For the 4 mm wide hole, Eq. (2.7) is not valid, and  $A'_2$  can be taken equal to unity. Summarized, the mutual inductance  $M_1 = A'_2/A_1$  (hole down) and  $M_2 = A'_2A_1$  (hole up), in which  $A'_2 = 1$  for the 4 mm wide hole.

**Table 2.1.** Measured (m) and calculated (c) mutual inductance for radii 0.5, 0.8, and 2 mm. The positions 1 (hole down) and 2 (hole up) are indicated by subscript 1 and 2. The mutual inductance  $M_h$  is given by Eq. (2.5),  $M_1 = M_h A'_2/A_1$ , and  $M_2 = M_h A'_2 A_1$ , in which  $A'_2 = 1$  for the 4 mm wide hole.

| $r_h$ [mm]/<br>$t$ [mm] | $M_h$ [pH] | $M_1$ [pH] |       | $M_2$ [pH] |      | $M_1/M_2$ |      |
|-------------------------|------------|------------|-------|------------|------|-----------|------|
|                         |            | m          | c     | m          | c    | m         | c    |
| 0.5/0.12                | 0.20       | 0.18       | 0.15  | 0.08       | 0.08 | 2.2       | 1.85 |
| 0.8/0.12                | 0.84       | 0.97       | 0.72  | 0.48       | 0.39 | 2.0       | 1.85 |
| 2.0/0.15                | 13.05      | 17.50      | 17.75 | 7.96       | 9.60 | 2.3       | 1.85 |

Table 2.1 presents the mutual inductances  $M_h$  for both positions and different hole radii; these values were obtained in the frequency range 100-300 MHz. All measured and calculated



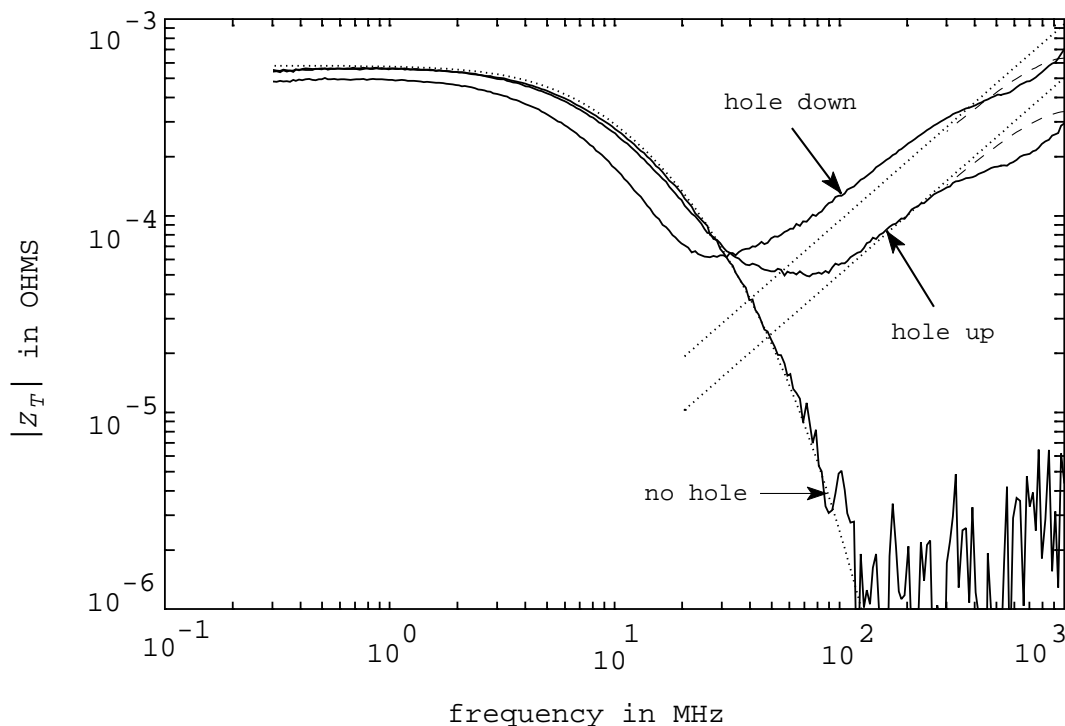


**Figure 2.6.** Measured  $Z_T$ 's for tube with and without a hole ( $r_h = 0.5$  mm). The theoretical high-frequency coupling is given by dotted straight lines and are calculated by means of the values given in Table 2.1. The corrected theoretical HF coupling is shown by (- - -), see main text.

$M$  values agree to within 25 percent. The largest deviations occur for the smaller holes. In our opinion this is mainly due to the uncertainty in  $A_2$ .

Practical connectors have often much larger  $Z_T$ 's than those discussed up to now. Therefore, we also tested the setup for a tube with three 4 mm wide holes facing down and three 4 mm wide holes facing up; the distances between the holes were 8 mm. The theoretical inductive mutual coupling equals 82.05 pH ( $= 3 \cdot (M_1 + M_2) = 3 \cdot (17.75 + 9.6)$ ); this coupling is equivalent with a  $|Z_T|$  of approx.  $0.5 \Omega$  at 1 GHz. The measured  $M$  was 85 pH, in a good agreement with the calculation; no direct interaction between the holes was assumed.

At 1 GHz the measured  $Z_T$  (hole up) is 6 dB lower than the calculated transfer impedance (dotted straight lines in Fig. 2.6). Since the total length of our tube and connector is approx. 5 cm, TL effects showed up. In an analysis we represented the tube by a 3 cm long TL with characteristic impedance  $Z_0 = 60 \operatorname{arccosh}(h_t/r_o) = 112 \Omega$  terminated with a (estimated) self inductance  $L_s \approx 15$  nH seen at point B (Fig. 2.5), the connection of the tube to the sensor; the source was modeled by an ideal voltage generator with impedance  $100 \Omega$  ( $50 \Omega$  of the tracking generator in series with the  $50 \Omega$  protecting resistor). The current  $I_s$  through  $L_s$  was at 1 GHz 3 dB larger than the current half way the TL, at the hole.

Figure 2.6 also shows the calculated (- - -)  $Z_T$  above 300 MHz corrected for the above mentioned TL effect. In practical situations the inaccuracy in  $Z_T$  due to this transmission-line effect is negligible up to 1 GHz. Therefore, no further investigations were carried out in order to describe the small differences (less than approx. 3 dB) between the theoretical and measured  $Z_T$ 's.

The present setup measures transfer impedances down to  $3 \mu\Omega$ . This lower limit could further be reduced by averaging multiple scans of the network analyzer, or by using a power

amplifier which increases  $I_{CM}$ . With the assumptions on the field attenuation stated above, the high frequency  $M$ -couplings down to 0.1 pH are measured with 25 percent accuracy, provided that TL effects are negligible.

## 2.4 Practical connectors

Our method is suited for relative measurement of  $Z_T$  (see also [Dun90]) and for absolute measurement. In this section we present results for relative measurements, as well as results for common connectors, single- and multi-pin, and the effects of different mounting methods.

As already mentioned in the introduction, rapid relative measurements were the incentive to develop our setup. Here we present as an example a prototype coaxial connector with a switch in the receptacle; a hole was present in the shield of the plug. The cable fixed to the plug had to be bent over a sharp angle, which caused a less dense braid at the outside bend and a larger overall  $Z_T$  of the combination cable, plug and receptacle. Guided by relative measurements for  $Z_T$  we improved the cable and plug. The results are presented in Fig. 2.7.

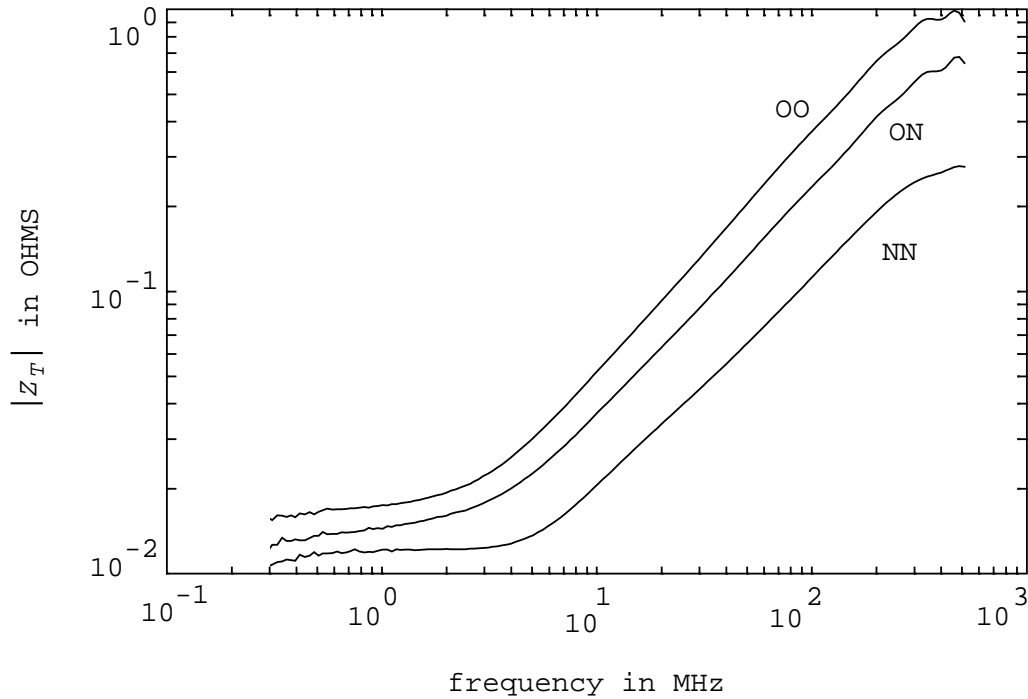


**Figure 2.7.**  $Z_T$  of coaxial connector with switch. For the abbreviations ‘OO’, ‘ON’, and ‘NN’ see the main text.

The fixed receptacle with switch was mounted on the current sensor. The plug consisted of different samples and was connected to different coax cables of 30 mm length. ‘OO’ was the reference sample, ‘ON’ had the same plug but a better coax cable, and finally ‘NN’ had both better plug and coax cable compared to the reference sample. In the frequency range 10-500 MHz we obtained an improvement of 11 dB with respect to the reference sample ‘OO’. The d.c. resistance was only slightly reduced.

Transfer impedances of commercial SMA connectors are given in Fig. 2.8. The connectors consisted of a plug which was soldered onto the semi-rigid  $V_{DM}$ -measuring cable and a PCB straight jack receptacle. The inner conductor of the receptacle was short circuited to its

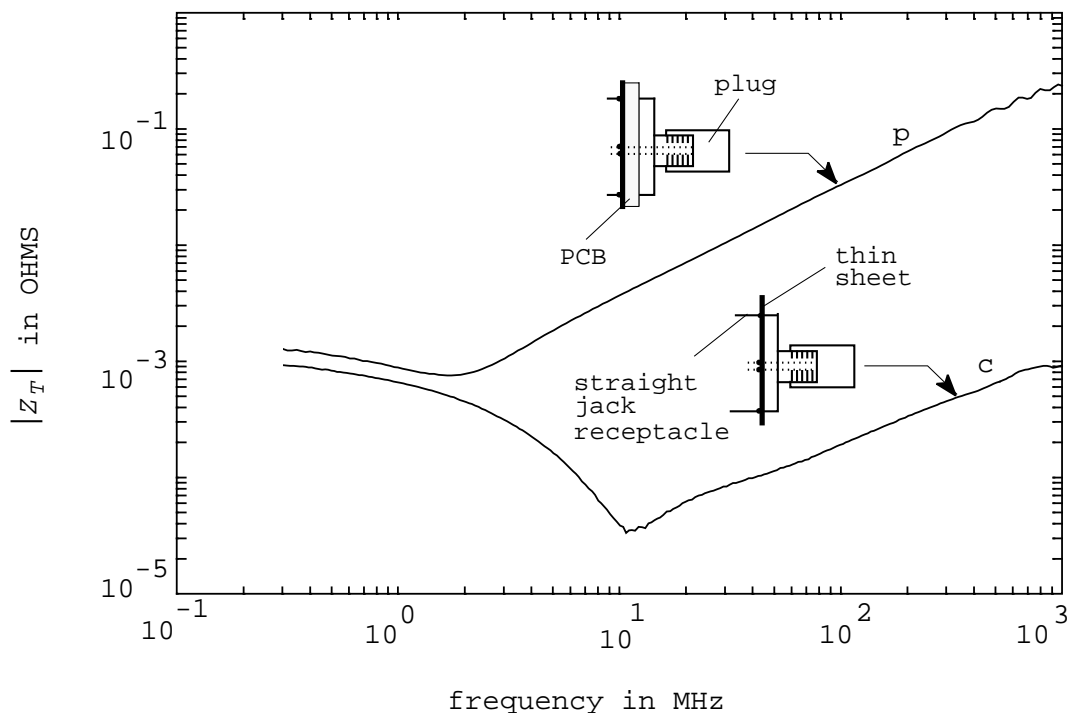


**Figure 2.8.** Measured  $Z_T$ 's of SMA connectors for a correct (c) and a poor (p) short circuit between inner leads and shield.

shield either by a 0.1 mm thick copper plate or by the single copper layer of a PCB; the thickness of the PCB was 1.5 mm. We deliberately used the PCB epoxy layer as standoff; the four pins of the receptacle shield thus remained 1.5 mm long (see Figs. 2.8 and 2.9b).

The  $Z_T$  of both assemblies differ by approx. two decades above 10 MHz. The correct and compact assembly clearly shows skin effect; the high-frequency coupling increases by approx. 10 dB/decade, indicating the dominance of contact impedance between plug and receptacle. The incorrectly mounted receptacle shows a slightly larger d.c. resistance of 1.3 m $\Omega$  and a mutual inductance of 49 pH. In terms of quality, the correctly mounted connector ranges between grade 1B (for semi-rigid and superscreened cables) and grade 2 (for double-braided cables); for an overview of these grades see Fowler [Fow75, Fow94].

Transfer impedances of some commonly used connectors (N, BNC, and SMA) were presented by [Hal73, Fow75, Eic85, Fow92]. Figure 2.9 shows a few connectors we investigated. In Fig. 2.10 the results for an N, SMA, BNC, C, UHF, and a 15-pins high-density D connector with metal shell are shown; for the D connector all internal pins were connected together at both sides. In all cases the current was injected on the receptacle whose shield was shorted with the inner conductor(s) (SC in Fig. 2.1 and left sides of the connectors in Fig. 2.9); the plug (right side in Fig. 2.9) was connected to the current sensor. For these measurements a new EMC box with a length of 16 cm was build.

The N connector is the best over almost the entire frequency range as shown in [Hal73, Fow75, Eic85, Fow92]. For high frequencies the N, SMA, and BNC are suitable; the C, UHF, and D connector are less suited in disturbing environments, in particular the D connector with an impedance of approx. 0.1  $\Omega$  at 100 MHz.

The  $Z_T$ 's of the N and SMA connectors depend on the fixing torque between plug and receptacle; in our case both samples were fixed with a torque of approx. 0.9 Nm. For example, Eicher [Eic85] showed approx. 60 dB  $Z_T$  difference at 1 GHz for an N connector

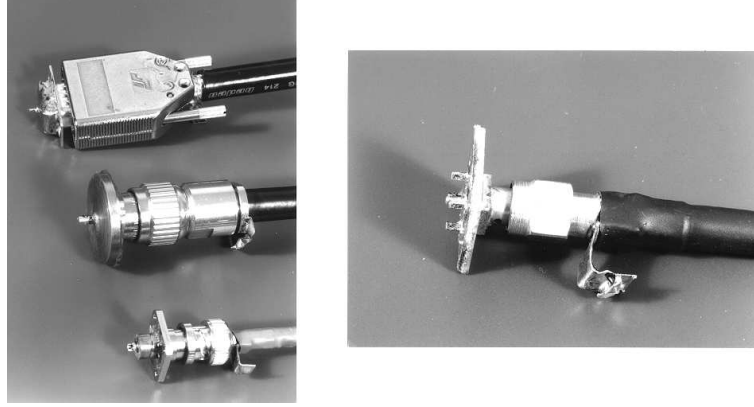


**Figure 2.9.** a) 15-pins high-density D connector (top), N connector (middle), and BNC (down).  
 b) SMA connector with receptacle mounted on a single-sided PCB; the plug was connected to the current sensor.

pair fixed with 7 and 11.5 cmkp (approx. 0.7-1.15 Nm) torque. The  $Z_T$  of the BNC connector pair depends on the rotational angle between plug and jack; Eicher observed approx. 40 dB difference between the best and worst case; our  $Z_T$  corresponds to his best case. Fowler [Fow75, Fow92] also found significant differences (more than one decade above 1 MHz) for a bayonet connector with and without side strain. Other mechanisms which influence the  $Z_T$  of connectors are the construction of the shield, gaskets, and the backshell to cable shield interfaces [Hoe88, Fow92].

The transfer impedance for a multiconductor cable depends weakly on the termination at both sides; typically less than 3 dB, see e.g. [Hoe88, Dem92, Kas94, Kas96]. Dunwoody and VanderHeyden [Dun90] also claimed such a relation for multi-pin connectors. Figure 2.11 shows results of different terminations for our 15-pins D connector: (1) all pins at both ends connected to each other and shorted to the shield at the left side in Figs. 2.1 and 2.2, (2) pin no. 5 shorted to the shield at the left side,  $V_{DM}$  measured at pin 5 at the right side, all other pins were left open, and (3) pin 8 shorted to the shield, all other opened.

The dips near 800 MHz in the measurements are caused by the difference in wave velocities at the inside and outside of the D connector (see [Hal88, Sze92]); the length of the connector was approx. 5 cm. The 3 dB variation reported in the earlier mentioned literature is confirmed as long as resonance effects do not show up; the  $Z_T$  is expected to have the lowest value for pin no. 5 since it is near a corner. Although the  $Z_T$  depends on the termination, the configuration with all pins shorted gives a good indication of the impedance which is admissible in practice.

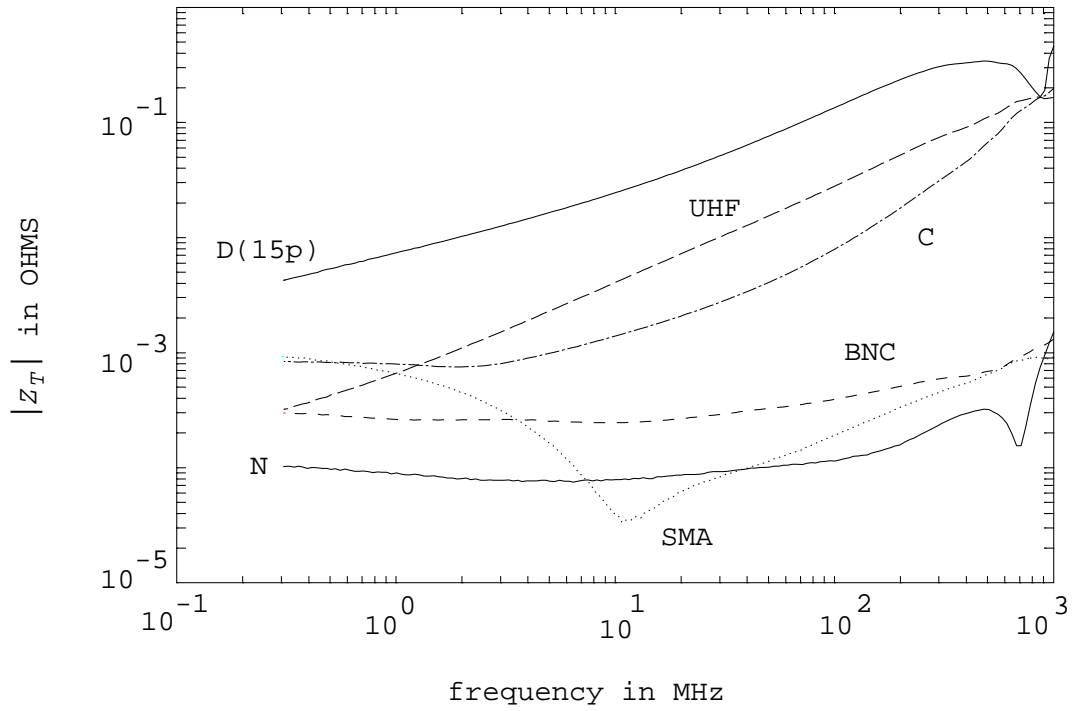


**Figure 2.10.** Results for an N, SMA, BNC, C, UHF, and 15-pins high-density D connector; all internal pins of the D connector were shorted at both sides. The dips around 800 MHz for the N and D connector are caused by the difference in wave velocities at the inside and outside of the DUT and the length of these connectors.

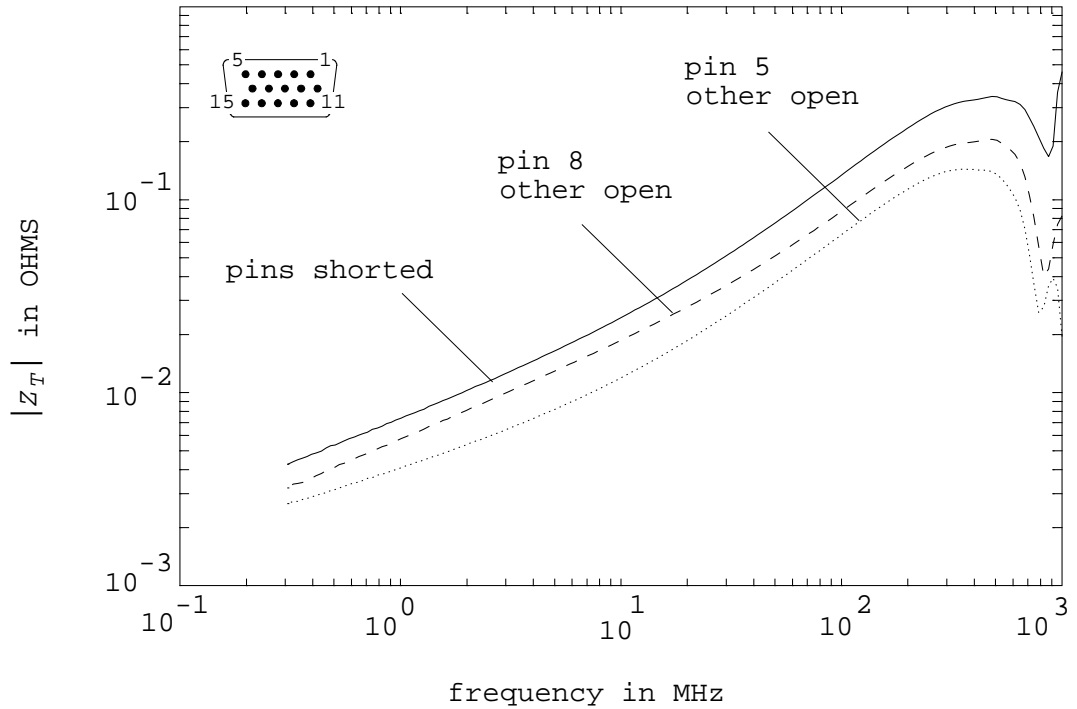


**Figure 2.11.**  $Z_T$  of 15-pins high-density D connector with different terminations in the DM-circuit (see main text).

## 2.5 Conclusions

A new method for measuring the transfer impedance of shielded connectors has been introduced. The main advantage over existing methods is ease of mounting connectors in the setup. The common-mode current  $I_{CM}$  and the differential-mode voltage  $V_{DM}$  generated are measured directly; no injection loss measurement or estimation are necessary. For connectors of maximum 3 cm length, transmission-line effects can be neglected; the 6 dB error at 1 GHz is admissible for practical purposes.

The parameters of the current sensor are known by calculations or by measurements; no calibration by a reference connector is needed. A tube with a well defined hole as test connector demonstrated the absolute accuracy of the setup. The setup correctly measures high-frequency transfer-impedances down to 0.1 pH. Measurements of a solid walled tube demonstrated a sensitivity down to  $3 \mu\Omega$  in a single scan of the network analyzer.

Results of practical single-pin as well as multi-pin connectors have been presented.



# Chapter 3

## Prediction of common-mode currents in cables attached to a PCB by means of a transmission-line approach

### Abstract

Common-mode (CM) currents generated by circuits on a triple-layer printed circuit board with a continuous ground plane have been studied by means of a transmission-line (TL) model. The CM current flows through the attached cables; the CM emission from these cables often dominates the direct radiation of the board. Several boards with different complexity were studied in the frequency domain. For demonstration purposes a board with modern digital electronics was developed. Measurements between 100 kHz – 1 GHz confirm the TL models.

### 3.1 Introduction

Modern multilayer printed circuit boards (PCB's) for high-frequency (HF) analog and digital electronics often contain large metallic land, sometimes full planes, which provide ground and the d.c. power supply. The tracks and the ground plane (GP) linking the components form many transmission lines (TL's), one might call them in EMC terminology differential-mode (DM) circuits (see Fig. 3.1). In the last decade the DM emission from PCB structures caused by the DM (or signal) current was calculated [Kam88, Nak89, Gre90, Nak95, Hil96]. Cables between PCB's or apparatus are primarily intended to transport DM signals. However, each cable is also a part of a larger circuit which closes via the environment of the PCB or via ground leads. The current in this circuit is a net current through the cable, the common-mode (CM) current in EMC terms. Because of their length, the cables often act as efficient antennas for the CM currents, producing more emission than the PCB itself as was predicted by Ott [Ott85] and verified afterwards by several other authors, see e.g. [Sze89, Pau89, Doc93, Oei94, Hoc96, Ler96].

Practical experience from many contracts with industry inspired us to develop an adapted test method in line with the precompliance method as proposed by Bersier [Ber83]. This method concentrates on the conduction currents or common-mode (CM) currents on cables connected to a multilayer printed circuit board (PCB); see also Fig. 3.2. Nowadays pre-compliance tests even largely suffice to demonstrate conformity with the European EMC requirements. The expensive and laborious full-compliance radiated emission and radiated immunity tests are replaced by a rapid and a simple method. In this Chapter we theoretically predict the CM current generated by a PCB for our precompliance setup; the connectors (see also Chapter 2) and cables can be handled separately. The fast calculations allow us to



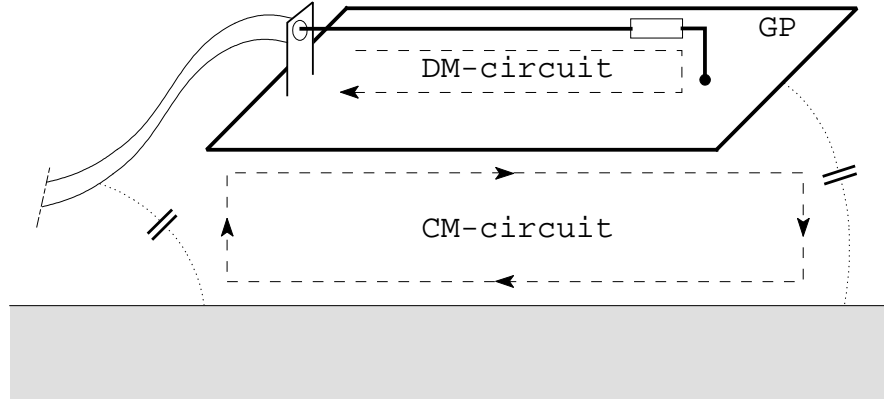


**Figure 3.1.** Differential-mode (DM) and common-mode (CM) definition. The CM current path closes via the ground plane (GP), the parasitic capacitances and the metallic plane below GP.

judge changes in the CM current during the design stage of a product, avoiding expensive redesigns after prototyping.

Our current based setup (Fig. 3.2) is closely related to Bergervoet's *et al.* [Ber97] CM-skeleton model. These authors model the PCB and all components by CM voltage-sources at the edges of the PCB, which drive the CM current into each cable attached to the PCB. Bergervoet *et al.* determined the sources and their internal impedances by measurements. Alternatively, a program as Fasterix [Clo94] may calculate those parameters: an equivalent network of the PCB and its components result from a full EM-wave analysis. Even for simple PCB's the calculation still takes many hours, a long time in the routing- and placement-stage of a product.

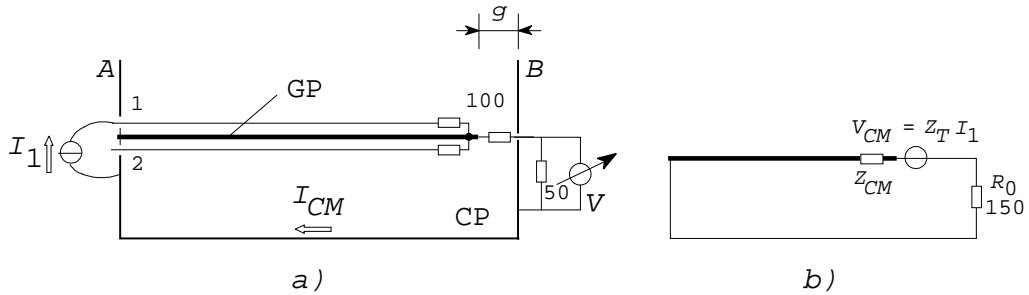


**Figure 3.2.** a) Setup for precompliance measurements with current injection through track 1 of the PCB shown in Fig. 3.3. The CM current is measured via the  $150\ \Omega$  load consisting of a  $100\ \Omega$  resistor in series with the  $50\ \Omega$  input impedance of the analyzer. The  $100\ \Omega$  bridges the gap  $g$  between the ground plane and brass plate  $B$ . b) The PCB is replaced by a voltage source  $V_{CM} = Z_T I_1$ ; the CM impedance  $Z_{CM}$  is formed by the ground plane (GP) of the PCB and by a large metallic plate (see also Fig. 3.1) at some distance, e.g. a cabinet panel (CP).

We consider first a multilayer PCB (see Fig. 3.3) with a continuous ground plane (GP); the signal- or differential-mode (DM) current in the tracks closes via the GP (see also Fig. 3.1). Later on ground tracks will also be considered. The tracks and the CM circuit are modeled as coupled transmission lines. In combination with analytical approximations for the TL parameters, the TL approach strongly reduces the computational effort or the

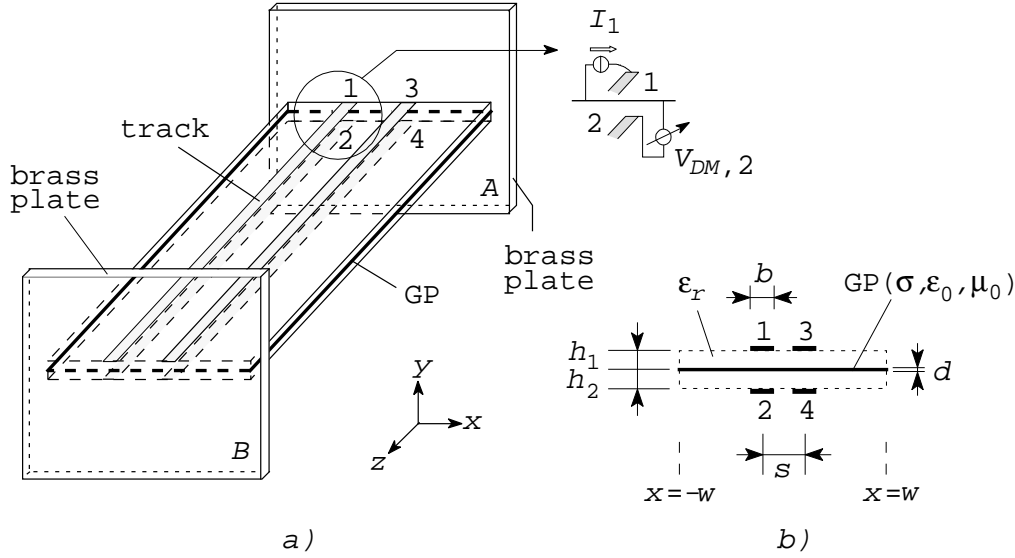


**Figure 3.3.** Four tracks on a triple layer PCB with ground plane (GP) as middle layer. The tracks of width  $b$  and the GP are terminated at side  $B$  into different impedances. b) cross section of the PCB.

computer hardware requirements. The comparison of the results with actual measurements was encouraging, in spite of the large number of simplifications. A personal computer calculates a typical configuration in a few minutes, depending on the complexity of the board; see also Chapter 5.

The induction coefficients of the transmission lines were obtained from a two-dimensional (2D) theoretical study of the model PCB in Fig. 3.3. The capacitive parameters of the TL's were also studied by this model PCB. A second metallic plate, e.g. a cabinet panel (CP), was placed at some distance under the PCB (Fig. 3.2) to provide a well-defined path for the CM current. This setup is similar to the one proposed by Bersier; the  $R_0 = 150 \, \Omega$  resistor in Fig. 3.2 models the CM-radiation resistance of a cable at resonance. This resonant condition may not occur at all frequencies in the DM signal, but will most probably do so at some frequency for which the emission limits might then be exceeded. Coenen [Coe94] obtained an average  $150 \, \Omega$  radiation resistance in the frequency range  $150 \, \text{kHz} - 1 \, \text{GHz}$  for cables which do not run directly over conductive surfaces or in cable trays or conduits. A transfer impedance  $Z_T = V_{CM}/I_1$  can be defined, which relates a DM current ( $I_1$ ) injected in e.g. track 1 to the equivalent voltage source at the edge of the PCB. For the setup of Fig. 3.2 the common-mode current  $I_{CM}$  then equals  $V_{CM}/(Z_{CM} + 150)$ . In the treatment of two-dimensional structures it is more convenient to use also the transfer impedance  $Z_t = V_{CM}/I_1 \ell$  per unit length (with small  $t$  as subscript). From the context and the subscript it will be clear whether the total quantity or the quantity per unit length are used.

A good EMC criterion for emission is the  $3 \, \mu\text{A}$  'rule of thumb' limit [Goe92, Section 2.4.1]) based on test experiences: CM currents in any cable connected to the equipment may not exceed  $3 \, \mu\text{A}$  (see also Section 3.3). If an actual cable is attached to the PCB, the CM-current distribution can in principle be calculated by an integral equation method. From this CM-current distribution through the cable the far field can be established, see e.g. Ramo [Ram94, Chapter 12] and Balanis [Bal97, Chapter 4].

The reciprocal situation, the immunity problem or CM-DM coupling, can also be handled by the Bersier method. When an electromagnetic wave illuminates the cable (see [Tay92]

and references added therein), a CM voltage-source at the edge of the PCB may be chosen to replace the cable and the wave. In the Bulk Current Injection (BCI) technique [Car96, Tro96] a current is directly injected. A CM current through the ground plane of the PCB then induces disturbing voltages in the DM circuits. Again, direct coupling between wave and DM circuits is often less important. Note the close relation with a transistor radio or mobile telephone: the cable is now an antenna and the CM current the desired signal current.

The PCB's studied (Fig. 3.3) have three layers [Hor96a, Hor96b, Hor97a, Hor97b, Hor97c]. A continuous copper ground plane (GP) of length  $\ell = 20$  cm has a conductivity  $\sigma = 5.8 \cdot 10^7 \Omega^{-1}\text{m}^{-1}$  and thickness  $d = 30 \mu\text{m}$ ; the width  $2w$  varies between 5 and 15 cm. Tracks of  $b = 1.5$  mm width are placed at  $h_{1,2} = 1.5$  mm above and below the GP. The dielectric constant  $\varepsilon_r$  of the epoxy insulation is 4.7. Details of the measurements are given in [Hor96a, Section VII]. The tracks run parallel to the length of the PCB; in later calculations track 1 meanders over the surface. A DM current is injected at side  $A$ ; the tracks terminate into different impedances at end  $B$ . The CM circuit consists of the GP and a large brass plate (cabinet panel CP in Figs. 3.2a and 3.4) under the PCB at the distance  $h_{CP} = 1$  cm.

Section 3.2 describes the CM to DM or Bersier coupling if resonant effects do not show up. The inductive part of this coupling can be used for a first-order prediction of the generated CM current (Section 3.3). Section 3.4 describes the transmission-line approach for the DM to CM coupling. Results of the TL method for the simple PCB with parallel tracks (Fig. 3.3), some more complicated meandering tracks, and ground tracks are shown in Section 3.5. For demonstration purposes we developed two boards with HCT and HLL digital logic, see Section 3.6. In Section 3.7 some additional coupling effects are discussed which influence the calculations and measurements. Finally, Section 3.8 gives concluding remarks.

### 3.2 Low-frequency CM to DM coupling

The DM circuits on a PCB may generate a CM current which flows along the cables connected to the PCB. In the reciprocal setup, a CM current  $I_{CM}$  flows through the GP; as return path we imagine a second plane, for instance a cabinet panel (CP), under the GP (Fig. 3.4). We investigate the CM current distribution over the GP and the resulting coupling with the DM circuit, expressed as  $Z_t$  per unit length. Sensing track 1 is placed at the distance  $h_1 = 1.5$  mm above or below the GP. Several limiting situations can be considered: the CP a) has a certain width  $2p$  or b) is very large in the  $x$ -direction; the CP is c) nearby ( $h_{CP}/w \ll 1$ ) or d) at a large distance from the GP ( $h_{CP}/w \rightarrow \infty$ ).

In the experiments we used a brass plate as CP of thickness  $d_p = 1.5$  mm and width  $2p = 20$  cm. The sheet resistance of the copper GP is given by  $R_\square = 1/\sigma d$ ; we reserve this symbol for the GP. A similar expression holds for the brass CP with conductivity  $1.43 \cdot 10^7 \Omega^{-1}\text{m}^{-1}$  and thickness  $d_p$ . In the calculations we may assume the thin-plate limit for both GP and CP, i.e. both thicknesses approach zero while the sheet resistances are kept at their actual values. The current distribution then follows from a set of coupled Fredholm integral equations of the second kind. In Appendix D such an integral equation for a thin wire above a single GP is given, which was solved by the method of moments (MOM) [Har93]. The method can readily be applied to two or even more plates.

The MOM-calculated  $Z_t$  between CM to DM circuits is presented in Fig. 3.5 for the middle position ( $x \simeq 0$ ) of the sensing track, with the CP at the distance of  $h_{CP} = 1$  cm. At d.c. or low frequencies the sheet-current density in the GP is homogeneous  $K_z = I_{CM}/2w$  (in A/m) and  $Z_t = R_\square \ell / 2w$ . Above the frequency  $f_c = 2wd \simeq \delta^2$  [Hel95]  $K_z(x = 0)$  decreases

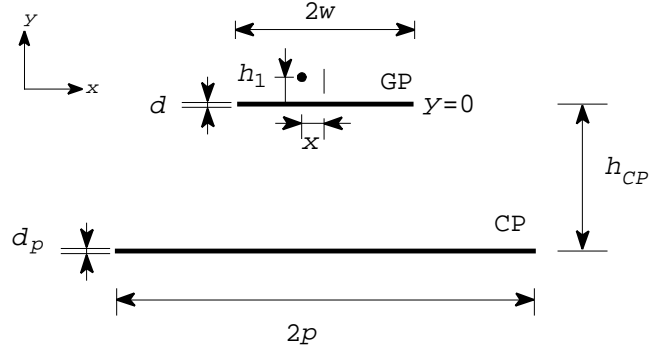


**Figure 3.4.** Parameters for the PCB above a cabinet panel (CP).

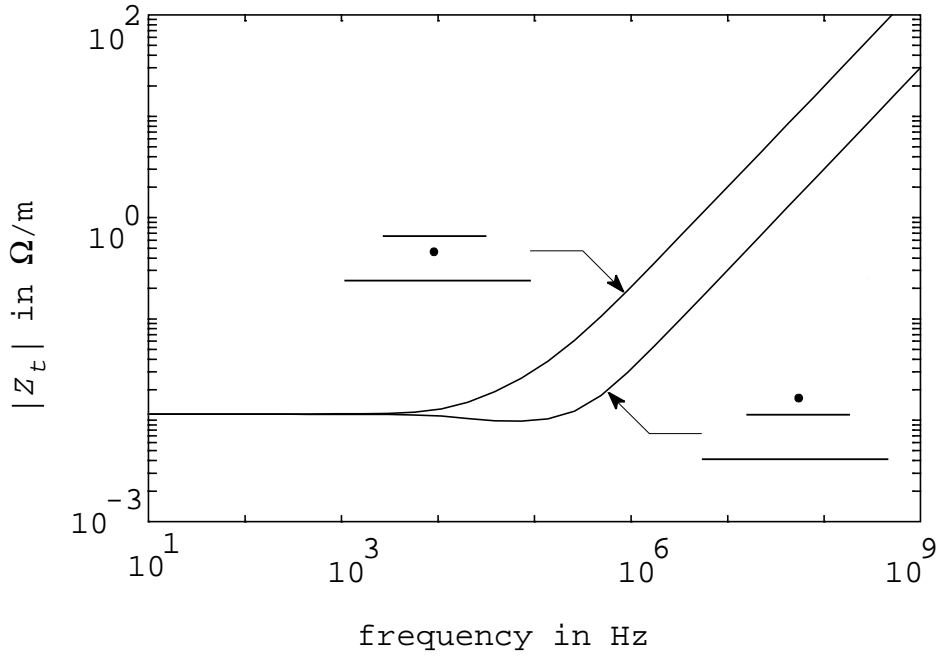


**Figure 3.5.** CM to DM  $Z_t$  for two positions of the sensing track;  $h_{CP} = 1$  cm,  $2w = 50$  mm,  $h_1 = 1.5$  mm.

towards the high-frequency value  $I_{CM}/\pi w$  [Kad59, p. 63];  $\delta = \sqrt{2/\omega\mu_0\sigma}$  is the skin depth. For the GP width chosen, the corresponding decrease in  $Z_t$  by a factor  $2/\pi$  barely shows up because of the inductive behavior of  $Z_t$  at high frequencies.

The mutual-inductance part of  $Z_t$ ,  $M_s$  can also be calculated by conformal mapping, see Appendix A. We derived closed-form approximations for  $M_s(x, y)$ -values for the sensing track 1 at various positions. Consider first a CP at large distance from the GP, i.e.  $h_{CP} \rightarrow \infty$ . The  $M_s$ -values for the track 1 at  $x = 0$  and  $|x| = w$  are:

$$M_s(0, h_1) = \frac{\mu_0}{2\pi} \ln \left( \frac{h_1}{w} + \sqrt{1 + \left( \frac{h_1}{w} \right)^2} \right) \simeq \frac{\mu_0}{2\pi} \frac{h_1}{w} \quad (3.1)$$

$$M_s(|x| = w, h_1) \simeq \frac{\mu_0}{2\pi} \sqrt{\frac{h_1}{w}}. \quad (3.2)$$

The approximated expressions for  $M_s$  present the lower and upper bound, which are accurate to within 10 percent for the track at either side of the GP when  $h_1/w < 0.9$ . The approximated  $M_s$  in Eq. (3.1) is equivalent to Hubing's partial mutual inductance [Hub94, Eq. (21)] of a finite-width plane.

At high frequencies a nearby large CP ( $h_{CP}/w \ll 1$ ) compresses the H-field between GP and CP, and reduces the field above the GP. Figure 3.6 shows the magnetic field lines calculated by the MOM for low (10 Hz) and high frequencies (1 GHz) with  $h_{CP} = 1$  cm.

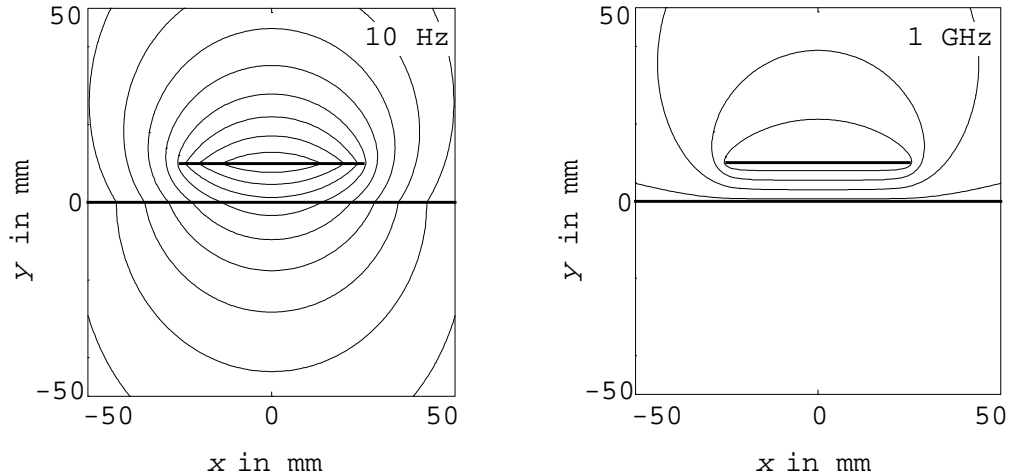


**Figure 3.6.** Magnetic field pattern at low and at high frequency for a CM current through the CP ( $2p = 20$  cm) which returns via the GP ( $2w = 5$  cm).

Because of the homogeneity of the field under the GP, a first approximation for  $M_s(x, y)$  with sensing track at  $x = 0$  and  $y = -h_1$  under the GP is:

$$M_s(0, -h_1) \simeq \mu_0 \frac{h_1}{2w}, \quad (3.3)$$

a factor  $\pi$  larger than Eq. (3.1) for the isolated PCB.

At other positions of the track 1 the  $M_s$ -values are more difficult to obtain. Love [Lov23] gave the general Schwarz-Christoffel transformation, which involves elliptic functions; his results were extended by Langton [Lan81] and Lin [Lin85]. This method only gives an

implicit solution. For the position  $(x, y) = (0, h_1)$  above the GP, the expansion of the elliptic functions in Appendix A.1 results in

$$M_s \simeq \mu_0 \frac{K}{K'} \frac{1}{\frac{K'}{K}\pi - 2} \frac{h_1}{h_{CP}}, \quad (3.4)$$

with

$$\frac{K'}{K} = \frac{w}{h_{CP}} \left[ 1 + \frac{h_{CP}}{\pi w} \left( 1 + \ln \frac{2\pi w}{h_{CP}} \right) \right]. \quad (3.5)$$

For  $h_{CP}/w \ll 1$  we have

$$M_s(0, h_1) \simeq \mu_0 \frac{h_1 h_{CP}}{\pi w^2} \quad (3.6)$$

which is a factor  $2h_{CP}/\pi w$  smaller than the  $M_s$  at the lower side of the GP, Eq. (3.3). For the track 1 at the edge of the GP,  $|x| = w$ , we proceed in a different and approximate way. When  $h_{CP} \ll 2w$ , the other edge may be thought far away. The  $M_s$  near one edge can then be derived from a simpler transformation which is often employed for the fringing field of a parallel-plate capacitor [Ram94, Section 7.7]. The solution is still implicit (see Appendix A.2), but involves only an exponential. When  $h_1 \ll h_{CP}$ , the first two terms in the expansion of the exponential result in:

$$M_s(|x| = w, |y| = h_1) \simeq \frac{\mu_0}{2w} \sqrt{\frac{h_1 h_{CP}}{\pi}} \quad (3.7)$$

irrespective on which side of the GP track 1 is placed. Already for  $h_1 \simeq h_{CP}/10$  higher-order terms in the expansion become discernible. A numerical fit to the calculations resulted in a correction term

$$\Delta M_s(|x| = w, y) \simeq \frac{\mu_0}{2w} c_1 y \quad (3.8)$$

with  $c_1 \simeq -1/3$ , in which  $y$  is positive for positions above the GP. This  $\Delta M_s$  restores the actual asymmetry between upper and lower positions of the track 1; for a more elaborate fit see Appendix A.2 and Fig. A.3. The variation of  $M_s(x, h_1)$  and  $M_s(x, -h_1)$  over the width of a GP is shown in Fig. 3.7a, whereas Fig. 3.7b gives  $M_s$  as function of  $h_{CP}/w$  for a few fixed positions of the sensing track. For this GP size and position ( $2w = 5$  cm,  $h_{CP} = 1$  cm) the assumption  $h_{CP}/w \ll 1$  is not fulfilled, and the actual magnetic flux between GP and CP is lower than assumed. The current distribution  $K_z(x)$  in the GP and the total flux between GP and CP calculated by MOM agreed well with the analytical expression for parallel strips given by Kuester and Chang [Kue80, Eq. (6)]. When track 1 is close to the GP, we can correct the  $M_s$ -values given by Eqs. (3.3), (3.6), and (3.7) by the ratio of their total flux Eq. (A.14) and the flux of the homogeneous field  $H = I_{CM} h_{CP}/2w$ ; see Appendix A.2 at the end. For our 5 cm wide GP at 1 cm above the cabinet panel we find a correction factor of 0.67.

### 3.3 Conducted emission

A description of conducted emission can be based upon the transfer impedance  $Z_t(\text{CM-DM}) = Z_t(\text{DM-CM})$  of the previous section; the Bersier setup Fig. 3.2a is employed. The current waveforms in the DM circuit are typical choices for a switched-mode power supply and for several families of logic circuits (Fig. 3.8). We connect the GP at the left side to the CP (Fig. 3.2); the DM track is shorted at the right side near the plate  $B$ . In this model

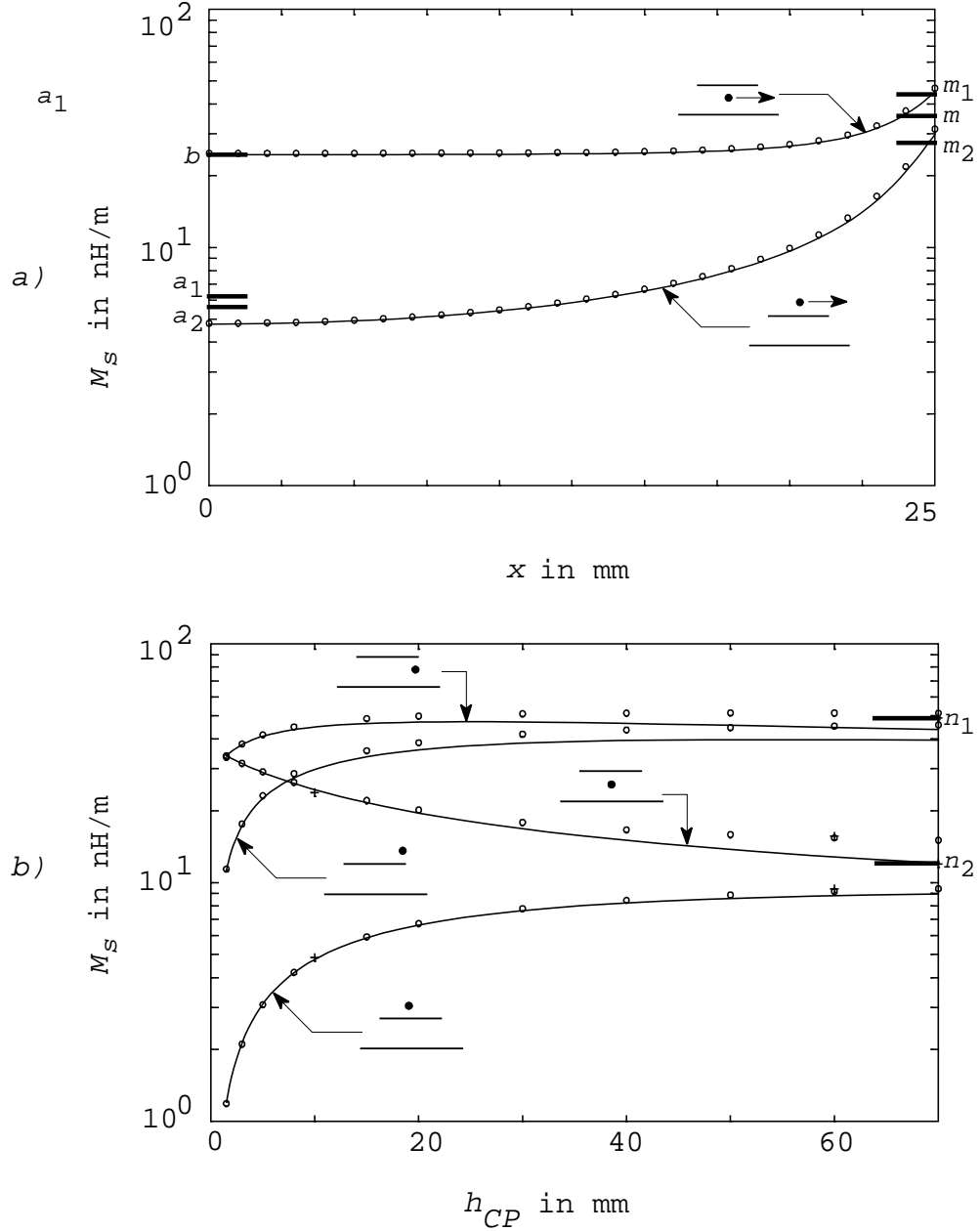


**Figure 3.7.** a) Mutual inductance  $M_s$  between CM and DM loop when the  $x$ -position of the track varies over the GP (full width 5 cm). The 20 cm wide CP is at  $h_{CP} = 1$  cm under the GP. The circles are MOM results, the solid lines are analytical approximations discussed in Appendix A.2. The three markers  $m$ ,  $m_1$ , and  $m_2$  on the right vertical axis indicate the  $M_s$ -values at the edge. The marker  $m$  is  $M_s$  from Eq. (3.7), to which the correction  $\Delta M_s$  from Eq. (3.8) has been added (marker  $m_1$ ) or subtracted (marker  $m_2$ ). The markers  $a_1$  and  $b$  on the left vertical axis correspond to Eq. (3.6) and Eq. (3.3) multiplied by the correction factor 0.67, see also the main text. For comparison the marker  $a_2$  corresponds to Love's expression Eq. (3.4) without any correction. b) Mutual inductance  $M_s$  between CM and DM loop as function of  $h_{CP}$  for four positions of the sensing track. The upper marker  $n_1$  at the right vertical axis corresponds to Eq. (3.2), the lower marker  $n_2$  to Eq. (3.1).

we still neglect the propagation delays over the PCB; the induced CM voltage  $v_{CM}(t)$  can be imagined as a localized source between cable and GP which drives the cable as antenna. The CM current  $i_{CM}(t)$  through the cable at resonance is then given by  $v_{CM}(t)/R_0$ .

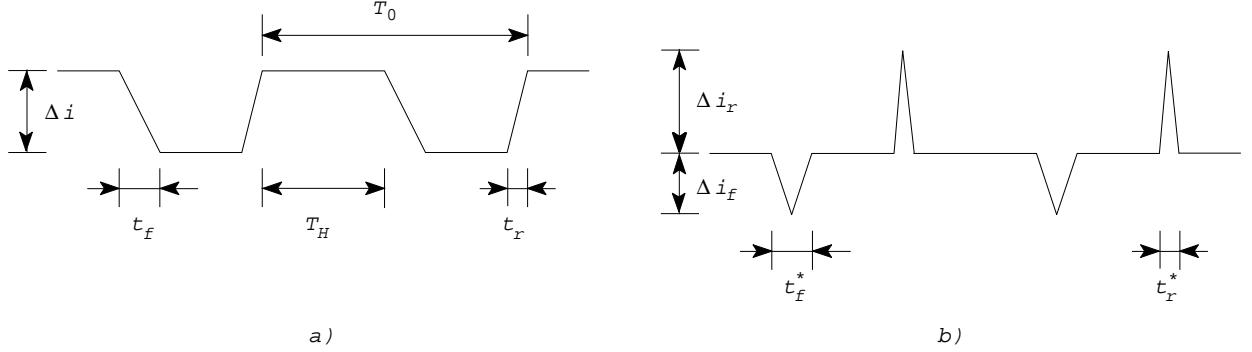


**Figure 3.8.** Typical current waveforms for a) switched-mode power supplies and TTL and ECL digital circuits, b) for fast CMOS circuits.

The DM current waveforms in switched-mode power supplies or TTL and ECL (nowadays obsolete) digital circuits is approximated by the trapezoids in Fig. 3.8a. For CMOS and similar circuits, the DM current resembles more a triangular shape (Fig. 3.8b). The trapezoidal current  $i_{DM}(t)$  of period  $T_0$  is expanded in the Fourier series

$$i_{DM}(t) = \sum_{n=-\infty}^{\infty} I_n^{DM} e^{jn\omega_0 t}, \quad (3.9)$$

with  $\omega_0 = 2\pi f_0 = 2\pi/T_0$ . For  $t_r = t_f = \tau$  the coefficients  $I_n^{DM}$  are given by

$$I_n^{DM} = \Delta i \frac{\sin(n\omega_0\tau/2)}{n\omega_0\tau/2} \frac{\sin[n\omega_0(T_H + \tau)/2]}{n\pi}. \quad (3.10)$$

The transfer impedance per unit length  $Z_t(\text{DM-CM})$  can be approximated by (see also Fig. 3.5)

$$Z_t(\omega) \simeq R_{GP} + j\omega M_s, \quad (3.11)$$

with  $R_{GP}$  the resistance of the ground plane. The induced voltage  $v_{CM}(t)$  then follows from

$$v_{CM}(t) = \sum_{n=-\infty}^{\infty} V_n^{CM} e^{jn\omega_0 t}, \quad (3.12)$$

with

$$V_n^{CM} = Z_t(n\omega_0) I_n^{DM}. \quad (3.13)$$

According to the EN55022 regulation, the maximum electric field strength should not exceed  $30 \text{ dB}\mu\text{V/m}$  (at 10 m for class B equipment) in the frequency range 30-230 MHz. This requires a CM current through the cable of less than approx.  $3 \mu\text{A}$ , see e.g. Ott [Ott85] or Goedbloed [Goe92, Section 2.4.1].

The fundamental frequency  $f_0$  determines the smallest harmonic number  $m$  in Eq. (3.9) with  $mf_0 \leq 30 \text{ MHz}$ , for which the EMC requirements should be met. The corresponding



**Table 3.1.** Upper bounds for the maximal spectral components of  $i_{CM}$  given by the r.h.s. of Eq. (3.14). For the switched-mode power supply (SMPS) and ECL3 (or ECL-100K) digital logic, the trapezoidal waveform (Fig. 3.8a) is used; a triangular shape form (Fig. 3.8b) is assumed for CMOS and HLL logic. The mutual inductances  $M_s$  are calculated by MOM (Section 3.2).

| TYPE<br>$f_0/\tau/\Delta i$               | $\max\{ I_m^{CM} \}$ in $\mu\text{A}$ per length of PCB |  |   |  |
|---|---|--|---|--|
|   | $2w = 5 \text{ cm}$                                     |  | $2w = 15 \text{ cm}$                    |  |
|   | injection 1<br>$M_s = 4.8 \text{ nH/m}$                 | injection 2<br>$M_s = 24.9 \text{ nH/m}$ | injection 1<br>$M_s = 0.6 \text{ nH/m}$ | injection 2<br>$M_s = 10.6 \text{ nH/m}$ |
| SMPS<br>100 kHz/100 ns/1 A                | $1.4 \cdot 10^0$  | $7.0 \cdot 10^0$                         | $2.0 \cdot 10^{-1}$                     | $3.0 \cdot 10^0$                         |
| ECL3 (ECL-100K)<br>230 MHz/1.3 ns/14.8 mA | $4.6 \cdot 10^2$  | $2.4 \cdot 10^3$                         | $5.8 \cdot 10^0$                        | $1.0 \cdot 10^3$                         |
| CMOS<br>10 MHz/60 ns/4.2 mA               | $2.9 \cdot 10^0$  | $1.5 \cdot 10^1$                         | $4.0 \cdot 10^{-1}$                     | $6.3 \cdot 10^0$                         |
| HLL (CMOS 3V)<br>230 MHz/1.5 ns/100 mA    | $5.4 \cdot 10^3$  | $2.8 \cdot 10^4$                         | $6.8 \cdot 10^2$                        | $1.2 \cdot 10^4$                         |

spectral component of  $i_{CM}(t)$  is  $I_m^{CM} = V_m^{CM}/R_0$  when the resistance term in  $Z_t$  is neglected. The upper bound for the amplitude of this spectral component is given by

$$|I_m^{CM}| \leq \frac{4M_s \Delta i}{\pi m R_0 \tau}, \quad (3.14)$$

which holds for the waveform given in Fig. 3.8a. For the waveform given in Fig. 3.8b,  $\tau$  must be replaced by  $\min\{t_r^*/2, t_f^*/2\}$  and  $\Delta i$  by  $\max\{\Delta i_r, \Delta i_f\}$ .

In Table 3.1,  $|I_m^{CM}|$  is given for a few families of digital circuits. As can be seen, the 3  $\mu\text{A}$  limit for ECL3 and HLL digital logic requires extensive additional EMC measures. A reduction of about 44 dB and 65 dB, respectively, should be obtained in case of our 0.2 m long and 5 cm wide PCB, for instance by an extra ground plane or cabinet panel, smaller distances between tracks and GP, filter connectors, etc.

### 3.4 Transmission-line approach

We now extend the description to include propagation effects. The four DM circuits and the CM circuit are considered as a set of transmission lines (TL's). The coupling between the lines is described by the resistive and inductive transfer impedance and the capacitive transfer admittance.

We regard the tracks over the GP as microstrip lines. The dominant transmission mode is quasi-TEM: a TEM wave adapted to include the nonhomogeneous dielectric by modifying the line capacitance, and the conductor losses by adding a series resistance. Gupta *et al.* [Gup96] gave an overview of the vast literature published over the last decades. For convenience we repeat here Gupta's expressions (Eq. (2.116)) for the characteristic impedance  $Z_m$  above a very wide GP:

$$Z_m = \begin{cases} \frac{\eta}{2\pi\sqrt{\epsilon_{r,eff}}} \ln\left(\frac{8h}{b} + 0.25\frac{b}{h}\right) & , \quad \frac{b}{h} \leq 1, \\ \frac{\eta}{\sqrt{\epsilon_{r,eff}}} \left\{ \frac{b}{h} + 1.393 + 0.667 \ln\left(\frac{b}{h} + 1.444\right) \right\}^{-1} & , \quad \frac{b}{h} > 1, \end{cases} \quad (3.15)$$

and

$$\varepsilon_{r,eff} = \frac{\varepsilon_r + 1}{2} + \frac{\varepsilon_r - 1}{2} \begin{cases} (1 + 12h/b)^{-1/2} + 0.04(1 - b/h)^2 & , \quad \frac{b}{h} \leq 1, \\ (1 + 12h/b)^{-1/2} & , \quad \frac{b}{h} > 1, \end{cases} \quad (3.16)$$

where  $\eta = \sqrt{\mu_0/\varepsilon_0} \simeq 120\pi \Omega$ . The characteristic impedance  $Z_m$  and the effective dielectric constant  $\varepsilon_{r,eff}$  depend on  $\varepsilon_r$  and  $b/h$ . The finite size of the GP and the presence of the dielectric increase  $Z_m$ ; the deviation is less than 3 percent when the track is more than  $2b$  from the edge, as was shown by Smith and Chang [Smi85].

When the damping is small we may also write  $Z_m = \sqrt{L_s/C_s}$ . The self-inductance  $L_s$  can be obtained from  $L_s = Z_{0m}/c_0$ , with  $Z_{0m}$  the characteristic impedance of the microstrip with the dielectric replaced by vacuum or  $\varepsilon_{r,eff} = 1$ , and  $c_0$  the velocity of light in vacuo. For all tracks on our PCB's we use the same  $L_s = 414$  nH/m, calculated as if the GP were of infinite extent. Inserting the proper value for  $\varepsilon_{r,eff} = 3.34$ , one finds for the capacitance  $C_s = 88.9$  pF/m and for  $Z_m = 68 \Omega$ .

The series impedance  $Z_s$  for the track is  $Z_s(\omega) = R_{DC} + R_s(\omega) + j\omega L_s$ , where  $R_{DC}$  and  $R_s(\omega)$  are the d.c. and skin-effect resistances. Closed-form expressions for the skin-effect resistance were first published by Pucel *et al.* [Puc68] in 1968, where they used Wheeler's incremental inductance rule. Recently Collin proposed expressions by means of conformal mapping [Col92, Appendix III]. These values are somewhat higher than Pucel's one; Collin claims that his solution is in better agreement with experimental results [Col92, pp. 156-7]. For a microstrip structure with a finite-width GP (as in our case), Djordjević [Djo94] gives other expressions for  $R_s(\omega)$ . The high-frequency current distribution in a microstrip line and a rectangular strip is given in several papers by Faraji-Dana and Chow [Far90a, Far90b, Far91]. In the calculations we used Collin's value. However, for our experimental boards we had to increase *ad hoc* the skin-effect resistance  $R_s(\omega)$  for all frequencies by a factor of five compared to Collin's value, to obtain a good fit of the amplitude and the width of the resonances, in the input impedance of the DM circuit and in the DM-CM coupling. A detailed analysis [Hor97a, Section IIe] showed that this increase may indeed be caused by the manufacturing process.

Figure 3.9 shows the four tracks (Fig. 3.3) as coupled microstrip lines TL1-TL4 with the ground plane (GP) as reference;  $z = 0$  corresponds with the side of plate *A* (near end) and  $z = \ell$  with the side *B* (far end). The TL5 describes the CM current through the GP with return CP (Figs. 3.2 and 3.4). The  $5 \times 5$  impedance matrix  $\mathbf{Z}(\omega)$  per unit length with GP as reference is then given by

$$\mathbf{Z}(\omega) = \mathbf{Z}_d(\omega) + \mathbf{Z}_t(\omega), \quad (3.17)$$

in which  $\mathbf{Z}_d = \text{diag}(Z_s, Z_s, Z_s, Z_s, Z_{CM})$  is the self-impedance diagonal matrix,  $\mathbf{Z}_t(\omega)$  the transfer impedance matrix with zeros on the diagonal, and  $Z_{CM} = \sqrt{L_{CM}/C_{CM}}$  the proper impedance of the CM circuit formed by GP and CP. The self inductance  $L_{CM}$  of the CM circuit may be taken from Kuester and Chang [Kue80] for large  $2w/h_{CP}$ . The capacitance  $C_{CM}$  in vacuum results from  $C_{CM} \simeq 1/c_0^2 L_{CM}$ . The 1.5 mm dielectric layer increases this value by about 13 percent with  $h_{CP} = 1$  cm. The elements of  $\mathbf{Z}_t$  matrix between de DM and CM circuits are given in Section 3.2. At high frequencies these matrix-elements are predominantly given by the mutual inductances  $M_s$  discussed above. The off-diagonal elements of  $\mathbf{Z}_t$  between the tracks will be extensively discussed in Chapter 4. Only the coupling between tracks on the same side are relevant for the total DM-CM coupling: between 1 and 3 and between 2 and 4. The coupling between tracks on opposite sides can be neglected.

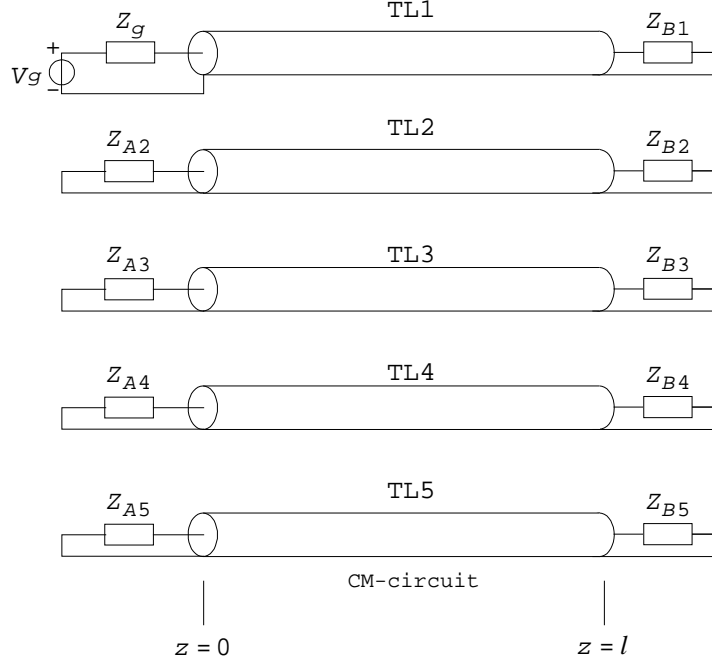


**Figure 3.9.** Transmission-line (TL1-TL4) model of the four-track PCB in Fig. 3.2; TL5 incorporates the DM-CM couplings as discussed in the text. The near side  $z = 0$  corresponds with the side of brass plate *A*, the far end  $z = \ell$  with brass plate *B*. The terminating impedances are discussed in the text.

As admittance matrix we have  $\mathbf{Y}(\omega) = j\omega\mathbf{C}$ , where  $\mathbf{C}$  is the  $5 \times 5$  capacitance matrix. It is more difficult to calculate the off-diagonal elements of the capacitance matrix because the boundary conditions on the dielectric need to be accounted for. We followed a similar numerical approach by Harrington [Har69] and Venkataraman [Ven85] for static electric fields. For highest accuracy the discretization must be adapted; see Appendix B. In an iterative procedure we calculated the absolute error in the tangential electric field, integrated over each conductor element; for the dielectric boundaries we took the integrated absolute error in the condition for the normal component of the electric field. The element sizes were adjusted until an equipartition of the errors over the elements occurred. Again, the DM-DM capacitive couplings become negligibly small, with the exception of those between the tracks which are on the same side of the CP.

The DM-CM capacitive coupling coefficients must be calculated quite accurately. From extensive calculations we derived analytical approximations which suffice in our TL model. In order to limit the size of the matrices to be displayed here, suppose that only track 1 (Fig. 3.4) is present. The capacitance matrix then becomes

$$\mathbf{C} = \begin{bmatrix} C_s + C_{1-CP} & -C_{1-CP} \\ -C_{1-CP} & C_{CM} + C_{1-CP} \end{bmatrix}. \quad (3.18)$$

In vacuo the capacitance matrix  $\mathbf{C}_0$  satisfies the well-known relation

$$\mathbf{L}\mathbf{C}_0 = \frac{1}{c_0^2}\mathbf{I}_2 \quad (3.19)$$

with  $\mathbf{I}_2$  the  $2 \times 2$  identity matrix and

$$\mathbf{L} = \begin{bmatrix} L_s & M_s \\ M_s & L_{CM} \end{bmatrix}, \quad (3.20)$$

the inductance matrix. We found the following approximate relation between  $C_{1-CP}$  and  $C_{1-CP,0}$ , the capacitive coupling coefficients with and without dielectric

$$C_{i-CP} \simeq \frac{C_{i-CP,0}}{\varepsilon_{r,eff}^{1/4}}. \quad (3.21)$$

This procedure is tested for a wide range of parameters. For a maximum deviation of 25 percent between numerical results and approximate analytical expressions this parameter range is:  $1 \leq \varepsilon_r \leq 12$ ,  $0 \leq x/2w \leq 0.9$ ,  $0.5 \leq b/h \leq 3$ ,  $0.05 \leq w/p \leq 1$ , and  $0.1 \leq 2w/h_{CP} \leq 3$ . For practical dielectrics used for PCB's, the error without the correction in the denominator was larger than 50 percent.

With the full matrices  $\mathbf{Z}(\omega)$  and  $\mathbf{Y}(\omega)$  the response of the system of coupled transmission lines can be calculated. Djordjević *et al.* [Djo87a] presented an overview of the methods to solve the equations for the coupled lines with linear and non-linear load impedances, both in the frequency and the time domain. We will first consider linear loads in the frequency domain; this allows us to employ the modal expansion of Djordjević and Sarkar [Djo87b], which is similar to the BLT-method [Bau78, Tes97].

### 3.5 Results for bare PCB's

The next subsections show the TL results for boards with passive loads. First the simple track problem of Fig. 3.3 will be addressed in Section 3.5.1, which is extended to more complicated tracks as on practical PCB's in Section 3.5.2. Finally some results for grounding tracks instead of grounding planes are shown in Section 3.5.3.

#### 3.5.1 Straight tracks

For the simple PCB of Fig. 3.3 in the Bersier setup (Fig. 3.2a), the current  $I_1$  is injected in straight track 1 by a voltage-generator source  $V_g$  with impedance  $Z_g = 50 \Omega$ , see Fig. 3.9. Other straight tracks were open-ended at the near end  $A$ , or  $Z_{Ai} = \infty$  ( $i = 2, \dots, 4$ ). The far end impedances  $Z_{Bi}$  ( $i = 1, \dots, 4$ ) are chosen either equal to the characteristic impedance  $Z_m = 68 \Omega$  of the microstrip line, or zero, or very large (open circuit). The CM circuit is short circuited at plate  $A$ ,  $Z_{A5} = 0$ ; the far-end impedance  $Z_{B5}$  was  $R_0 = 150 \Omega$ , a  $100 \Omega$  resistor in series with the  $50 \Omega$  input impedance of the HP 4396A spectrum analyzer. The measured voltage  $V$  (Fig. 3.2a) over the input impedance was converted to the CM current. The  $100 \Omega$  resistor bridged a  $g = 1$  cm gap between the GP and the brass plate  $B$ .

Figure 3.10 shows the measurements and the TL model results for the current transfers  $I_{CM}/I_1$  and  $I_{CM}/I_2$ , for injection into track 1 or 2. All four tracks were terminated into  $68 \Omega$  near brass plate  $B$ .

The measurements can also be described reasonably well by the simple model of Fig. 3.2b.

$$\frac{I_{CM}}{I_{1,2}} = \frac{Z_T(\omega)I_{1,2}/150}{I_{1,2}} = \frac{j\omega M_{s1,2}}{150}, \quad (3.22)$$

since  $Z_T(\omega) \simeq j\omega M_{s1,2}$ , with  $M_{s1,2}$  the mutual inductance between CM and DM circuit; see the dotted curve in Fig. 3.10.

Figure 3.11 shows the current transfers for the DM short-circuit case ( $Z_{Bi} = 0$ ,  $i = 1, \dots, 4$ ) and DM open case:  $Z_{Bi}$  large,  $1 \text{ M}\Omega$  in the calculations. The markers indicate the resonant-frequencies  $f_{rDM}$  of the DM circuit, where the input-current  $I_{1,2}$  is minimal;

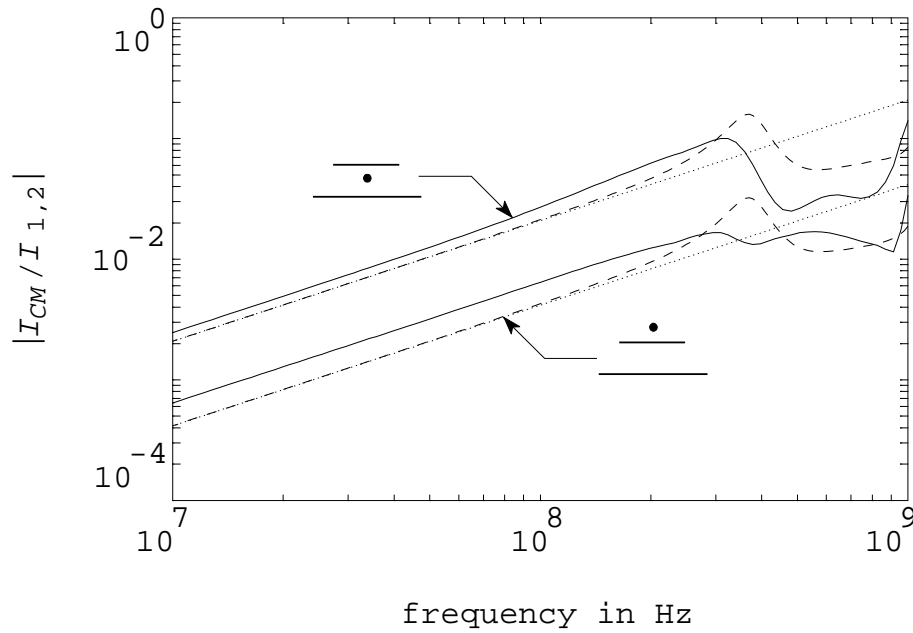


**Figure 3.10.** Measured (—) and calculated (---) current transfer between DM and CM circuits of the Bersier setup (Fig. 3.2a); the tracks are terminated at the far end of the PCB into their characteristic impedances of  $68\ \Omega$ . The approximation (3.22) is given by the dotted line.

see also Section 3.7. For the shorted case  $f_{rDM} = 200$  and  $600$  MHz, and  $f_{rDM} = 400$  and  $800$  MHz with open ends.

A comparison of Figures 3.10 and 3.11 shows the effect of the termination of the DM circuit. In the latter Figure, the CM current becomes equal in magnitude or even larger than the injected current  $I_{1,2}$  at the  $1/4$  and  $3/4\ \lambda$  DM resonances. This is more than a decade larger compared to the  $Z_m$ -terminated tracks of Fig. 3.10. In addition, the current transfer may vary over 60 dB within an octave. Such current transfer may cause EMC problems with modern MOS circuits, which usually have high input impedance and low output impedance. One should avoid the excitation of the DM resonances by digital devices, e.g. by providing appropriate damping. As an alternative, the coupling may be reduced by applying a dielectric thinner than the 1.5 mm in this experiment.

The CM resonances are manifestly absent in the current transfer. The current and voltage distributions along the CM circuit at resonance do not match those in the DM circuit. In addition, the propagation velocity differs for both circuits; the wave velocity for the CM circuit is slightly larger. The CM current shows deep dips due to the distributed coupling via  $M_s$  and  $C_{1,CM}$ . Such TL effects can also be discussed along the lines presented earlier by Vance [Van78, pp. 147-150]. The frequency at which the dips occur depend on the termination of the DM circuit, as is apparent from a comparison of Figs. 3.11a and b.

### 3.5.2 More complicated tracks

We now address more complicated tracks. Many experiments were carried out; for this presentation we selected those which we consider to be a critical test of the TL method and an indication of the limits of its applicability.

First we present the results on a PCB with a double bend in track 1 at half its way over the GP (inset upper part of Fig. 3.12). The current  $I_1$  is again injected in track 1 (TL1)

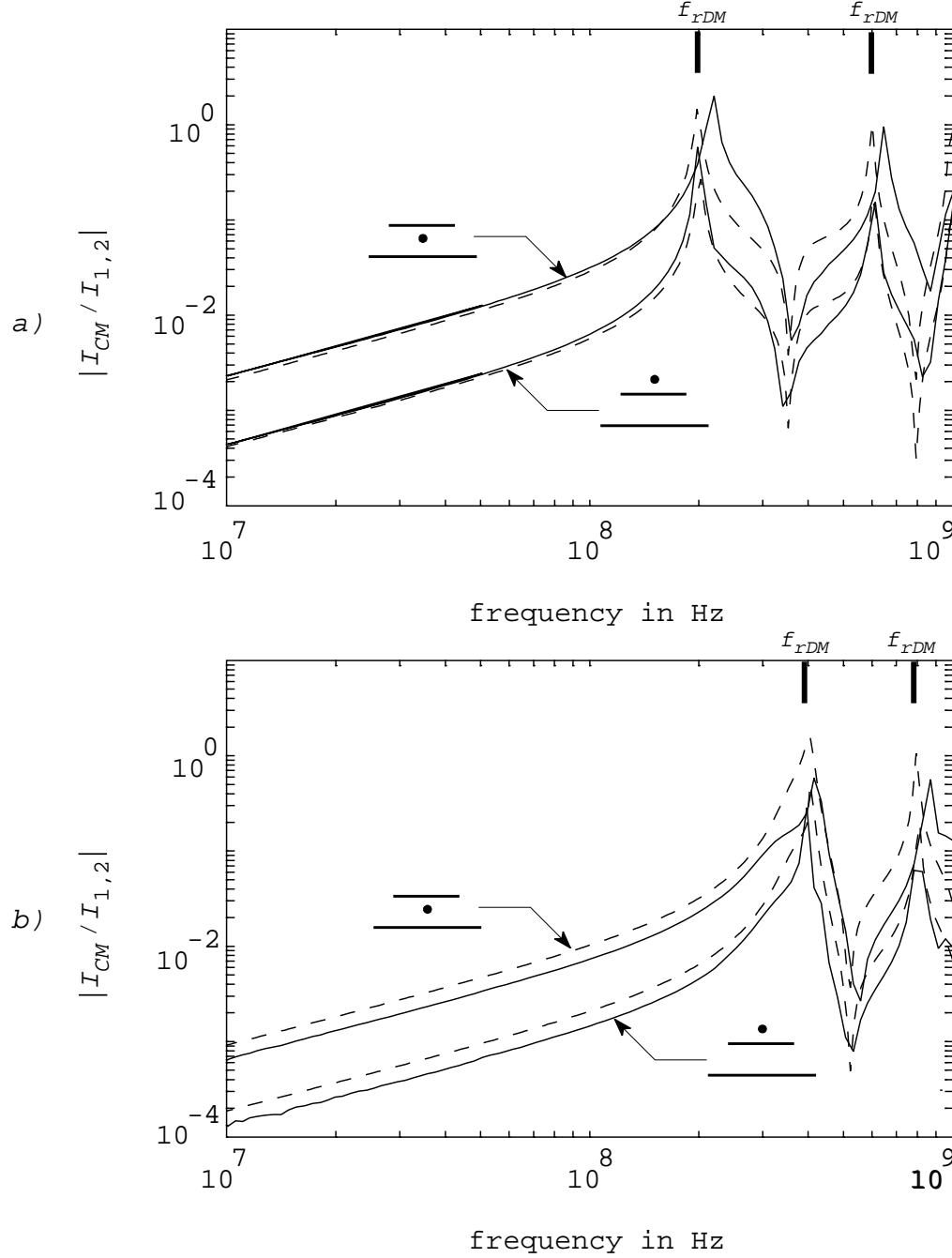


**Figure 3.11.** Measured (—) and calculated (---) current transfer between DM and CM circuits of the Bersier setup (Fig. 3.2a). The tracks are a) shorted and b) opened at the far end of the PCB. The markers  $f_{rDM}$  show the resonant frequencies in the DM circuit.

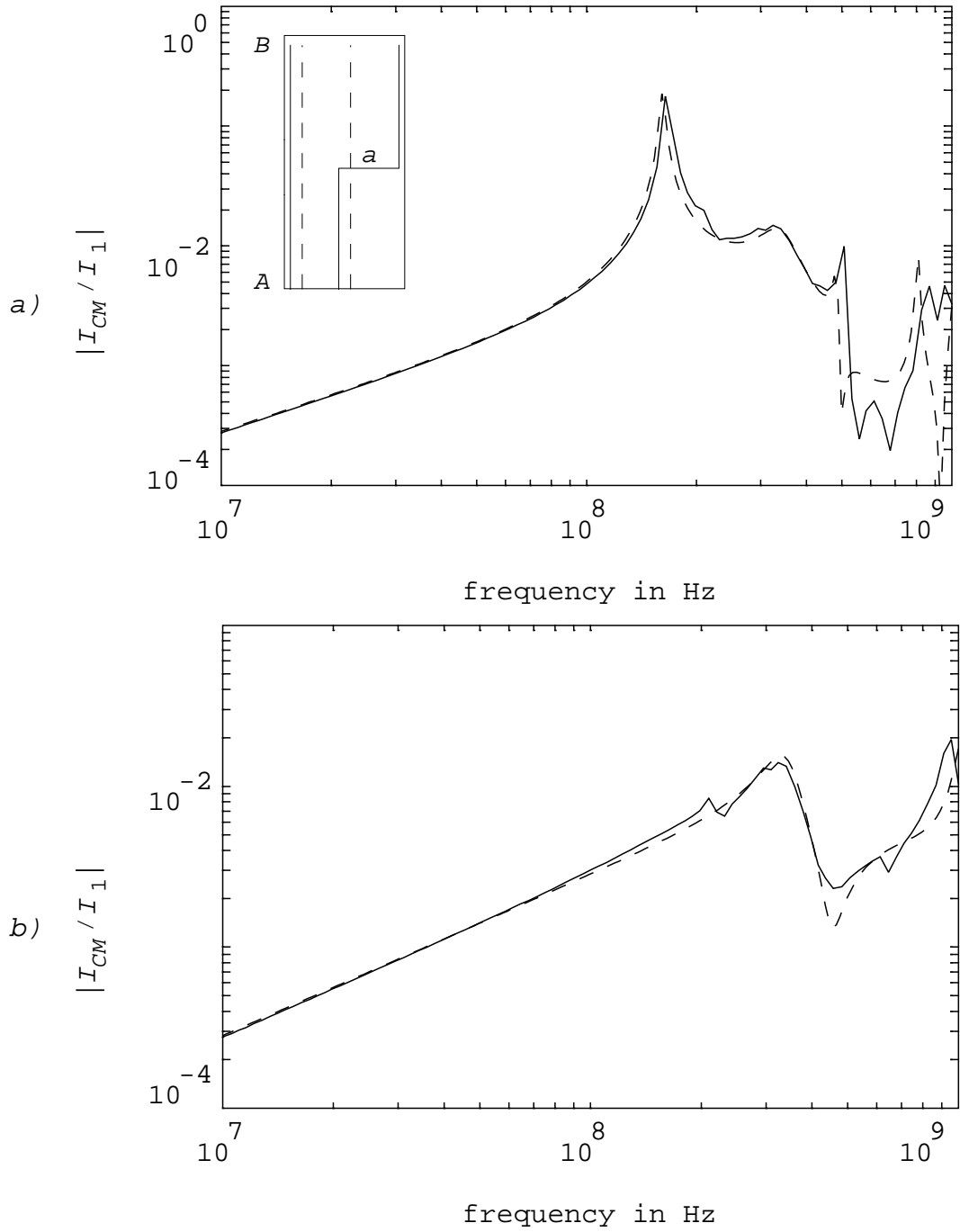


**Figure 3.12.** a) The measured (—) and calculated (---) current transfer  $|I_{CM}/I_1|$  between the DM circuit of track 1 and the CM circuit. The current  $I_1$  is injected at side A (see also Fig. 3.2). The inset shows bent track 1 and track 2 (—) on the upper layer of the PCB) and tracks 3 and 4 (---) on the lower layer. All tracks are open ended end at side B. b) The same current transfer with the tracks terminated into  $Z_m = 68 \Omega$  at end B.

by a voltage source  $V_g$  with impedance  $Z_g = 50 \, \Omega$ . The other DM tracks are open ended at the near end  $A$ . The CM termination impedance  $Z_{A5}$  is zero and  $Z_{B5} = R_0 = 150 \, \Omega$ . Figure 3.12 shows the DM to CM current transfer with all tracks open ended to the GP near the end  $B$  ( $Z_{Bi} = \infty$ ,  $i = 1, \dots, 4$ ) or with the tracks terminated there into the characteristic impedance ( $Z_{Bi} = 68 \, \Omega$ ,  $i = 1, \dots, 4$ ).

In the TL model, each of the parallel segments are described as in the previous Section, with proper values for the off-diagonal elements in  $\mathbf{Z}$  and  $\mathbf{Y}$ . The short perpendicular part  $a$  mainly acts as an intermediate DM delay line. The CM circuit under part  $a$  is modeled as a TL section of the same length, with its inductance and capacitance modified such that the speed of propagation is a factor 50 larger, but the characteristic impedance remains constant. No magnetic coupling is expected between DM part  $a$  and the CM circuit. For the capacitive coupling we adopted two models which gave similar results. Either the total  $C_{a-CM}$  was evenly distributed over section  $a$ , or it was lumped in two halves at both ends of section  $a$ . Implicitly we neglected the variation of  $C_{a-CM}$  over the length.

The thus adapted TL calculations agree quite well with the measurements. The 160 MHz peak in the shorted case is the first quarter-wavelength resonance of track 1. The maximum current transfer is smaller than encountered in the previous Section, but still reaches values of about 0.2 for the open-ended tracks.

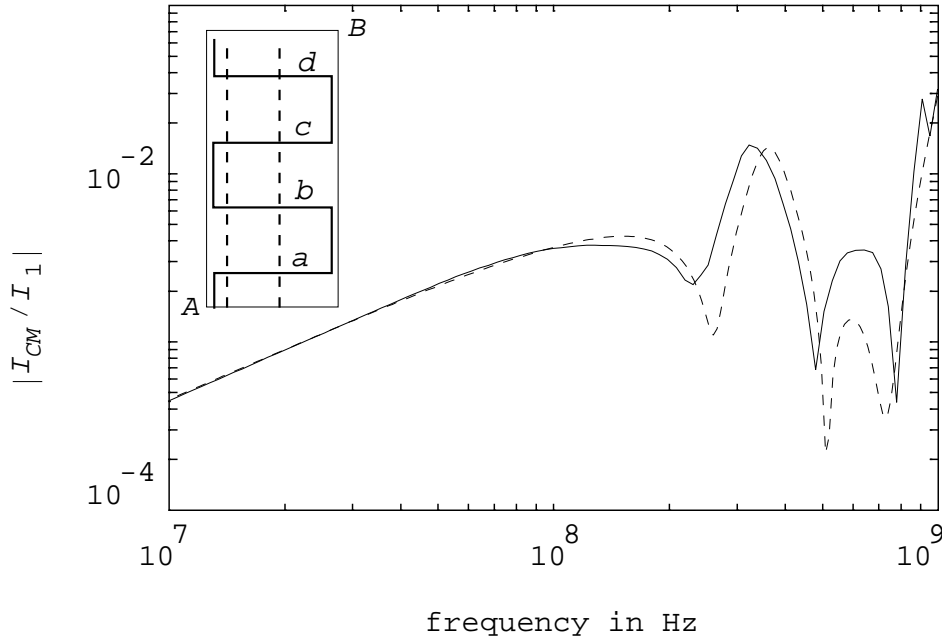


**Figure 3.13.** The measured (—) and calculated (---) current transfer between the DM circuit of track 1 and the CM circuit. The current  $I_1$  is injected at side  $A$  (see also Fig. 3.2). The inset shows the meandering track 1 (—) on the upper layer of the PCB and tracks 3 and 4 (---) on the lower layer. All tracks are terminated into  $Z_m = 68 \, \Omega$  at the far end  $B$ .

Figure 3.13 shows the current conversion of a second and much more complicated PCB. Track 1 (e.g. a supply track) meandered over the upper surface as shown in the inset of Fig. 3.13. The four perpendicular parts  $a$  up to  $d$  are again modeled as DM delay lines with couplings to the CM circuit as described above. All tracks were terminated into  $Z_m$  at  $B$ . The general behavior of the current conversion as a function of frequency is still correctly calculated.



### 3.5.3 Ground track

We now consider a PCB where the ground plane is replaced by a ground track. On such a PCB both the DM-DM and the DM-CM coupling are large. Nevertheless, such PCB's can be found in practical equipment, when for example low costs are important, or slow devices are employed, or additional EMC measures reduce the coupling with other PCB's and with the environment.

The inset of Fig. 3.14 shows the cross section of a three-layer PCB with four DM tracks (1, 2, 3 and 4) which are kept close to a ground track 5; all straight tracks were 20 cm long. The characteristic impedance of track 1 and 3 is  $Z_{m1,3} = 426 \Omega$  (referenced to track 5); that of track 2 and 4  $Z_{m2,4} = 102 \Omega$ . As with the PCB's discussed before, the near end *A* of the exited tracks is terminated into the  $50 \Omega$  of the spectrum analyzer; the non-exited tracks, except track 4, are open ended there. At the far end *B*, the DM tracks were terminated into the different impedances toward ground track 5:  $Z_{B1,3} = 470 \Omega$  and  $Z_{B2,4} = 100 \Omega$ . Tracks 4 and 5 were shorted to each other at both ends. In the Bersier setup this structure was placed at  $h_{CP} = 1$  cm above the CP; the gap  $g$  was again 1 cm.

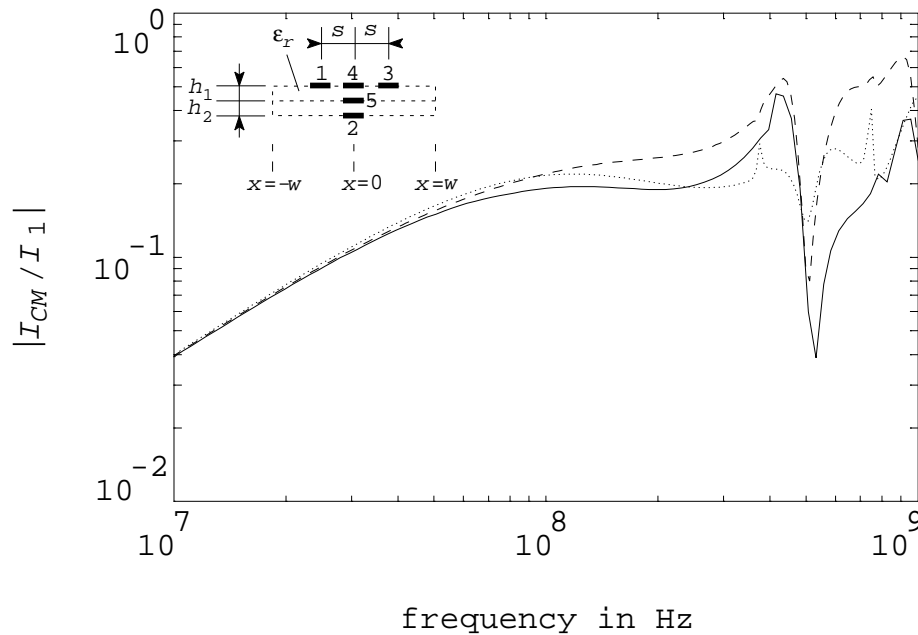


**Figure 3.14.** Measured (—) and calculated (---) current transfer  $I_{CM}/I_1$  for the 5 track problem shown in the inset. The  $2w = 10$  cm wide PCB consisted of three DM tracks 1, 2, and 3, and two grounding tracks 4 and 5; the upper tracks were  $s = 10$  mm separated and all tracks were of width  $b = 1.5$  mm. Tracks 1 and 3 were terminated into  $470 \Omega$  resistors with track 4, while track 2 was terminated into a  $100 \Omega$  resistor with track 5. The three resistors were in the model paralleled with a stray capacitance of 1 pF at the far end *B* (see main text); for comparison curve ( $\cdots$ ) gives the current transfer with no stray capacitance. The grounding tracks 4 and 5 were shorted at both ends.

Figure 3.14 shows the measured and calculated current transfer for excitation of track 1. In the TL model track 5 was assumed as reference. The transfer at low frequencies  $f < 64$  kHz (not shown in Fig. 3.14) corresponds to the parallel resistance of tracks 4 and 5, which is  $38 \text{ m}\Omega$ . The capacitive and inductive TL parameters were obtained by the MOM calcula-

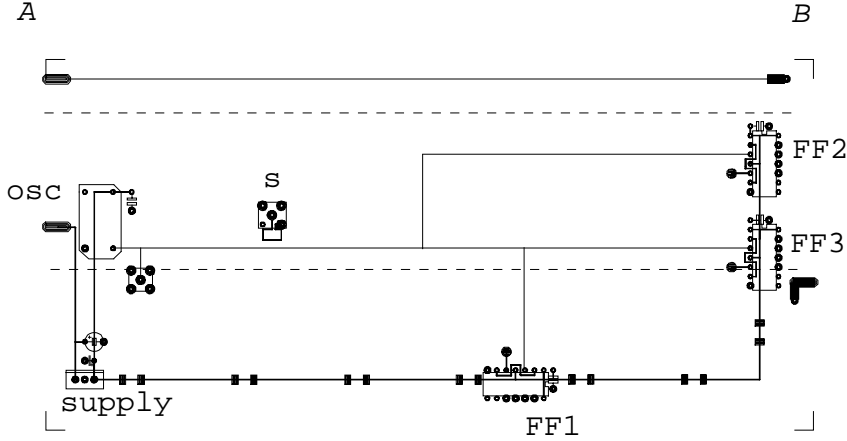


**Figure 3.15.** Top view of the HCT board with three D flip flops (FF's) and a clock oscillator (OSC). The solid lines indicate the tracks at the upper layer of the PCB, the dashed lines those at the lower layer. Apart from the signal track three test tracks were incorporated. The DM current is measured with inductive current sensors  $s$ . The supply voltage was regulated by a stabilizer.

tions. Comparing the data shown with Fig. 3.10 one finds that the  $M_s$ -coupling is larger by more than an order of magnitude. The high frequency coupling ( $f > 300$  MHz) is about a factor of 5 larger.

The dip at 500 MHz in the current transfer may be explained by a parasitic capacitance of the terminating resistors. A parallel capacitance of 1 pF (obtained by fitting) changes the current and voltage distribution in the DM circuit ( $\omega RC = 1.6$  at 500 MHz), and suffices to essentially reproduce the dip. Other causes are discussed in Sections 3.7 and 3.8.

### 3.6 Demonstration boards with digital logic

Two demonstration boards were designed with three D flip-flops (HCT: 74HCT74 and HLL: 74HLL33534) driven by a clock oscillator. Flip-flops (FF's) were preferred over gates, since a FF is the simplest device with activity at other than the clock frequency. In Fig. 3.15 the HCT board is shown; the layout of the HLL board is similar. Each FF had its own branch of the clock trace. This provided some complexity, but still kept the bookkeeping effort manageable. The TTL compatible quartz crystal oscillators (OSC) had fundamental frequencies  $f_0$  of 10 MHz, 20 MHz, 50 MHz, and 100 MHz (the last one only for the HLL board); a translator  $T$  (74HLL33244) placed near the oscillator on the HLL board transformed the 5 V signal into a 3.3 V signal.

We measured the actual DM current delivered by the clock. An inductive sensor  $s$  was placed at the position indicated; the mutual inductance  $M_{sens}$  with respect to the clock signal track was 0.97 nH for the HCT print, and 0.29 nH for the HLL print. The sensor output  $V_{sens}$  was integrated numerically:  $I_{DM}^m = V_{sens}/j\omega M_{sens}$ . The PCB was again mounted in the Bersier setup of Fig. 3.2a, with the oscillator near side A. The external power was also provided from side A. The on-board voltage stabilizer is indicated by 'supply' in Fig. 3.15; high frequency decoupling capacitors were placed nearby the stabilizer and nearby each IC. The CM current was measured at end B by the spectrum analyzer. The resolution and

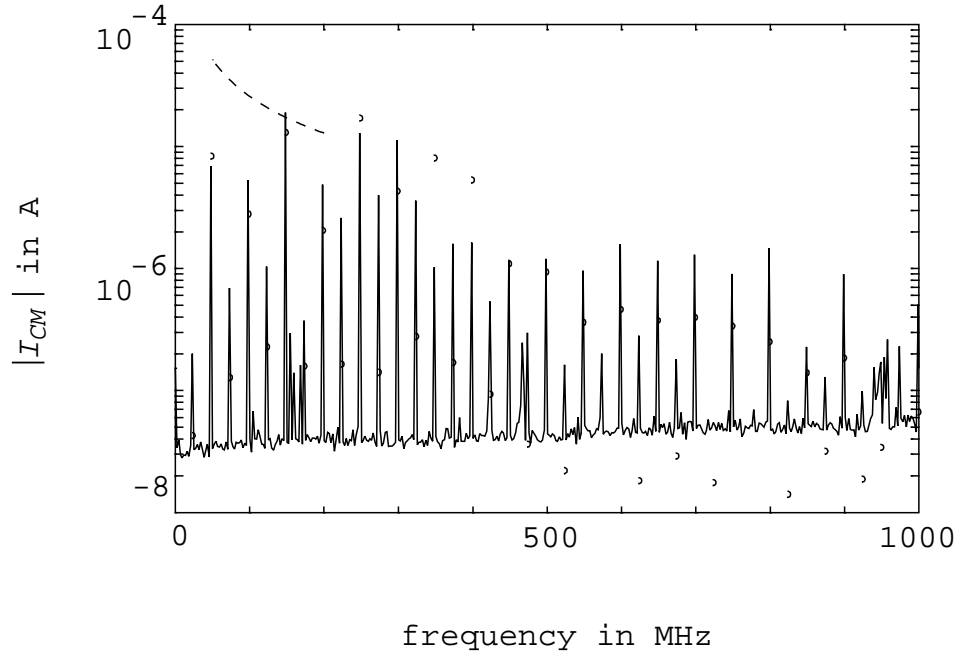


**Figure 3.16.** Measured (—) and calculated (o) spectral component of the common-mode current  $I_{CM}$  in the Bersier setup for the HCT board with 50 MHz clock speed. The dashed line shows the upper bound for a single straight track located at the mid position at the upper side of the PCB; the experimental parameters used in Eq. (3.14) were  $M_s = 1.43 \text{ nH/m} \times 0.2 \text{ m} = 0.29 \text{ nH}$ ,  $\tau = 2.4 \text{ ns}$ , and  $\Delta i = 51 \text{ mA}$ .

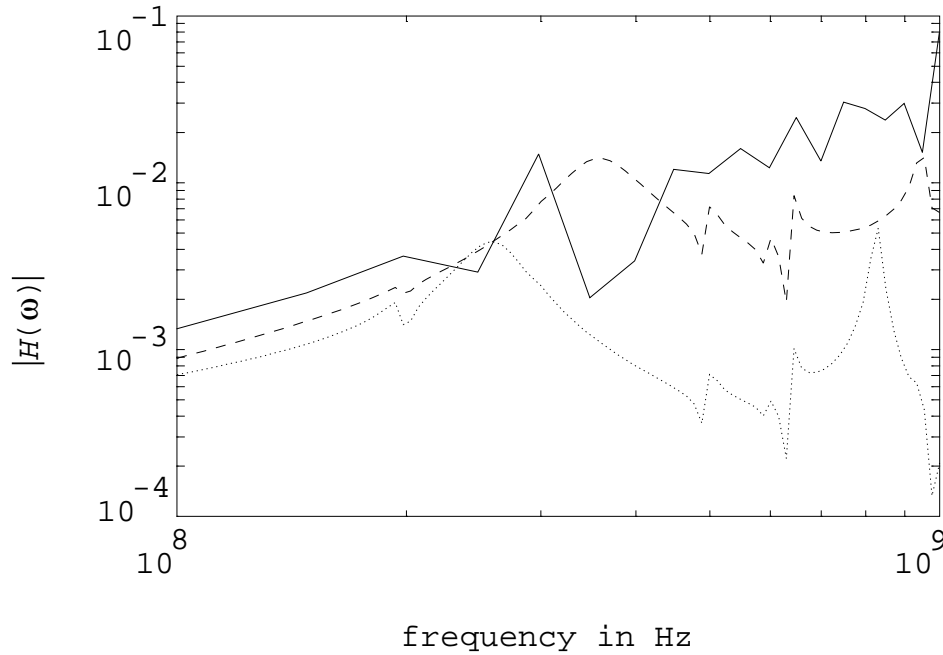


**Figure 3.17.** Measured transfer function  $H(\omega)$  of the HCT board with 50 MHz oscillator (—) and the calculated  $H(\omega)$  for  $C_g = 0 \text{ pF}$  (- - -) and  $C_g = 10 \text{ pF}$  ( $\cdots$ ).

**Table 3.2.** Mean and maximum deviation between measured and calculated harmonics of  $f_0$  in the CM current for HCT and HLL boards;  $f_m$  indicates the frequency where the maximum deviation occurs. The frequency range considered was 10 MHz – 600 MHz.

| $f_0$ [MHz] | HCT       |           |             | HLL       |           |             |
|-------------|-----------|-----------|-------------|-----------|-----------|-------------|
|             | mean [dB] | max. [dB] | $f_m$ [MHz] | mean [dB] | max. [dB] | $f_m$ [MHz] |
| 10          | 5.5       | 18.3      | 400         | 5.5       | 16.8      | 350         |
| 20          | 5.4       | 17.4      | 580         | 4.5       | 16.5      | 480         |
| 50          | 6.6       | 15.1      | 350         | 7.0       | 18.6      | 400         |
| 100         | -         | -         | -           | 4.9       | 9.8       | 400         |

video bandwidth (RBW and VBW) of the analyzer were both 30 kHz and the frequency span was 100 kHz – 1.82 GHz.

In the TL model the devices were simplified/linearized according to an IBIS (Input/output Buffer Information System) model. The output impedances ( $Z_g$  in Fig. 3.9) of the Thévenin equivalent models for the oscillator and the translator  $T$  were 20 and 12  $\Omega$ , which provide some damping of the DM circuit. The rise and fall times of the unloaded voltage source ( $V_g$  in Fig. 3.9) were measured separately, about 2 ns for HCT and 1 ns for HLL. The input impedance of the FF is a capacitance of  $C_i = 3.5$  pF for both types of logic. The minor nonlinearity of the capacitance, due to the Miller effect inside the IC's, was neglected. We preferred not to calculate the DM current from the available data for the IC's, because of the many implicit assumptions for the parameters. Still, our approach to determine the DM current distribution involves several IC parameters.

In order to assess the current transfer, we first assumed a voltage source of 1 V at the oscillator, and calculated the resulting DM current  $I_{DM,s}$  seen by the current sensor  $s$  for a large number of frequencies. Knowledge of  $I_{DM}$  at one place suffices, since both forward and backward waves are taken into account in the linearized TL model. We then determined the transfer function  $H(\omega) = I_{CM}/I_{DM,s}$  from the TL model and calculated the  $I_{CM}$  through the 150  $\Omega$  load from the measured  $I_{DM,s}$  with the devices operating.

As an example, Fig. 3.16 shows the spectrum of  $I_{CM}$  for the HCT board with a 50 MHz clock. The measured current transfer  $|H(\omega)|$  for the same clock speed (—) and the calculated transfer function (- - -) are given in Fig. 3.17; the curve ( $\cdots$ ) is discussed in Section 3.7. Table 3.2 shows the average deviation in dB between the measured and calculated  $I_{CM}$ , as well as the maximum deviation which occurred near  $f_m$ . The frequencies considered ranged between 10 MHz – 600 MHz. The branches in the HCT board clearly reduce the amplitude of the resonances in the current transfer, as is apparent when the  $H(\omega)$  of Fig. 3.17 is compared to the one for straight open ended tracks, Fig. 3.11b. The measured  $I_{CM}$  reaches values well over the 3  $\mu$ A limit. Without additional EMC measures this PCB proper does not comply with EMC regulations.

Measurements and calculations agree within 7 dB on the average. The maximum deviation, up to about 19 dB, is restricted to one or a few spectral components near the frequency  $f_m$  mentioned in the Table. We compared the experimental transfer functions for one type of logic (HCT) but with different clock frequencies. Large and abrupt variations in the measured  $|H(\omega)|$  between subsequent harmonics were found near  $f_m$  as in Fig. 3.17, also at the lowest clock frequency. The calculated  $H(\omega)$  were of course identical, since the electronics remained essentially the same; this  $|H(\omega)|$  also showed smaller resonances above

$f_m$ . Where these resonances occurred, depended on many parameters, primarily on the difference in propagation speed in the DM and the CM circuit, and on the termination of the DM circuit. The actual values of the inductive and capacitive DM-CM coupling coefficients of the tracks were less decisive.

Since the FF's act as dividers, subharmonics are present in the measured DM and CM currents. We checked two possible coupling paths towards the CM circuit: a) directly from the clock tracks, and b) from the supply track. For coupling a) we calculated the transfer function between the clock track and the CM circuit, assuming a synchronous source for the subharmonics at all FF's. It turned out that this transfer is too small by an order of magnitude to explain the measured subharmonics in  $I_{CM}$ . As a consequence, the even terms of the subharmonics do also not significantly influence the harmonic components. Coupling b) was minimized by a careful placement of decoupling capacitors, as was verified by separate measurement of the subharmonic content of the supply current. The small peaks at  $f \simeq 160$  MHz, 470 MHz and 950 MHz are signals from nearby communications. This was verified by switching off the power to the PCB; the communication peaks remained. The equipment was not placed in a shielded room.

Both effects, abrupt variations in  $|H(\omega)|$  near  $f_m$  and large subharmonic amplitudes in  $I_{CM}$ , may have a common origin in a local coupling at the devices. This coupling is not included yet in the TL model based on the traces. For a passive component, a local off-diagonal capacitance and a mutual inductance could be selected. Each active device will act as a local series voltage source, and a parallel current source with respect to the CM circuit. As a test, we placed a small copper electrostatic shield near FF2 and FF3, at the edge of the GP. The variations in  $H(\omega)$  near  $f_m$  were reduced indeed. Also the measured subharmonic amplitudes became smaller relative to the harmonics, certainly for the 10 and 20 MHz clock frequencies. A magnetic shield was not tested.

### 3.7 Additional coupling effects

We chose to present the TL model results as current transfer between the DM and CM circuits. The DM circuits and the currents should in principle be known to the designer of a practical PCB. In particular for fast digital electronics, the DM currents may be large. The CM currents are the prime vehicle of interference, both in immunity and in emission. In our Bersier approach we decided to interconnect GP and CP at the DM current input side; the CM current is determined at the other end of the PCB. This allowed well-defined closed current loops for both the DM and the CM circuit, and enabled us to measure the CM currents in a direct way. As a consequence, the inductive/resistive DM-CM coupling will already be important at low frequencies. Other choices for the CM circuit will result in a different current transfer. For instance, one could leave the CM circuit open at both ends. The capacitive coupling will then be more important than in our setup.

One should be careful when a CM current is injected in the same setup, in order to assess the immunity of the DM circuits. The interference current at the inputs of devices is then described by a different  $H(\omega)$ , which again depends strongly on the position of the tracks and devices. This is no violation of reciprocity, which relates the current in one circuit to a voltage in another. Both current transfers, from DM to CM and vice versa, are correctly described in the TL method.

Experiments taught us that for smaller distances the parasitic capacitance  $C_g$  between the GP and the brass plate  $B$  becomes important in two respects. First, the  $C_g$  is a path for  $I_{CM}$  parallel to the  $150\Omega$  resistor. Only the part through the resistor is actually seen by

the spectrum analyzer. Second,  $C_g$  alters the impedance seen at the input of the CM circuit at the connector in plate  $B$ . We calculated  $C_g$  in a 2D model for the gap; Fig. 3.18 shows  $C_g$  for several situations. The dielectric layer on the PCB increases  $C_g$ , whereas the nearby CP lowers  $G_g$ . For a 5 cm wide GP we found  $C_g$  equal to 3.5 pF in case of a 0.5 mm gap. Measurements indicated an even larger value,  $C_g \simeq 10$  pF, with only a slight dependence on the gap size  $g$  if smaller than 1 mm; then  $\omega R_0 C_g = 1$  at 100 MHz. In Fig. 3.17 we presented the calculated current transfer for the HCT board with  $C_g = 0$  pF (---) and 10 pF (···). Our choice of the 1 cm gap at end  $B$  of the GP is a compromise in the experiments. A larger gap would increase the local contribution of the 100  $\Omega$  resistor to the CM inductance.

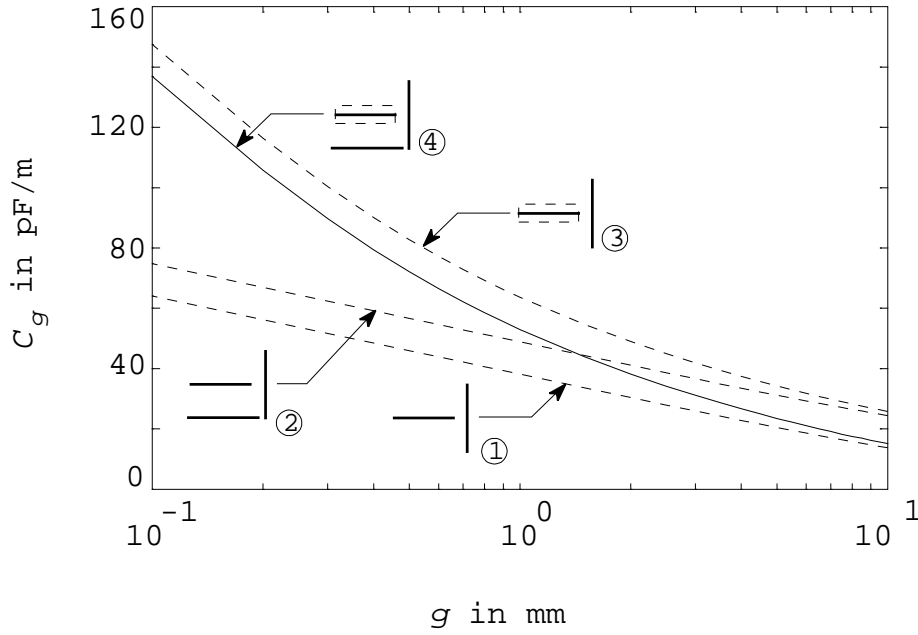


**Figure 3.18.** Calculated capacitance  $C_g$  for different configurations: (1) Ground plane GP at a distance  $g$  from the vertical brass plate  $B$  of height 2 cm, no CP present. (2) The same as (1) but with a 20 cm long CP at a distance  $h_{CP} = 1$  cm below GP. (3) PCB coated with a dielectric  $\epsilon_r = 4.7$  at a distance  $g$  from plate  $B$ . (4) The coated PCB with plates CP and  $B$ .

A smaller direct capacitive coupling can also be expected between each DM track or the devices and the brass plate  $B$ , certainly when the track is open ended. This has not been studied in detail.

### 3.8 Concluding remarks

The proposed TL method estimates the equivalent sources for the common-mode current on a cable connected to a PCB quite well. For complicated tracks the TL method starts to deviate above approx. 400-500 MHz. For digital circuits, the first few harmonics dominate the spectrum above 30 MHz, for which the current-injection or Bersier method is applicable. At these frequencies, the TL method is particularly accurate.

Different methods exist to describe the EMC properties of a circuit. The simplest one is the lumped-circuit model, which is particularly useful at low frequencies. Other advantages are the familiarity of many designers with the model, its applicability to the DM circuits proper, and the amount of insight which can be obtained from the model. If ground planes

and conductors are split up into smaller parts, more involved models result, such as the partial-element analysis proposed by Ruehli [Rue74] or the circuit analysis implemented in Fasterix [Clo94]. Delay effects can also be incorporated into the models [Gar97]. If good accuracy is required for the small DM-CM couplings, the constituent parts should be made small, and the computation time increases dramatically.

Our main interest to investigate the merits and limitations of the TL method was the wish to speed up the calculations, in particular when analytical expressions were available for the relevant coupling coefficients. A full  $I_{CM}$  or  $H(\omega)$  spectrum for our demonstration boards is now calculated in less than a minute on a modern PC. The TL method is then very well suited for incorporation in a placement and routing process, to generate early warnings when certain EMC requirements are likely to be violated. A more involved calculation can always be carried out later.

We used the measured  $I_{DM}$  in our TL model. One might prefer to also calculate the DM currents. However, in practice devices may be available earlier than the required IBIS models. In addition, interference sources which reside inside the devices such as processors, are seldom presented in data sheets or files. One then has to resort to measurements anyway [Ber97].

We expect that the TL method can be extended to even higher frequencies when three-dimensional effects are addressed more accurately: local coupling at the devices and the fringing fields at the border of the PCB. In principle the immunity of a PCB with respect to interferences can also be determined by the TL method. The non-linearity of the devices should then be adequately known.

When the harmonics generated by digital circuits nearly coincide with abrupt variations in  $H(\omega)$ , large deviations may be found with respect to measurements. This is true for our method, but also for any other calculation method. The TL method can be extended to include local couplings by devices. Active devices require separate series CM voltage and parallel CM current sources. It would be worthwhile to investigate whether an approach similar to our TL model can also be found for an active device proper. This will certainly be necessary for densely packed PCB's, where the devices may contribute more than the tracks.

# Chapter 4

## Crosstalk on a multilayer printed circuit board and the current distribution in the ground plane

### Abstract

In multilayer printed circuit boards, a ground plane (GP) acts as return for the current through the tracks. The current distribution in the ground plane (GP) has been studied for a triple-layer printed circuit board (PCB). The continuous GP was the middle layer; test tracks in the top and bottom layer were placed at various positions. The crosstalk in terms of a transfer impedance  $Z_t$  between tracks on opposite sides of the GP is particularly sensitive to the current distribution in the GP. General analytical expressions for  $Z_t$  are given; the 2D-calculations rely on different models, each adequate for a specific frequency range. EMC design rules for a proper PCB layout and routing can be obtained. Rapid high-frequency calculations were based on transmission-line (TL) models. The theory was checked by measurements. The TL method gave good results for several boards with bends in the tracks up to 1 GHz.

### 4.1 Introduction

Multilayer printed circuit boards (PCB's) are nowadays often used in modern high-speed analog and digital electronic designs. The ground plane(s) and the lands which distribute d.c. supply voltages extend over a major part of the different layers. The growing importance of high-frequency (HF) power distribution and the associated delta- $I$  noise on (multilayer) PCB's is reflected in the growing literature, see e.g. [Pau92b, Djo93, Fra94, Hub95, Can96, Coe96, Osu97, Zut97]. The current in the ground plane (GP) may originate from three sources. (1) The GP acts as return for a signal track; together with the electronic components at the ends of the track, a closed signal loop or differential-mode (DM) circuit is formed. (2) The GP carries the common-mode (CM) current which may arrive at the PCB via cables connected to the PCB, see also Chapter 3. (3) An external perpendicular magnetic field and electric field lines ending on the GP may induce circulating currents in the GP which cause interference signals into DM circuits. The current distribution over the plane is important for crosstalk between different signal circuits on the PCB, for sensitivity with respect to external disturbances, and for generation of such disturbances [Ber94, Hoc97]; the latter important CM current generation is reported in [Hor97a, Hor97b, Hor97c] and Chapter 3.

In the past, numerous crosstalk studies focused on two (or more) circuits on the same side of a GP; see [Gra92] for a literature review. The GP in these studies is often assumed to be of infinite size and a perfect conductor; this high-frequency limit is certainly relevant for





current loops with proper self inductances. In mathematical terms, our 2D magnetic vector potential always goes to zero for large distances. This approach circumvents the introduction of (partial) inductances which refer to infinite distances.

The spurious couplings require considerable accuracy in the calculations; therefore the analytical and numerical results are compared to check consistency and accuracy. To retain clarity of the paper, all mathematical details are deferred to appendices. In Section 4.2 we discuss a physical picture for the current distribution and the DM-DM crosstalk which provides a simple way to understand the results for our PCB in Fig. 4.1. Section 4.3 describes the calculations and additional results. The proximity of a metal cabinet panel (CP) influences the magnetic field and alters the DM to DM crosstalk; in Section 4.4 we present a selection out of the many possible configurations. A signal track between two ground planes and its coupling to another DM circuit outside these planes is studied in Section 4.5. In Section 4.6 the TL model is introduced and the results are compared with measurements. More complicated tracks terminated into different impedances are treated in Section 4.7. The same TL model was extended to describe the conducted emission or susceptibility of a PCB, which included a comparison with measurements on actual digital logic, see Section 3.6 and [Hor97a, Hor97b, Hor97c].

In Sections 4.2–4.5, the finite width tracks are represented by filamentary wires; these wires are then at the middle positions of the corresponding tracks. The actual tracks of width  $b$  are taken into account in Sections 4.6 and 4.7, in order to incorporate the proper self inductances and capacitances.

The experimental triple-layer PCB was 20 cm long and consisted of a single- and a double-layer PCB firmly pressed against each other. The copper layer had conductivity  $\sigma = 5.8 \cdot 10^7 \Omega^{-1}\text{m}^{-1}$  and thickness  $d = 30 \mu\text{m}$ . Different GP's of various widths were studied. The 1.5 mm wide tracks were placed at  $h_{1,2} = 1.5 \text{ mm}$  above and below the GP (see Fig. 4.1). The epoxy layers had a dielectric constant  $\varepsilon_r$  of 4.7. The GP was connected over the full width to the brass plates, which minimized end effects. Measurements between 10 Hz–100 kHz were carried out with an active current probe, sine-wave generator and lock-in detector. Between 100 kHz and 1 GHz we used a network analyzer. Proper care was taken to ensure the EMC quality of the measuring system: we only used SMA connectors and double-braided RG223 cables. The measuring equipment was placed in a special EMC-cabinet [Hou89].

## 4.2 Current Distribution and $Z_t$

For a physical picture of the phenomena governing the per unit length transfer impedance  $Z_t$ , we consider the  $Z_t(1-2)$  between filamentary tracks 1 and 2, for the moment centered ( $x_{1,2} = 0$ ) on the GP ( $2w = 5 \text{ cm}$ ), but at opposite sides. The origin of the coordinate system is at the center of the upper surface of the GP. The current  $I_1$  is injected in track 1 and returns via the short circuit and the GP. The DM voltage  $V_{DM}$  between track 2 and the GP is determined at the sending end for the current. Faraday's law for time harmonic signals  $\oint \mathbf{E} \cdot d\mathbf{l} = -j\omega\Phi$  yields

$$\begin{aligned} V_{DM} &= \int_a^b E_z(x, -d) d\zeta + j\omega\Phi \\ &= E_z(x, -d)\ell + j\omega\Phi \\ &= Z_t I_1 \ell, \end{aligned} \tag{4.1}$$

where  $\Phi$  is the flux through the rectangle  $a-b-c-d-a$  in Fig. 4.2. The electric field  $E_z(x, -d)$  at the lower surface of the GP is related to the local current density by  $J_z(x, -d)/\sigma$ . The 2D assumption allows the simplifications as given in the second and third line of Eq. (4.1); here  $Z_t$  is the transfer impedance per unit length.

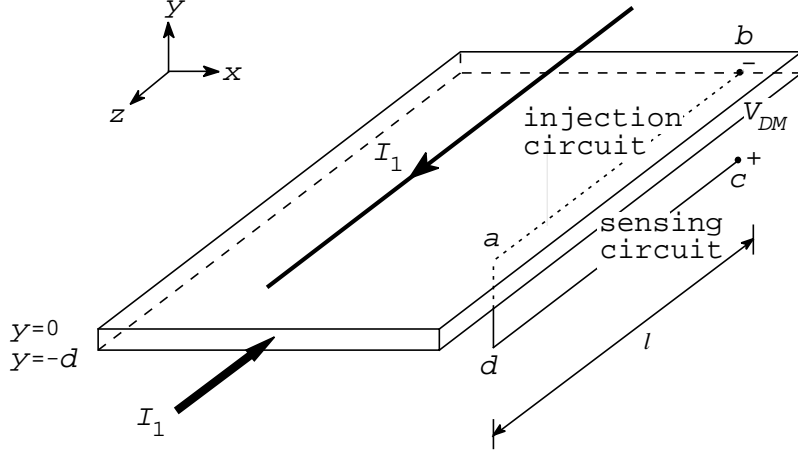


**Figure 4.2.** The voltage  $V_{DM}$  measured between  $c$  and  $b$  is determined by the  $E_z$ -field along the line  $a-b$  and the flux through the area  $a-b-c-d-a$ .

The solid line in Fig. 4.3a shows the general behavior of  $Z_t(1-2)$  for a thin GP without skin effect; for calculations see Section 4.3. Figure 4.3b shows the absolute values of three contributions to  $Z_t$ : a)  $E_z(0, -d)$ , and the flux between the GP and track 2 as b)  $j\omega\Phi_1$  due to the vacuum magnetic field of track 1, and c)  $j\omega\Phi_{GP}$  due to the current density in the GP. We can write the volume current density  $J_z$  as a sheet current density  $K_z$

$$K_z(x) = \int_{-d}^0 J_z(x, y) dy, \quad (4.2)$$

or simpler here:  $K_z(x) = dJ_z(x, y)$ . Note that at low frequencies the variation of  $J_z(x, y)$  with depth  $y$  in the GP may be neglected. The  $E_z$  is then proportional to  $K_z$ , according to  $E_z(x, -d) = R_{\square} K_z(x)$ , where  $R_{\square} = 1/\sigma d$  is the sheet resistance of the GP.

Below 1 kHz (region 1 in Fig. 4.3a) the current density  $K_z$  is also homogeneous in the  $x$ -direction. The  $Z_t$  is given by the d.c. resistance of the GP,  $Z_t(\omega = 0) = R_{\square}/2w$  or 11.5 mΩ/m for our PCB. The vacuum magnetic field due to the current in track 1 and the current in the GP fully penetrate the GP (Fig. 4.4a). The flux contributions to  $Z_t$  are still negligible. Above 1 kHz the  $J_z$  concentrates under the track (Fig. 4.4b) in order to expel the magnetic field out of the GP. The  $E_z$  contribution to  $Z_t(1-2)$  increases. At 300 kHz (region 3) the current distribution in the GP in the vicinity of track 1 becomes nearly independent of frequency. Its value tends to

$$K_z(x) = -\frac{I_1}{\pi} \frac{h_1}{x^2 + h_1^2}, \quad (4.3)$$

analogous to the electrostatic surface charge distribution induced on the GP by a wire with charge  $q$  per unit length, above that plane, see introductory text books on electromagnetics, e.g. Ramo *et al.* [Ram94]. The  $E_z$  remains proportional to  $K_z$ . The change in  $E_z$  between

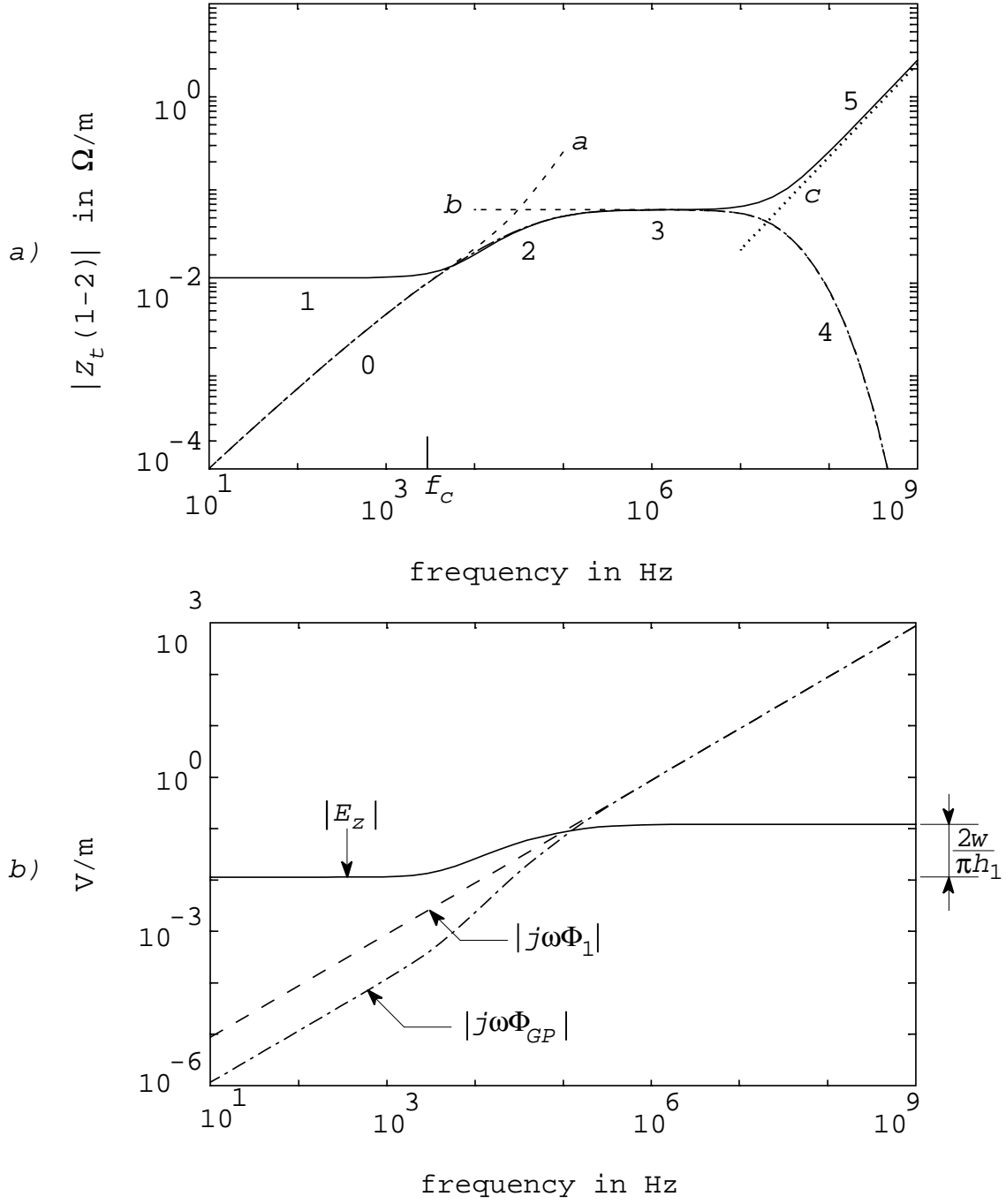


**Figure 4.3.** a) General behavior of  $|Z_t(1-2)|$  between track 1 and 2 with a  $2w = 5$  cm wide GP. The curve 1-2-3-5 (—) is calculated by method of moments (Section 4.3.2). The curve 0-2-3-4 (— · — · —) shows  $|Z_t(1-2)|$  for a very wide ground plane; the skin effect then lowers the  $|Z_t(1-2)|$  in region 4. The curves  $a$ ,  $b$  and  $c$  are discussed in the text, Section 4.3, as is the cross-over frequency  $f_c = 2.9$  kHz from Eq. (4.5). b) Contributions to  $|Z_t(1-2)|$  from Eq.(4.1);  $\Phi_1$  and  $\Phi_{GP}$  represent the flux between track 2 and the GP due to the vacuum field of track 1 and of the GP, respectively.

region 1 and 3 is a factor  $2w/\pi h_1$ , i.e. a factor 10.6 for our PCB (see Fig. 4.3b). The flux contributions lower the change in  $Z_t$ . The total  $Z_t$  is constant over nearly two decades in frequency. Both flux contributions  $j\omega\Phi_1$  and  $j\omega\Phi_{GP}$  become similar in magnitude but opposite in phase. The calculations in Section 4.3 show that the total flux  $\Phi_1 + \Phi_{GP}$  decreases with  $1/\omega$ , which results in the constant  $Z_t$  of Eq. (4.13).

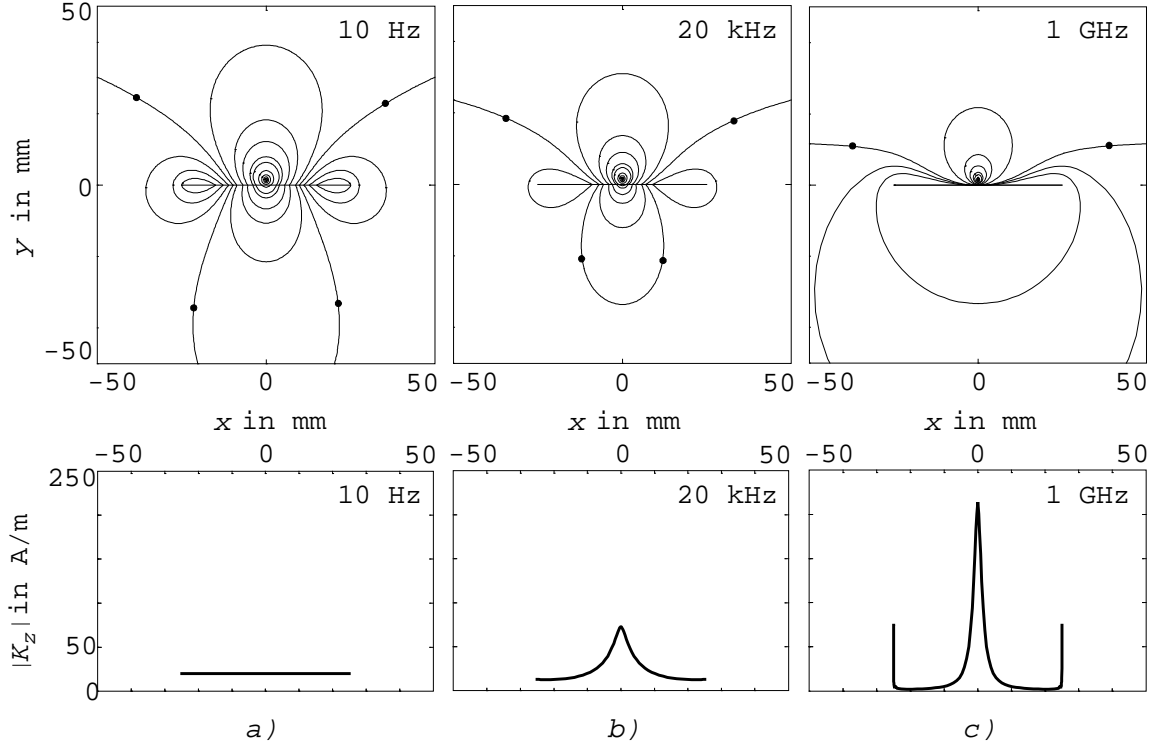


**Figure 4.4.** Magnetic field lines and current distribution  $|K_z|$  in the ground plane ( $2w = 5$  cm) for three frequencies. Only at large distance of the GP the field lines assume the dipolar shape, i.e. closed circles through the dipole. The marked field lines are the separatrices  $A_z = 0$  between the field lines, which at large distance close above or under the GP.

An analogous situation is the more familiar magnetic shielding by a long tube [Laa84] against an external homogeneous axial magnetic field (Fig. 4.5). An external field  $H_e$  produces a flux through the tube  $\Phi_e = \mu_0 H_e \pi r_t^2$ . In the tube wall a circulating current  $I_t$  produces an opposing flux  $L_t I_t$  inside the tube. Here  $L_t = \mu_0 \pi r_t^2 / \ell_t$  is the self inductance of the tube regarded as a long single turn coil of length  $\ell_t$ . The resistance of the tube for the circulating current is  $R_t = 2\pi r_t / d_t \ell_t \sigma_t$ , with  $d_t$  the wall thickness and  $\sigma_t$  the conductivity. We again assume here that the current is homogeneous over the wall thickness. Faraday's law then results in

$$R_t I_t = -j\omega\Phi_e - j\omega L_t I_t. \quad (4.4)$$

At low frequencies,  $\omega \ll R_t/L_t$  the total flux inside the tube  $\Phi_e + L_t I_t \simeq \Phi_e$  because the current  $I_t$  is low. At high frequencies the flux tends to zero as  $\Phi_e R_t / (R_t + j\omega L_t)$ . A voltage induced in a loop inside the tube becomes independent of frequency when the external field  $H_e$  is kept constant, which implies that the induced current is almost constant. The cross-over frequency is given by  $\omega L_t = R_t$  or  $r_t d_t = \delta^2$ . Here  $\delta = \sqrt{2/\omega\mu_0\sigma_t}$  is the skin depth for the tube with  $\mu_r = 1$  because the flux inside the tube is involved rather than the flux in the

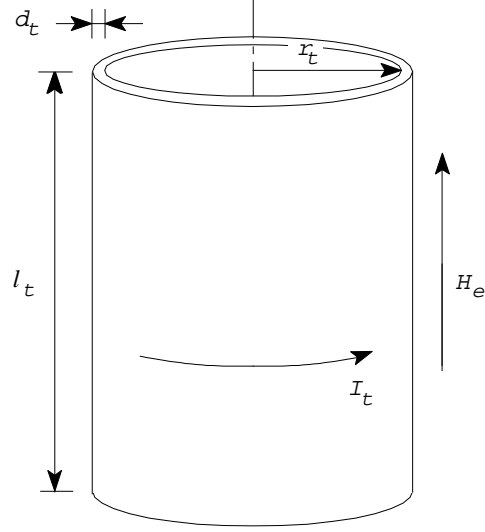


**Figure 4.5.** Parameters for the tube analogon.

tube wall. The relation  $r_t d_t = \delta^2$  also holds for the onset of shielding against a magnetic field perpendicular to the tube axis [Kad59, p. 81].

Returning to our PCB we extend this analogon and estimate the cross-over frequency  $f_c$  between region 1 and 2 by the relation  $2wd = \delta^2$ :

$$f_c = R_{\square}/2\pi\mu_0 w. \quad (4.5)$$

This approximation is valid for the mid position  $x \simeq 0$  of both tracks, as was verified by numerical calculations. A more accurate estimate requires the solution of the implicit equation  $R_{\square} = |Z_t|$  with  $Z_t$  given by Eq. (4.12) in Section 4.3.1.

Above 10 MHz two effects become discernible. First the current density approaches the HF limit under track 1 given by Eq. (4.3). The magnetic field through the GP is strongly reduced. For an infinitely wide GP, the two flux contributions  $\Phi_1$  and  $\Phi_{GP}$  would become equal and opposite. However, because of the finite width some magnetic field lines wrap around the GP (Fig. 4.4c). The flux between track 2 and the GP is then given by the residual difference of the flux contributions which can be described by a frequency independent mutual inductance  $M$  (region 5 and the curve  $c$  in Fig. 4.3a). From Kaden [Kad59, p. 266] or Love [Lov23, Section 13] one has

$$M = \frac{\mu_0}{4\pi} \frac{h_1 h_2}{w^2}, \quad (4.6)$$

valid near  $x = 0$  for both tracks. At the edges of the GP  $K_z(x)$  approaches the HF limit near  $|x| = w$ :

$$K_z(x) \propto 1/\sqrt{w^2 - x^2}, \quad (4.7)$$

analogous to the edge effect for charge density on a plate. The magnetic field near the edges is strong. However, the current density diverges only in thin strips near the edges of the GP. Because of the small area involved, the flux through these strips is small. Only at high

frequencies the resistance will then be overruled by induction, in our example at frequencies larger than 30 MHz; the GP then behaves like an ideal conductor ( $\sigma \rightarrow \infty$ ).

Second, the skin effect alters the vertical current distribution in the GP. For an infinitely wide GP with permeability  $\mu = \mu_r \mu_0$  the high-frequency  $Z_t$  is given by:

$$Z_t = R_{\square} \frac{kd}{\sinh kd} \frac{h_t}{\pi(x^2 + h_t^2)}, \quad (4.8)$$

in which  $h_t = h_1 + h_2$  and  $k = (1+j)/\delta$  with  $\delta = \sqrt{2/\omega\mu_0\mu_r\sigma}$  the skin depth. This behavior is shown by the dot-dash line, region 3 and 4 in Fig. 4.3a, and by the curve *b*. For the 50 mm wide GP of our example, the exponential decrease in  $Z_t$  of Eq. (4.8) by the skin effect is overruled by the increase due to the flux coupling around the GP. Observe that the  $Z_t$  in Eq. (4.8) depends only on the total distance  $h_t$  between the tracks, the same result that is found for the  $Z_t$  between two circular coils separated by a large plate; see e.g. [Bal81] and references added therein. The transfer impedance of a thin-walled tube [Sch34, Kad59], considered as outer conductor of a coaxial system, decreases in an analogous fashion:

$$Z_t = R_0 \frac{kd_t}{\sinh kd_t}, \quad (4.9)$$

where  $R_0$  is approximately the d.c. resistance of the tube per meter, and  $d_t$  the wall thickness of the tube. The current flows in the longitudinal direction through the tube wall; the current distribution is axially symmetric. The additional  $x$ -dependence in Eq. (4.8) stems from the distribution of the current over the GP. A similar exponential decrease also sets in at  $d_t \simeq \delta$  for the shielding of the tube mentioned above [Kad59, pp. 292-295]. Some authors call the current contraction under track 1 the lateral skin effect or just skin effect [Lip80]. In this paper the vertical skin effect is meant when the term vertical is omitted.

Note that the perpendicular component  $H_{\perp}$  of the magnetic field at the surface of the GP never vanishes exactly for a GP with finite conductivity. The  $y$ -component of  $\nabla \times \mathbf{E} = -j\omega\mathbf{B}$  links the  $x$ -variation of the current density  $\sigma E_z$  to the  $H_{\perp}$ . In region 3 (Fig. 4.3a) the magnetic field penetrates the GP and leaves at the other side of the GP; in region 4 the magnetic field  $H_{\perp}$  at the surface is guided through the skin. The penetration is more pronounced where the variation of the current density is larger, i.e. near the edges and under track 1 as discussed before.

### 4.3 Mathematical description

#### 4.3.1 The half space and the infinite plate

In a first step consider the plane  $y = 0$  limiting the lower half space (Fig. 4.6a) of material with conductivity  $\sigma$  and magnetic permeability  $\mu = \mu_0\mu_r$ . The elementary wire carrying the injection current  $I_1$  is in the dielectric region ( $\varepsilon_0, \mu_0$ ) at a height  $h_1$  above the plane. The distribution of the induced return current  $J_z(x, y)$  in the plane has already been calculated by Carson [Car26] in 1926 for non-magnetic materials ( $\mu_r = 1$ ). He assumed a transverse magnetic wave  $\propto e^{j\omega t - \gamma z}$  propagating in the positive  $z$ -direction with a small propagation constant  $|\gamma|$ .

Carson aimed at a telegraph wire several meters above soil with typical conductivity of about  $10^{-2} \Omega^{-1}\text{m}^{-1}$ . Many authors [Ols74, Eft78, Wed78, Oly95] treated the transmission of waves along wires above a dissipative medium; some use the full-wave analysis. For our PCB Carson's approach is apparently correct up to the GHz range because of the much smaller

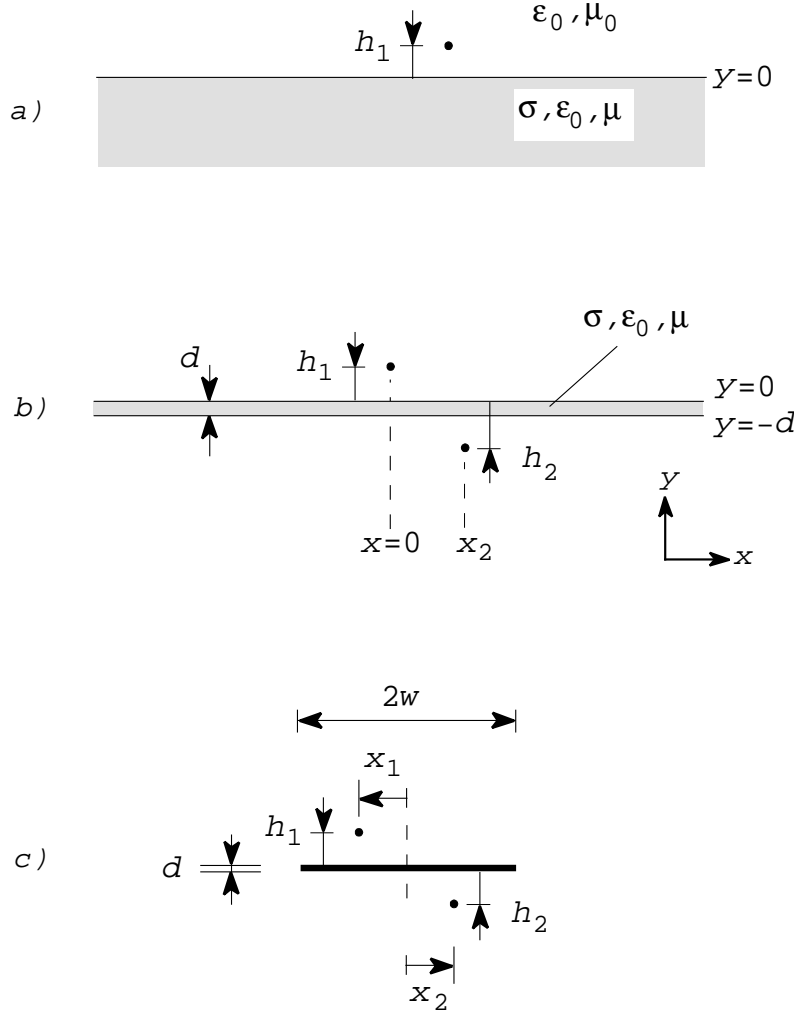


**Figure 4.6.** Parameters for a) the infinite plane, b) the infinite plate, and c) the strip or finite plate.

distances between tracks and GP and the high conductivity of copper. Appendix C.1 gives the general steps of Carson's derivation, which is slightly extended in order to incorporate magnetic materials  $\mu_r \neq 1$ ; see also [Wis31].

In a second step consider the plate at  $y = 0$  with thickness  $d$  and conductivity  $\sigma$ , still of infinite extent in the  $x$ -direction (Fig. 4.6b). The injection wire is at the position  $(0, h_1)$  above the upper side of the plate; a sensing wire is at  $(x_2, -h_2)$  below the plate. In both dielectric regions  $\mu_r = 1$  is assumed. Because of the finite conductivity, the magnetic field penetrates the plate. An inductive coupling exists between the circuits at both sides of the GP. In Appendix C.2, Carson's calculation for the longitudinal current distribution  $J_z(x, y)$  in the plate is extended to allow a finite thickness  $d$  of the plate (Eq. (C.13)) and to include the magnetic field below the plate.

For a thin GP one may take the 'thin plate limit'  $d \downarrow 0$  and  $\sigma \rightarrow \infty$  while keeping the sheet resistance  $R_\square$  of the plate constant. The sheet current density  $K_z$  can be derived from the volume current density  $J_z(x, y)$  in Eq. (C.13):

$$K_z(x) = \int_{-d}^0 J_z(x, y) dy = -\frac{j\omega\mu_0 I_1}{2\pi R_\square} \int_0^\infty \frac{\cos(\alpha x) e^{-\alpha h_1}}{\alpha + j\beta} d\alpha, \quad (4.10)$$



in which  $\beta = \omega\mu_0/2R_\square$ . Asymptotic expressions for  $Z_t$  can also be derived in closed form. After some algebra using Eq. (C.17), the transfer impedance for the sensing wire at  $(x_2, -h_2)$  under the GP simplifies to

$$Z_t = \frac{j\omega\mu_0}{2\pi} \int_0^\infty \frac{\cos(\alpha x_2) e^{-\alpha h_t}}{\alpha + j\beta} d\alpha, \quad (4.11)$$

in which  $h_t = h_1 + h_2$ . For low frequencies the small-argument expansion [Abr70] of the Ei functions in Eq. (C.18) can be used, this yields

$$Z_t = \frac{1}{4}\omega\mu_0 - j\frac{\omega\mu_0}{2\pi} \left[ \ln \frac{\omega\mu_0(x_2^2 + h_t^2)^{\frac{1}{2}}}{2R_\square} + \gamma_e \right], \quad (4.12)$$

with  $\gamma_e = 0.57721 \dots$  being Euler's constant. This  $Z_t$  is the curve labeled *a* in Fig. 4.3a. The high-frequency approximation of Eq. (4.11) reduces to

$$Z_t = R_\square \frac{h_t}{\pi(x_2^2 + h_t^2)}. \quad (4.13)$$

This  $Z_t$  value (region 3 and the curve *b* in Fig. 4.3a) does not explicitly depend on the frequency. In Eq. (4.11) only the sum  $h_t$  of the heights  $h_1$  and  $h_2$  occurs. Reciprocity only requires that the  $Z_t$  is symmetrical in  $h_1$  and  $h_2$ . Remarkably the position of the thin GP between the track does not influence this part of  $Z_t$ .

In the thin-plate limit no skin effect is possible since  $d/\delta$  goes to zero. To correctly describe the skin effect we must consider a general thickness  $d$  and use the full equation (C.17). The resulting  $Z_t$  is displayed as curve 0-2-3-4 in Fig. 4.3a. Fortunately the expression simplifies in the high-frequency limit to Eq. (4.8). The frequency  $f_{cs}$  where the skin effect becomes effective, can be calculated explicitly. Choose, by convention, the 3 dB point where  $|Z_t|^2$  obtained by Eq. (4.8) is halved with regard to the value of region 3 in Fig. 4.2 given by Eq. (4.13). The transcendental equation

$$\left| \sinh \left[ (1+j) \frac{d}{\delta} \right] \right| = 2 \frac{d}{\delta}, \quad (4.14)$$

has an numerically obtained solution  $d/\delta \simeq 2.14$ . Thus the cut-off frequency  $f_{cs}$  is given by

$$f_{cs} \simeq \frac{2.25}{\pi\mu_0\sigma d^2}, \quad (4.15)$$

and is again independent of the heights  $h_1$  and  $h_2$ . This frequency equals approx. 22 MHz for our GP parameters given at the end of Section 4.1 used in calculating  $Z_t$  in Fig. 4.3a. In Fig. 4.3a the curve 0-2-3-4 shows the behavior of  $Z_t$  as described in this Section. Good agreement is shown in region 2 and 3 (Fig. 4.3a) between the analytical expressions and the method of moments (MOM) calculations described in the next subsection. The deviations at the low and the high-frequency end (region 1 and 5 in Fig. 4.3a) are due to the finite width of the GP.

### 4.3.2 The strip of finite width

We now replace the infinite plate GP by a strip of width  $2w$  (Fig. 4.6c). The injection current  $I_1$  flows through the wire at the upper side of the strip and returns via the strip. We

again consider the thin plate limit and calculate the sheet current density  $K_z(x)$ . The width  $2w$  is slightly less than the shortest wavelength under consideration. We use Faraday's law for two positions  $(x, 0)$  and  $(x^*, 0)$  on the strip:

$$E_z(x, 0) - E_z(x^*, 0) = -j\omega \{A_z(x, 0) - A_z(x^*, 0)\} \quad (4.16)$$

in which the vector potential  $A_z$  is due to the current  $I_1$  through the injection wire and to the current  $K_z = E_z/R_\square$  distributed over the strip, see Appendix D. Here we require that  $I_1$  returns through the strip, or

$$\int_{-w}^w K_z(x) dx = -I_1. \quad (4.17)$$

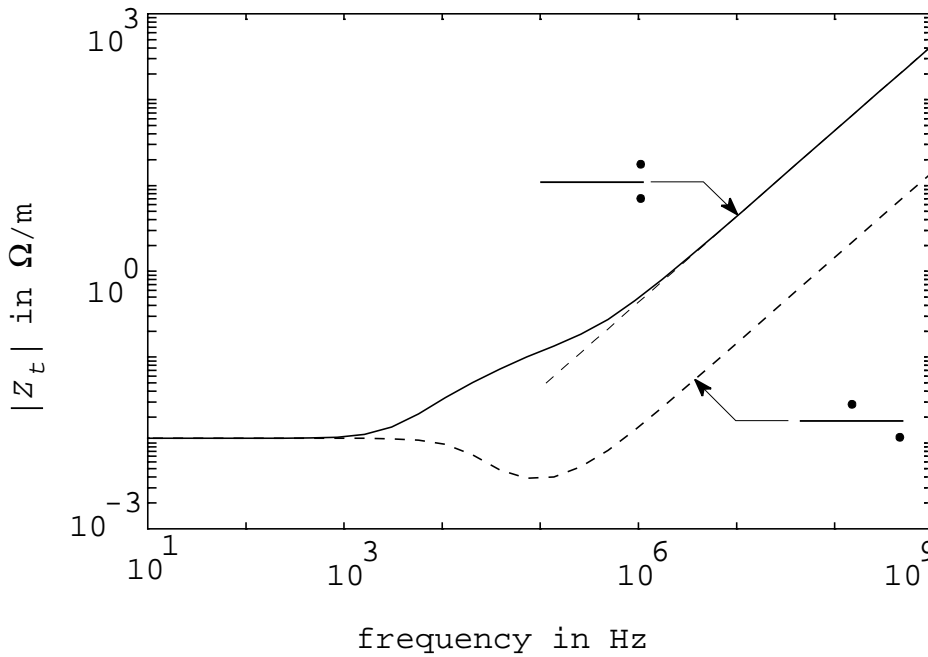


**Figure 4.7.** DM to DM  $Z_t$  calculated by MOM for one or both wires at the edge of a 50 mm wide GP. The vertical distance between wires and GP is 1.5 mm. The straight line behavior above 10 MHz corresponds to  $M$ -values of Fig. 4.8.

Equation (4.16) was solved by the method of moments [Har93]; for other methods see Atkinson [Atk97]. Pulse functions as basis functions approximated  $K_z(x)$  over intervals of the strip. Point matching (Dirac delta functions as testing functions) was used. The collocation points were at the middle of subsequent intervals. The vector-potential contribution due to each interval was calculated analytically [Jas77]. To improve the accuracy with reduced calculation effort, the discretization of the strip was non-uniform: a  $(x^2 + h_1^2)^{-1}$  partition beneath the injection wire and a fine constant mesh at the edges. The transfer impedance  $Z_t$  is then obtained by Eq. (4.1). The solid line in Fig. 4.3a is obtained by this MOM method. The total number  $N$  of intervals was chosen such that the difference between the analytical HF value of  $Z_t$  (see next section) and the numerical one was less than 10 percent. This required an accuracy in  $A_z$  of about  $10^{-4}$ ; see also Fig. 4.3b. Such accuracy is generally needed in EMC calculations because one looks for spurious couplings close to the currents. No attempts were made to obtain the ‘ideal mesh’ through rigorous error analysis.

For low frequencies the resistive contribution ( $E_z$  term in Eq. (4.1)) dominates the magnetic-flux term, and  $Z_t$  is constant. The cross-over frequency  $f_c$  between region 1 and 2 was discussed in Section 4.2; the approximate expression based on the tube analogon is given in Eq. (4.5). The flat region 3 agrees with the analytical expression Eq. (4.13) for  $Z_t$  presented before. At high frequencies the vector potential dominates the resistive term; the l.h.s. of Eq. (4.16) can be neglected. As a result of the finite width, the transfer impedance in Fig. 4.3 increases linearly with frequency for  $f > 30$  MHz.

When both tracks are close to the edge, the current density concentrates more slowly under track 1; the calculated  $Z_t$  is shown in Fig. 4.7. At high frequency the MOM  $Z_t$  is in agreement with the analytical expression Eq. (4.20) discussed below.

### 4.3.3 Mutual inductance

For high frequencies the GP can be considered as a thin ( $d \downarrow 0$ ) ideal conductor ( $\sigma \rightarrow \infty$ ) with a sheet current distribution  $K_z$ . The magnetic field does not penetrate the GP anymore. The magnetic field outside the GP can then be derived from a complex potential  $\Omega$  which can be obtained by means of conformal transformation. See for details Appendix A.3. The current distribution on both surfaces of the strip results from [Kad59, pp. 56-58]

$$K_z(x) = -|\hat{\mathbf{y}} \times \mathbf{H}| = -\text{Re} \frac{d\Omega^*}{dz}, \quad (4.18)$$

where  $\Omega^*$  is the conjugate of the complex potential  $\Omega$ . For an arbitrary position of the injection wire, the result of Eq. (4.18) is given by Love [Lov23]. For small height-to-width-ratio  $h_1/w$  and the injection wire near  $x = 0$ , his solution [Lov23, Section 13] can be approximated by

$$K_z(x) \simeq -\frac{I_1}{\pi} \left[ \frac{h_1}{x^2 + h_1^2} + \frac{h_1}{w\sqrt{w^2 - x^2}} \right], \quad (4.19)$$

in which the contribution of  $\Omega$  at the upper and the lower surface are added (see Fig. A.5). The first term in the right-hand side is the same as the HF distribution for an infinitely thin plate; compare with Eq. (4.3). The last term results from the edge effect.

The transfer impedance now becomes a frequency-independent mutual inductance  $M$  which can be calculated by means of Eqs. (A.15), (A.17), (A.18), and (A.19) for any position of the two wires. When  $h_{1,2} \ll w$  simple real-valued closed-form approximations exist. The lowest  $M$  is given by Eq. (4.6) for both wires at  $x = 0$  on opposite sides of the GP. An upper bound occurs when both wires are at the same edge,  $|x| = w$ , but still on opposite sides of the GP. For general  $h_1$  and  $h_2$ :

$$M(|x| = w) \simeq \frac{\mu_0}{4\pi} \ln \left[ 1 + \frac{2\sqrt{h_1 h_2}}{(h_1 + h_2)} \right], \quad (4.20)$$

which attains a maximum value when  $h_1 = h_2$ :  $M_2 = (\mu_0/4\pi) \ln 2$ . Figure 4.8 shows a set of  $M$ -curves for a GP of  $2w = 5\text{cm}$  and both wires at the same distance  $h_{1,2} = 1.5\text{ mm}$  w.r.t. to the GP, calculated from the full complex potential  $\Omega$  of Eq. (A.18). For comparison we included an  $M$ -curve for both wires on the same side of the GP, one of them placed at  $x = 0$ .

## 4.4 Influence of a nearby metallic plate on the DM-to-DM crosstalk

Many PCB's are mounted in a cabinet, above a metal panel. A CM loop is then formed by the GP and the cabinet panel (CP in Fig. 3.4) of width  $2p$ . We describe the coupling

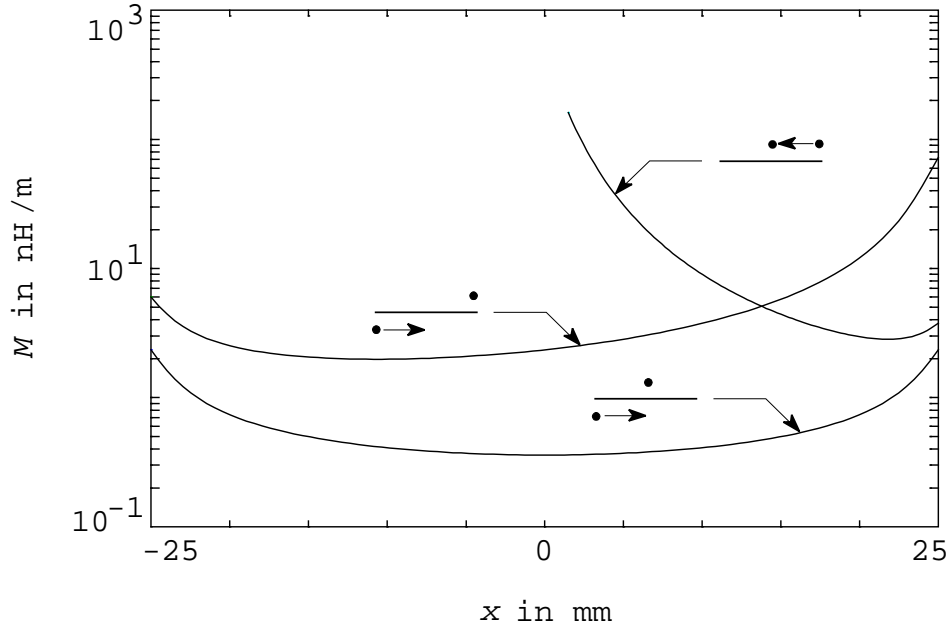


**Figure 4.8.** The mutual inductance part  $M$  of  $Z_t$  between two DM circuits when one of the circuits moves over the GP along the  $x$ -direction. Both tracks are at 1.5 mm distance from the 50 mm wide GP.

between a DM loop on the PCB and the CM loop by a transfer impedance  $Z_t$ ; the impedance of the CM loop is denoted by  $Z_{CM}$ . Both impedances were calculated by MOM. A detailed account was given in the previous chapter. Here we restrict the attention to the DM-to-DM crosstalk, and we omit all cables.

We first assume that the cabinet panel (CP) is not connected to the GP; the CM loop is an open circuit. When the cabinet panel now approaches the ground plane, the magnetic field due to the DM circuit induces a circulating current in the CP even without a net current flow in the CP. The DM-to-DM crosstalk depends on the position of the CP. For a disconnected CP, Fig. 4.9a shows the  $Z_t(1-2)$  at several  $h_{CP}$ , with both tracks at mid GP ( $x_1 = x_2 = 0$ ). We again assumed  $h_1 = h_2 = 1.5$  mm and  $2w = 5$  cm.

Of course the  $Z_t$  at d.c. does not depend on the presence of the disconnected CP. At mid frequencies, region 3 of Fig. 4.3a, the  $Z_t$  is only reduced when track 2 is very close to the CP. The  $Z_t$  assumes the behavior of an isolated PCB already for distances  $h_{CP}$  of 1 cm. At high frequencies the field lines wrapping around the GP dominate the  $Z_t$ . For smaller distances  $h_{CP}$  the H-field under the GP is compressed, which leads to higher  $M$ -values. The homogeneity of the field improves, and the  $M$ -values for  $x_2 = 0$  and  $|x_2| = w$  (lowest two curves in Fig. 4.9b) converge. At  $h_{CP} = 1.5$  mm these  $M$ 's are equal since both DM circuits then capture all magnetic flux under the GP. The field lines at the edges (see e.g. Fig. 3.6) show less curvature for smaller  $h_{CP}$ , as is demonstrated by the lower  $M$  for the sensing track above the GP.

We now connect the GP to the CP over their full width at both ends for instance by the brass plates  $A$  and  $B$  in Fig. 4.1. A current  $I_1$  through track 1 generates a  $I_{CM}$  in the closed CM circuit by the transfer impedance  $Z_t(1\text{-CM})$ , given by

$$I_1 Z_t(1\text{-CM}) + I_{CM} Z_{CM} = 0, \quad \text{with} \quad Z_{CM} = R_{CM} + j\omega L_{CM}. \quad (4.21)$$

The self inductance of the CM loop  $L_{CM}$ , as well as the distribution of  $I_{CM}$  over the GP

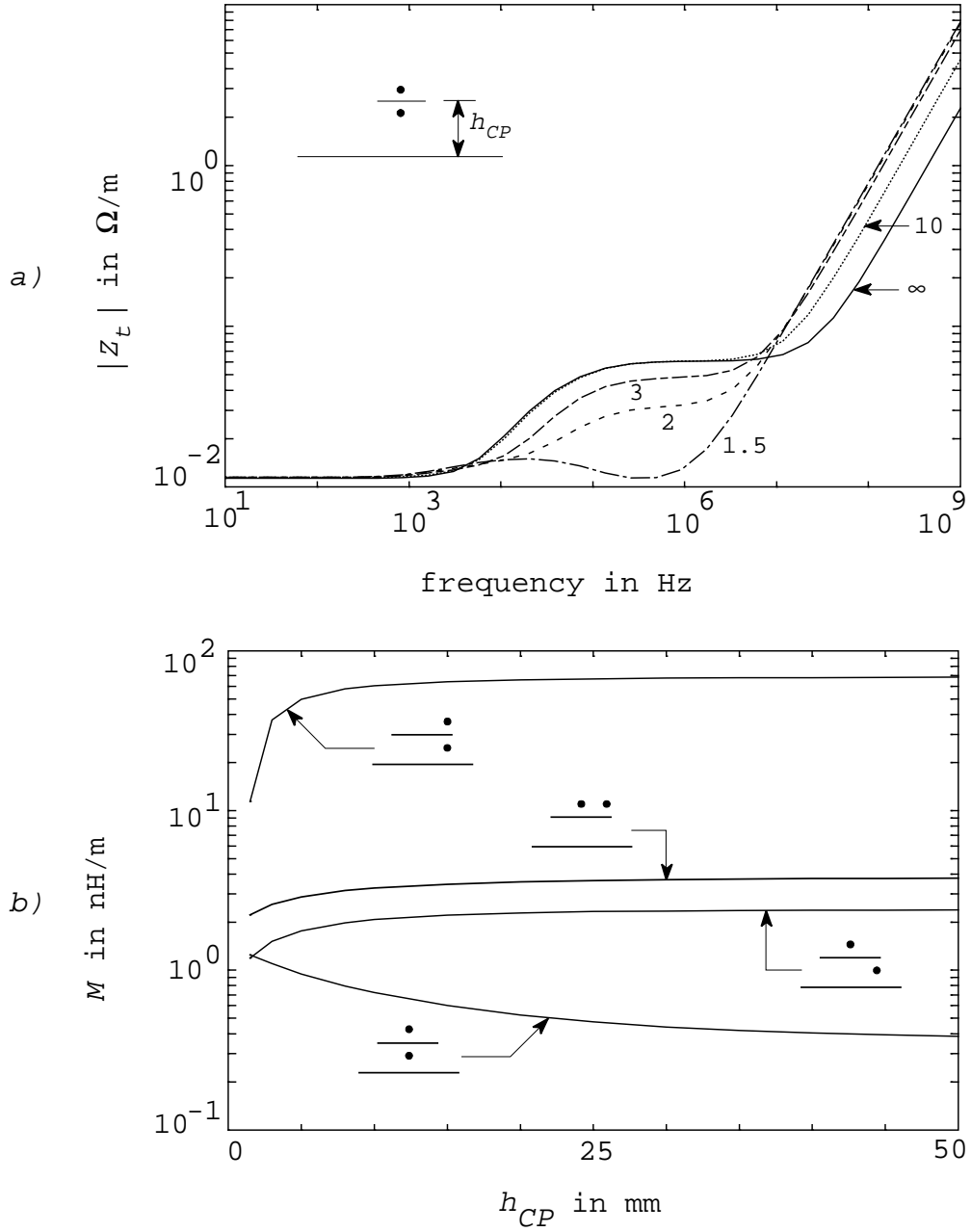


**Figure 4.9.** a) DM to DM  $Z_t$  for several distances  $h_{CP}$  (in mm) between GP ( $2w = 50$  mm) and CP ( $2p = 20$  cm). b)  $M$ -part of  $Z_t$  for DM to DM, as function of  $h_{CP}$  for several positions of the injection and sensing tracks.

and CP can be calculated by the MOM, which agreed with the analytical approximations of Kuester and Chang [Kue80]. The  $R_{CM}$  is the series resistance of GP and CP. The final transfer impedance between the tracks 1 and 2 is denoted by  $Z_t(1-2,c)$  where c indicates the closed CM loop:

$$Z_t(1-2,c) = Z_t(1-2,o) - \frac{Z_t(1-CM)Z_t(2-CM)}{Z_{CM}} \quad (4.22)$$

with  $Z_t(1-2,o)$  the transfer impedance in case of an open CM loop. Figure 4.10 shows  $Z_t(1-2,c)$ , assuming a CP of 1.5 mm brass in which the skin effect is neglected,  $h_{CP} = 1$  cm,  $h_1 = h_2 = 1.5$  mm and  $2w = 5$  cm.

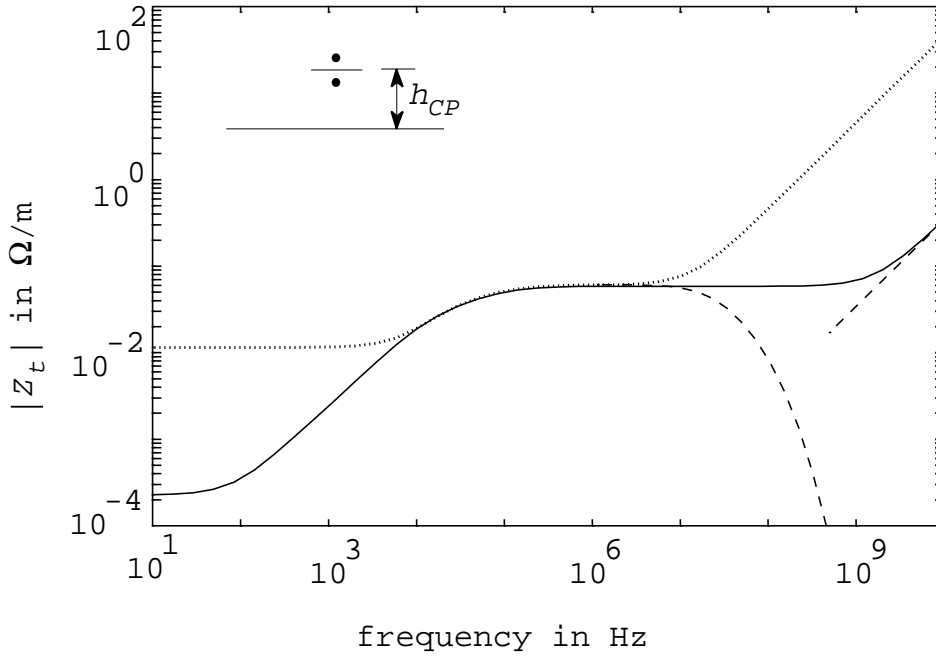


**Figure 4.10.** The MOM results of the DM to DM  $Z_t$  (—) when the CP ( $2p = 20$  cm) is connected to the GP ( $2w = 50$  mm) at both ends;  $h_{CP} = 1$  cm. Also indicated are the  $Z_t$  for a disconnected CP ( $\cdots$ ), as well as the expected behavior due to the skin effect and due to the residual  $M$ -coupling ( $- -$ ).

Major changes occur at low frequencies; the small resistance  $R_{CP}$  of the CP is parallel to  $R_{GP}$  of the GP, and  $Z_t = R_{GP}R_{CP}/(R_{GP} + R_{CP})$ . However, already at 100 Hz the  $Z_t$  rises. In order to estimate the cross-over frequency from Eq. (4.22), one may replace  $Z_{CM}$  by  $R_{CM} + j\omega L_{CM}$  and substitute both  $Z_t(1-CM)$  and  $Z_t(2-CM)$  by  $R_{GP}$ . In first approximation  $Z_t(1-2,o)$  also equals  $R_{GP}$ . The resulting cross-over frequency becomes  $L_{CM}/2\pi R_{CP}$ , which for our setup is 230 Hz. It turned out that the small inductive component in  $Z_t(1-2,o)$  was mainly responsible for the lowering of the cross-over to about 100 Hz, as shown in Fig. 4.10. The flat region 3 is extended to higher frequencies. The short-circuited CM loop reduces the flux and decreases the  $M$ -coupling. The dotted lines indicate the residual  $M$ -coupling, as well as the expected decrease due to the skin effect in the GP.

## 4.5 A DM track between two planes

In multilayer PCB's the coupling of a signal track is reduced when the track is placed between two planes, ground and/or power; assume the planes at  $y = \pm h_{PP}$  (Fig. 4.11).

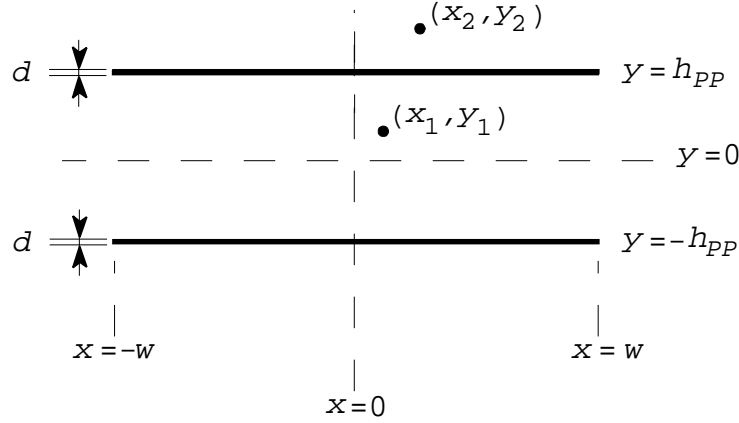


**Figure 4.11.** Parameters for a wire 1 between two planes of width  $2w$ . The sensing wire 2 resides outside the two planes.

We first describe the  $Z_t$  between a track on top of a very wide PCB and a track midway between both planes at  $(x_1, y_1) = (0, 0)$  carrying a current  $I_1$ . Assuming very wide GP's and filamentary wires for the tracks, the current distribution  $K_z$  in both planes can be calculated as in Section 4.3, see Appendix C.3. The 'thin-plate' result is:

$$K_z(x) = -\frac{j\omega\mu_0 I_1}{2\pi R_\square} \int_0^\infty \frac{\cos(\alpha x) e^{-\alpha h_{PP}}}{\alpha + j\beta(1 + e^{-2\alpha h_{PP}})} d\alpha, \quad (4.23)$$

where again  $\beta = \omega\mu_0/2R_\square$ . The high-frequency approximation of  $K_z$  becomes

$$K_z(x) = -\frac{I_1}{4h} \operatorname{sech} \frac{\pi x}{2h_{PP}}, \quad (4.24)$$

which is a factor  $\pi/4$  smaller than the current density at  $x = 0$  with only one GP; compare Eq. (4.3). The current density is also more concentrated near wire 1. For the 'thin-plate'  $Z_t$  of a wire at  $(x_2, h_2)$  with  $h_2 \geq h_{PP}$  we find

$$Z_t = \frac{j\omega\mu_0}{2\pi} \int_0^\infty \frac{\cos(\alpha x_2) e^{-\alpha h_2}}{\alpha + j\beta(1 + e^{-2\alpha h_{PP}})} d\alpha, \quad (4.25)$$

which describes regions 0, 2, and 3 in Fig. 4.12. We include the skin effect (region 3 and 4 in Fig. 4.12) to obtain the high-frequency  $Z_t$ :

$$Z_t = \frac{R_\square}{\pi} \frac{kd}{\sinh kd} \int_0^\infty \frac{\cos(\alpha x_2) e^{\alpha(d-h_2)}}{1 + e^{-2\alpha h_{PP}}} d\alpha. \quad (4.26)$$

The integral can be expressed in elementary  $\Psi$ -functions [Gra67, 3.541.6]. For  $(x_2, y_2) = (0, 2h_{PP})$  and  $d \downarrow 0$  the integral is simply  $(\ln 2)/2h_{PP}$ . In the flat region 3  $Z_t$  is a factor  $\ln 2$  smaller than the  $Z_t$  with one GP, Eq. (4.8), at the equivalent position. However, because a part of the current returns at the other side of wire 1, the reduction in  $Z_t$  is less than  $1/2$  as could be expected intuitively.

When the injection wire is midway between the planes, the return current is shared equally by both planes. For other  $y$ -position of the wire, the total current varies linearly as  $-(h_{PP} + y)I_1/2h_{PP}$  for the top and as  $-(h_{PP} - y)I_1/2h_{PP}$  for the bottom plane at high frequencies.

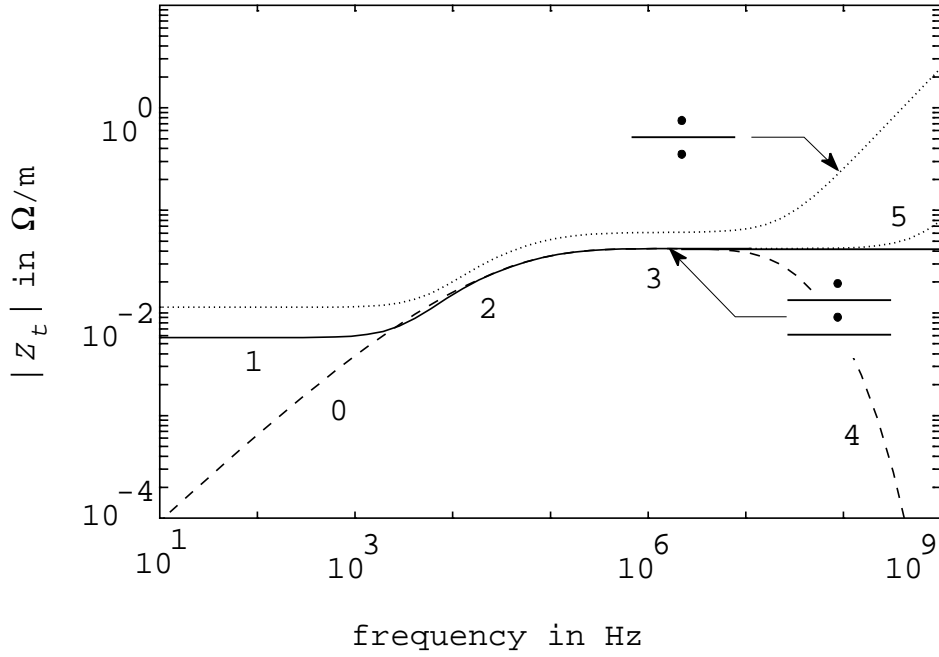


**Figure 4.12.** General behavior of  $|Z_t|$  between track 1 and 2 with  $2w = 5$  cm wide planes. Track 1 is positioned at the origin, while track 2 resides at  $(0, 2h_{PP})$ , width  $h_{PP} = 1.5$  mm. The solid curve 1-2-3-5 has been calculated by means of MOM; the dotted deviation in region 5 is due to numerical inaccuracies, which is corrected by the straight line. The curve 0-2-3-4 (- - -) shows  $|Z_t|$  for very wide planes; the skin effect again lowers the impedance in region 4. For comparison we have included the behavior for a PCB with only one GP.

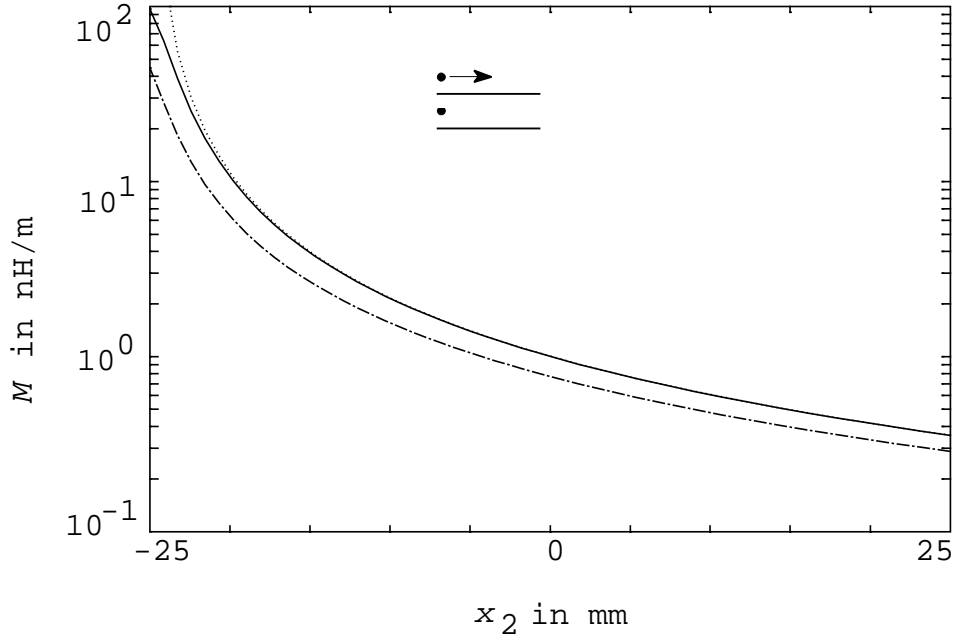


**Figure 4.13.** The mutual inductance part  $M$  of  $Z_t$  between two DM circuits. The injection wire resides between the two finite planes, near the edge. The sensing wire at the upper plane moves over the full width. The full expression Eq. (A.24) (—) as well as the approximations Eqs. (4.27) ( $\cdots$ ) and (A.25) ( $-\cdot-\cdot-$ ) are shown



The  $M$ -part in  $Z_t$  is strongly reduced since both planes effectively confine the magnetic field. An approximate procedure has been followed assuming that wire 1 and 2 are at some distance  $|\delta x_1|$  and  $|\delta x_2|$  from the edge of the PCB; see Appendix A.6. For  $M$  one finds:

$$M = \frac{\mu_0 \delta h_2}{2\pi} \left( \frac{h_{PP}}{\pi |\delta x_2|^3} \right)^{\frac{1}{2}} e^{-\frac{\pi |\delta x_1|}{2h_{PP}} - \frac{1}{2}}, \quad (4.27)$$

where  $\delta h_2$  is the vertical distance of wire 2 above the top plane. Since  $\delta x_1$  in the argument of the exponential decreases  $M$  rapidly, only one edge is taken into account. In Fig. 4.13 we compare Eq. (4.27) with the complex potential result of Eq. (A.25). When wire 1 is deeply buried between both planes at large  $\delta x_1$ , very low  $M$ -values result by Eq. (4.27) and other effects may become dominant. Assume for instance that the planes provide of ground and d.c. power; insufficient decoupling between the planes at the ends may cause a different return current  $-(\frac{1}{2} \pm a)I_1$  through the top (+) and bottom (−) plane. The value of  $a$  has to be estimated for an actual PCB; here we just assume any value  $0 \leq |a| \leq \frac{1}{2}$ . In worst case, no net return current flows through one of the planes.

## 4.6 High-frequency effects of the crosstalk

The previous sections focused on 2D effect for which it is convenient to use a  $Z_t$  per unit length. When resonances show up, the total transfer impedance  $Z_T = V_{DM}/I_1$  (with capital  $T$  as subscript) is more useful. Therefore, from now on  $Z_T$  will be considered. The current  $I_1$  is now the injected current into track 1 near plate  $A$  (Fig. 4.1). As before, the voltage  $V_{DM}$  is measured at this sending end. The filamentary wires in the calculations are replaced by the actual tracks of width  $b$ , as mentioned in the introduction.

### 4.6.1 Transmission-line description

The dominant mode in a microstrip line is quasi-TEM: a TEM wave adapted to include a nonhomogeneous dielectric by modifying the line capacitance, and the conductor losses by adding a series resistance. Gupta *et al.* [Gup96] give an overview of the vast literature published over the last decades.

Figure 4.14 shows our four tracks as coupled microstrip lines TL1-TL4 with the ground plane (GP) as reference;  $z = 0$  corresponds with the side of plate  $A$  (near end) and  $z = \ell$  with the side of plate  $B$  (far end). The TL5 describes the common-mode (CM) current through the GP; its return is a nearby metallic plate or free space. It turned out that a second-order coupling (DM-CM-DM) becomes important for small values of  $Z_T$  between tracks [Ber96]; we then had to include TL5. Details are presented in Section 4.6.4. Until there, the DM-CM-DM coupling and hence TL5 can be neglected.

The voltage source  $V_g$  with impedance  $Z_g$  injects a current  $I_1$  in circuit 1. The other impedances depend on the actual situation studied, for instance,  $Z_{Bi} = 0$ ,  $i = 1, \dots, 4$  for the shorted situation at brass plate  $B$  (Fig. 4.1); other values will be discussed in Sections 4.6.3 and 4.6.4. The response of the system can be calculated from the impedance matrix  $\mathbf{Z}(\omega)$  and admittance matrix  $\mathbf{Y}(\omega)$  per unit length. Djordjević *et al.* [Djo87a] presented an overview of the methods to solve the equations for the coupled lines with linear and non-linear load impedances, both in the frequency and the time domain. We will consider linear loads in the frequency domain; this allows us to employ the modal expansion of Djordjević and Sarkar [Djo87b], which is similar to the BLT-method [Bau78, Tes97].

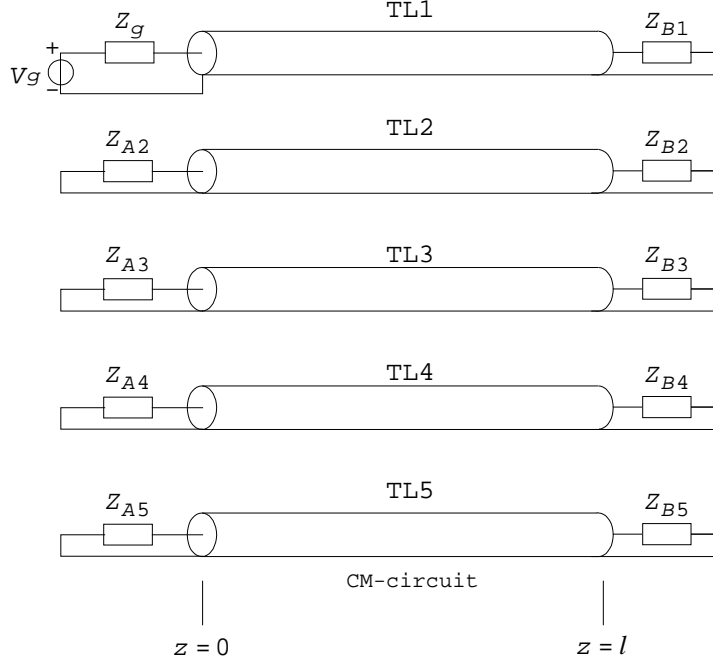


**Figure 4.14.** Transmission-line (TL1-TL4) model of the four-track PCB in Fig. 4.1; TL5 incorporates the DM-CM couplings as discussed in the text. The near side  $z = 0$  corresponds with the side of brass plate A, the far end  $z = \ell$  with brass plate B. The terminating impedances are discussed in the text.

#### 4.6.2 TL parameters

Let us first consider a single track of width  $b$  at a height  $h$  on a dielectric above a GP of infinite extent.

##### Characteristic impedance

The characteristic impedance  $Z_m = \sqrt{L_s/C_s}$  of this microstrip line is given e.g. by Gupta *et al.* [Gup96];  $L_s$  and  $C_s$  are the self inductance and self capacitance of the track with respect to the GP. For convenience we repeat here Gupta's expressions (Eq. (2.116))

$$Z_m = \begin{cases} \frac{\eta}{2\pi\sqrt{\varepsilon_{r,eff}}} \ln\left(\frac{8h}{b} + 0.25\frac{b}{h}\right) & , \quad \frac{b}{h} \leq 1, \\ \frac{\eta}{\sqrt{\varepsilon_{r,eff}}} \left\{ \frac{b}{h} + 1.393 + 0.667 \ln\left(\frac{b}{h} + 1.444\right) \right\}^{-1} & , \quad \frac{b}{h} > 1, \end{cases} \quad (4.28)$$

and

$$\varepsilon_{r,eff} = \frac{\varepsilon_r + 1}{2} + \frac{\varepsilon_r - 1}{2} \begin{cases} (1 + 12h/b)^{-1/2} + 0.04(1 - b/h)^2 & , \quad \frac{b}{h} \leq 1, \\ (1 + 12h/b)^{-1/2} & , \quad \frac{b}{h} > 1, \end{cases} \quad (4.29)$$

where  $\eta = \sqrt{\mu_0/\varepsilon_0} \simeq 120\pi \, \Omega$ . The characteristic impedance  $Z_m$  and the effective dielectric constant  $\varepsilon_{r,eff}$  depend on  $\varepsilon_r$  and  $b/h$ . The finite size of GP and dielectric increases  $Z_m$ ; the deviation is less than 3 percent when the track is farther than  $2b$  from the edge, as was shown by Smith and Chang [Smi85].

The self inductance  $L_s$  can be obtained from  $L_s = Z_{0m}/c_0$ , with  $Z_{0m}$  the characteristic impedance of the microstrip with the dielectric replaced by vacuum or  $\varepsilon_{r,eff} = 1$ , and  $c_0$  the velocity of light in vacuo. For all tracks on our PCB's we use the same  $L_s = 414$  nH/m, calculated as if the GP were of infinite extent. The capacitance  $C_s = 88.9$  pF/m may be calculated from  $L_s$  and  $Z_m$  with the proper value of  $\varepsilon_{r,eff} = 3.34$  for the dielectric.

### Series impedance

The series impedance  $Z_s$  for the track is

$$Z_s(\omega) = R_{DC} + R_s(\omega) + j\omega L_s, \quad (4.30)$$

where  $R_{DC}$  and  $R_s(\omega)$  are the d.c. and skin-effect resistances. Closed-form expressions for the skin-effect resistance were first published by Pucel *et al.* [Puc68] in 1968, where they used Wheeler's incremental inductance rule. Recently Collin proposed expressions by means of conformal mapping [Col92, Appendix III]. These values are somewhat higher than Pucel's one; Collin claims that his solution is in better agreement with experimental results [Col92, pp. 156-157]. For a microstrip structure with finite width GP (as in our case), Djordjević [Djo94] gives other expressions for  $R_s(\omega)$ . The high-frequency current distribution in a microstrip line and a rectangular strip is discussed in several papers by Faraji-Dana and Chow [Far90a, Far90b, Far91]. Later on the choice for the skin-effect resistance will be discussed.

### Coupled tracks, off-diagonal elements

We now include the remaining tracks. The impedance matrix  $\mathbf{Z}(\omega)$  per unit length for our problem (Fig. 4.1) is then given by

$$\mathbf{Z}(\omega) = Z_s(\omega)\mathbf{I}_4 + \mathbf{Z}_t(\omega), \quad (4.31)$$

in which  $\mathbf{I}_4$  is a  $4 \times 4$  identity matrix and  $\mathbf{Z}_t(\omega)$  the transfer impedance matrix with zeros on the diagonal as described in Sections 4.2 and 4.3.

The admittance matrix  $\mathbf{Y}(\omega)$  per unit length equals

$$\mathbf{Y}(\omega) = j\omega\mathbf{C}, \quad (4.32)$$

where  $\mathbf{C}$  is the  $4 \times 4$  capacitance matrix (see e.g. Van Bladel [Bla85, Section 4.6]). It is more difficult to calculate the off-diagonal elements of the capacitance matrix because the boundary conditions on the dielectric need to be accounted for. We followed a similar numerical approach by Harrington [Har69] and Venkataraman [Ven85] for static electric fields. For highest accuracy the discretization was adapted, see Appendix B. In an iterative procedure we calculated the absolute error in the tangential electric field, integrated over each conductor element; for the dielectric boundaries we took the integrated absolute error in the condition for the normal component of the electric field. The element sizes were adjusted until an equipartition of the errors over the elements occurred. From these calculations we derived analytical approximations which suffice in our TL model and considerably speed up the computations for a PCB.

For convenience, suppose that only tracks 1 and 2 (Fig. 4.1) are present. The capacitance matrix then becomes

$$\mathbf{C} = \begin{bmatrix} C_s + C_{12} & -C_{12} \\ -C_{12} & C_s + C_{12} \end{bmatrix}. \quad (4.33)$$

In vacuo the capacitance matrix  $\mathbf{C}_0$  satisfies the relation

$$\mathbf{L}\mathbf{C}_0 = \frac{1}{c_0^2}\mathbf{I}_2 \quad (4.34)$$

with

$$\mathbf{L} = \begin{bmatrix} L_s & M \\ M & L_s \end{bmatrix}, \quad (4.35)$$

the inductance matrix. We found the following approximate relation between  $C_{12}$  and  $C_{12,0}$ , the capacitive coupling coefficients with and without dielectric:

$$C_{12} \simeq \frac{C_{12,0}}{\sqrt{\varepsilon_{r,eff}}}, \quad (4.36)$$

valid for  $h_1 = h_2 = h$  and  $b_1 = b_2 = b$ . This simple relation agrees with the accurate numerical values to within 20 percent for tracks on the same or on different sides of the GP over a wide range of parameters:  $1 \leq \varepsilon_r \leq 12$ ,  $0.8 \leq b/h \leq 4$ , and  $50 \text{ mm} \leq 2w \leq 400 \text{ mm}$ . The numerical diagonal elements of  $\mathbf{C}$  were in good agreement those given by Gupta's expressions (4.28) and (4.29).

#### 4.6.3 Short-circuit case

All tracks are shorted against brass plate  $B$  (Fig. 4.1). Figure 4.15 shows the modules of the measured and calculated transfer impedances between circuit 1 and 2  $Z_T(1-2)$  and 1 and 3  $Z_T(1-3)$ .

In the experiment the injected current  $I_1$  and induced voltages  $V_{DMj}$  ( $j = 2, 3, 4$ ), are all measured with an S-parameter setup [Hor96a, Section VII]. The sensing circuit  $j$  is loaded by  $50 \Omega$  during the  $S_{j1}$  measurements. When these S-parameters are transformed into Z-parameters, the current  $I_j$  must be zero. Therefore, in our model (still without TL5) the near-end impedances  $Z_{Aj}$  ( $j = 2, 3, 4$ ) are all infinite; in the actual calculations  $1 \text{ M}\Omega$  impedances were used. The far-end impedances  $Z_{Bi}$  ( $i = 1, \dots, 4$ ) are chosen equal to zero.

Calculations and measurements agree very well. The peaks in  $|Z_T|$  correspond to quarter wavelength resonances:  $\ell = (2n + 1)\lambda/4$  with  $n = 0, 1, 2, \dots$ . Here  $\lambda$  is the wavelength calculated with Eq. (4.29) and  $\varepsilon_{r,eff} = 3.34$ .

For our experimental boards we had to increase *ad hoc* the skin-effect resistance  $R_s(\omega)$  for all frequencies by a factor five compared to Collin's value in order to fit the resonance amplitudes and widths. A detailed analysis [Hor97a, Section IIe] showed that this increase may be most probably attributed to the manufacturing process and surface roughness.

#### 4.6.4 Characteristic-termination case

When all tracks at the far end are terminated into their characteristic impedance of  $68 \Omega$ , the  $|Z_T|$  will be strongly reduced above 100 MHz because the resonances are suppressed. As already mentioned in Section 4.6.1, the DM-CM coupling modeled by TL5 must now be incorporated.

For a free-standing PCB with no nearby conductor in parallel, the CM current returns as a displacement current; the CM circuit is then difficult to describe in a 2D picture. We assumed an inductive mutual coupling  $M_s$  given by Eq. (3.1) between the DM circuits 1,  $\dots$ , 4 to the CM circuit. For the return of the common-mode current we chose a large cylinder of radius  $R = 1 \text{ m}$ . The mutual capacitance  $C_{s\infty} \simeq 0.2 \text{ pF/m}$  from the DM tracks to this

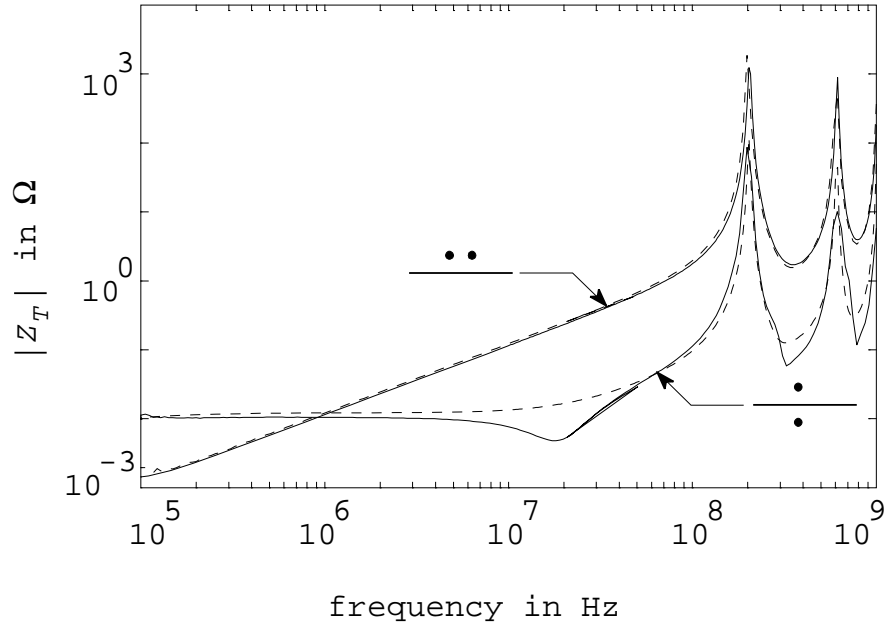


**Figure 4.15.** Measured (—) and calculated (---) transfer impedances  $|Z_T(1-2)|$  and  $|Z_T(1-3)|$  for a  $2w = 5$  cm wide GP; the tracks are shorted against brass plate  $B$ . Tracks 1 and 2 are on opposite sides at 5 mm from the middle line of the GP ( $2w = 5$  cm); the  $x$ -distance between track 1 and 3 is  $s = 10$  mm. The measured reduction of  $|Z_T(1-2)|$  at 20 MHz is due to the skin effect in the GP.

cylinder was numerically calculated by means of the method given in Appendix B. The self-inductance  $L_{CM}$  and self-capacitance  $C_{CM}$  of the CM circuit follow from expressions for a strip  $2w$  in a cylinder of radius  $R$  [Web65, Eq. (26.47)]

$$Z_{CM} = \sqrt{\frac{L_{CM}}{C_{CM}}} = \frac{\eta}{2\pi} \ln \frac{2R}{w}, \quad (4.37)$$

with  $\eta = 120\pi \Omega$ ; for our 5 cm wide PCB this impedance becomes approx.  $260 \Omega$ . Further, we assumed *ad hoc* the near-end impedance  $Z_{A5} = 0 \Omega$  and the far-end impedance  $Z_{B5} = 377 \Omega$ , the free-space wave impedance.

The  $5 \times 5$   $\mathbf{L}^*$  and  $\mathbf{C}^*$  matrices become

$$\mathbf{L}^* = \begin{bmatrix} & & & & M_s \\ & \mathbf{L} & & & M_s \\ & & & & M_s \\ & & & & M_s \\ M_s & M_s & M_s & M_s & L_{CM} \end{bmatrix}, \quad (4.38)$$

and

$$\mathbf{C}^* = \begin{bmatrix} & & & & -C_{s\infty} \\ & \mathbf{C} & & & -C_{s\infty} \\ & & & & -C_{s\infty} \\ & & & & -C_{s\infty} \\ -C_{s\infty} & -C_{s\infty} & -C_{s\infty} & -C_{s\infty} & C_{CM} \end{bmatrix}, \quad (4.39)$$

with  $\mathbf{L}$  and  $\mathbf{C}$  the DM-DM matrices (Section 4.6.2);  $L_{CM} = Z_{CM}/c_0 = 870$  nH/m and  $\text{diag}(\mathbf{L}) = (L_s, L_s, L_s, L_s)$ ,  $L_s = 414$  nH/m. Since the diagonal elements of  $\mathbf{C}$  ( $\simeq 90$  pF/m)

are much larger than  $C_{s\infty}$ , the mutual capacitance  $C_{s\infty}$  is not added to these diagonal elements.

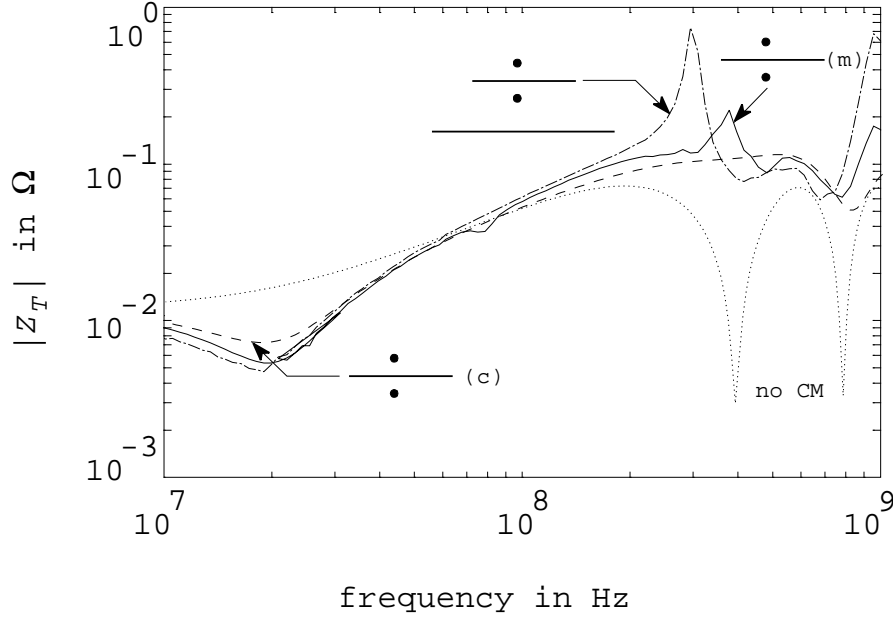


**Figure 4.16.** Measured (—) and calculated (---) transfer impedance  $|Z_T(1-2)|$  with  $68\ \Omega$  termination; curve ( $\cdots$ ) gives the calculated  $|Z_T(1-2)|$  neglecting the indirect DM-CM-DM coupling, i.e. without CM circuit or without TL5 in Fig. 4.14. For comparison we included the measured  $|Z_T|$  with a metallic plate at a distance of 5 cm from the PCB ( $-\cdot-\cdot-$ ), see main text.

In Fig. 4.16 the transfer impedance  $Z_T(1-2)$  is given for a free standing PCB. Since we are now mainly interested in the HF behavior, we only show the frequency range 10 MHz – 1 GHz. Measurements (—) and calculations (---) agree well. In the experiments brass plate *B* was removed. The calculated  $Z_T$  without CM circuit (TL5 in Fig. 4.14) is given by curve ( $\cdots$ ) for comparison.

A large brass plate was placed at a distance of approx. 5 cm parallel from the GP and in contact with brass plate *A*. The CM circuit is now better defined. Curve ( $-\cdot-\cdot-$ ) is the measured  $Z_T(1-2)$  for this situation. The nearby GP strongly reduces the mutual inductance and the mutual capacitance between the tracks. The indirect coupling DM-CM-DM now dominates  $Z_T$  and therefore resonant peaks at approx. 300 MHz and 920 MHz show up.

For frequencies larger than 200 MHz the  $Z_T$  reaches a plateau of approx.  $0.1\ \Omega$ . This coupling is important for high-current circuits (e.g. switched-mode power supply, digital circuits) together with low-noise circuits (e.g. operational amplifier). For example, a properly terminated ECL circuit with a fundamental current-amplitude of 14.8 mA at 230 MHz (see Table 3.1) generates a DM voltage in the other circuit 2 of approx. 1.5 mV.

## 4.7 More complicated tracks

The results of the previous section encouraged us to extend the TL method to more complicated tracks as on practical PCB's. Here we present the results on a PCB with a bend in

track 1 half way on the GP (PCB<sub>1</sub> in Fig. 4.17) and a meandering track 1 (PCB<sub>2</sub> in Fig. 4.17). The short perpendicular part(s)  $a$  to  $d$  were included in the TL picture as intermediate delay line(s); the CM circuit as described in the previous section was also included.

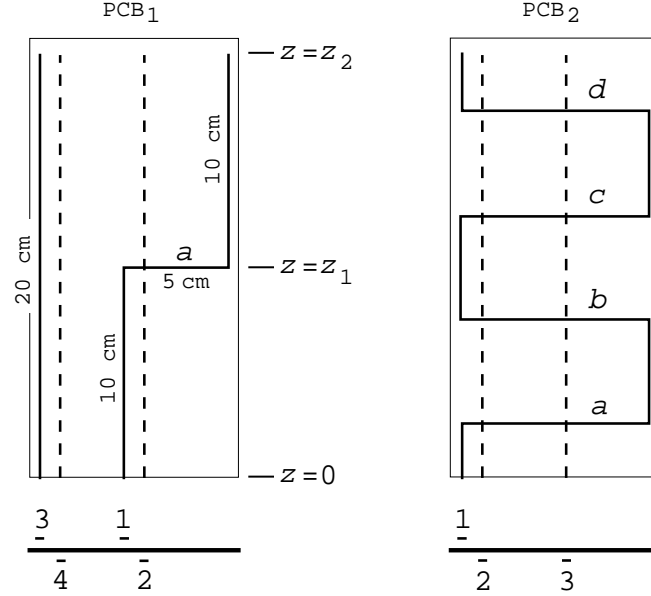


**Figure 4.17.** Two demonstration boards, PCB<sub>1</sub> and PCB<sub>2</sub>. Solid lines correspond to the upper layer of the PCB; dashed lines to the lower layer. The GP is the middle layer, with width  $2w = 10$  cm and lengths 20.5 cm; the straight tracks are  $\ell = 20$  cm long.

Figure 4.18 shows the DM-DM transfer impedance  $Z_T(1-2)$  with tracks shorted (s) or terminated in  $68 \Omega$  (t). The CM circuit (TL5 in Fig. 4.14) is formed by the GP and a return at large distance (Section 4.6.4), with only inductive couplings from the parallel tracks to this return. The inductive coupling from the orthogonal track  $a$  to the return is disregarded. The treatment is further the same as for the straight-track problem in Section 4.6.

The peak of  $Z_T(1-2)$  at 160 MHz for the shorted tracks correspond with the quarter-wavelength resonance of track 1 with total length  $\ell_1 = 25$  cm; the peak at 200 MHz with the corresponding resonance of the sensing track 2 with length  $\ell_2 = 20$  cm. The  $Z_T(1-2)$  and  $Z_T(1-3)$  results for the meandering track are shown in Fig. 4.19 (short-circuit case) and Fig. 4.20 (characteristic-termination case).

Good agreement between measurements and calculations are obtained up to approx. 500 MHz. At higher frequencies additional parasitic couplings to the CM circuit become more important; e.g. the capacitive coupling of the relative long orthogonal tracks  $a, \dots, d$  for PCB<sub>2</sub>. Nevertheless, the TL method gives good results when the tracks are on the same side where the couplings are much larger [Pau92a, Chapter 10].

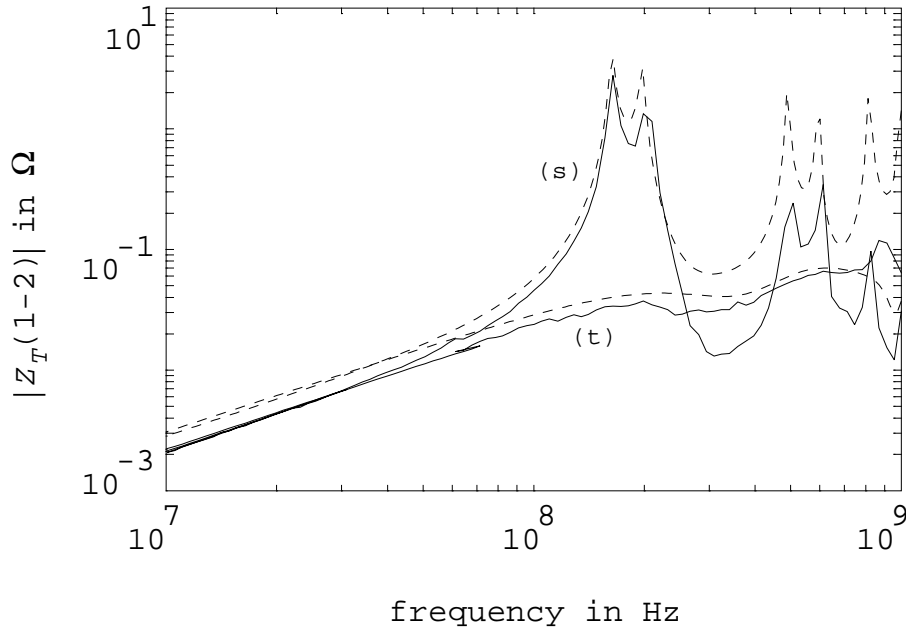


**Figure 4.18.** Measured (—) and calculated (---) DM-DM transfer impedance  $|Z_T(1-2)|$  for PCB<sub>1</sub> with shorted (s) and 68  $\Omega$  terminated (t) tracks.

#### 4.8 Concluding remarks

The  $M$ -part in the DM to DM crosstalk shows a strong position dependence when one or both tracks are near the edges of the GP. Both tracks at a distance  $3h_1$  from the edge already reduces the crosstalk by about one order of magnitude.

In our analysis we used 1.5 mm thick insulation. Many multilayer PCB have interlayer insulations of 0.2 mm, and correspondingly smaller tracks and track distances. There is also a tendency to reduce the copper-layer thickness. For such PCB's the analytical expressions for  $Z_t$  are valuable and the derived guidelines can help a designer to obtain an *a priori* estimate of the EMC properties of PCB's. Moreover, the expressions may be implemented in a PCB layout program to calculate or check 'online' violations of EMC rules; see also Chapter 5.

Our rapid and efficient TL method is also suitable for generating warnings for violations of EMC principles during the PCB design. A modern personal computer calculates different configurations in a few minutes; track positioning, placement of decoupling capacitors etc. could be optimized in a short time.

The TL method can be extended to even higher frequencies when three-dimensional effects are addressed more accurately, e.g. the capacitive coupling of the orthogonal tracks. The exact configuration of the CM circuit is also important for extension of the TL model, but this CM circuit is hard to identify for practical situations.



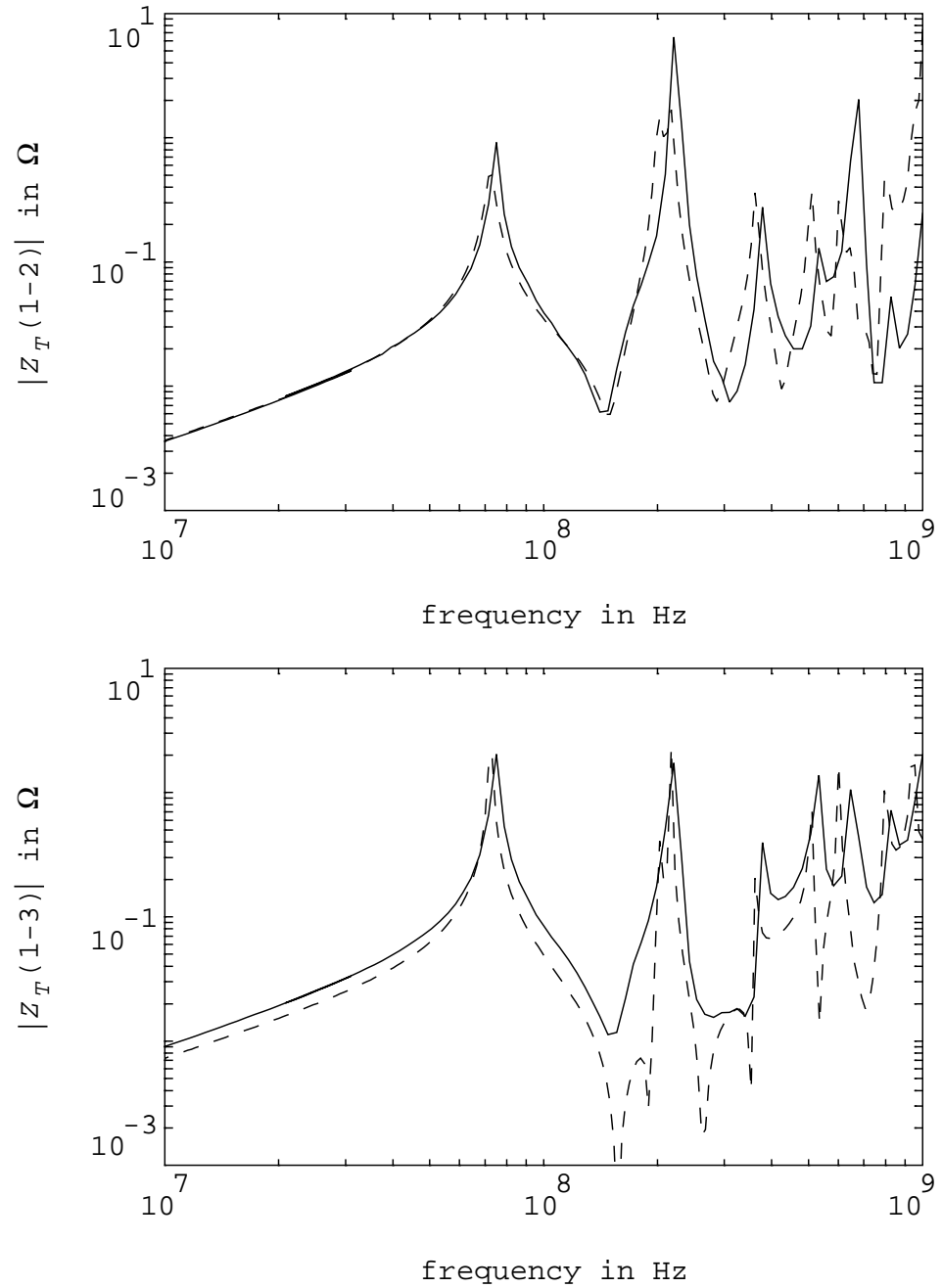


**Figure 4.19.** Measured (—) and calculated (---) DM-DM transfer impedance  $|Z_T(1-2)|$  and  $|Z_T(1-3)|$  for PCB<sub>2</sub> with shorted tracks.

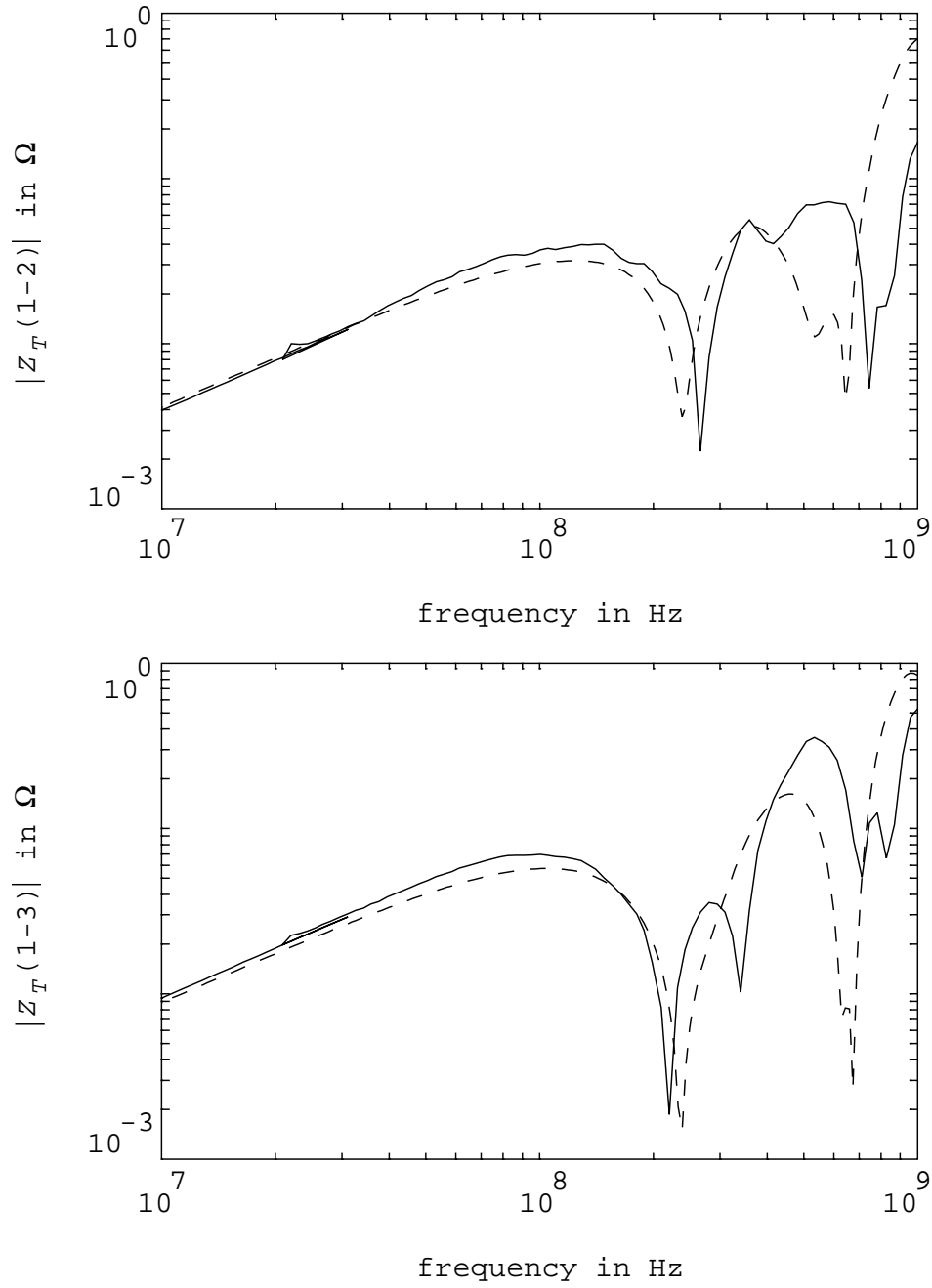


**Figure 4.20.** Measured (—) and calculated (---) DM-DM transfer impedance  $|Z_T(1-2)|$  and  $|Z_T(1-3)|$  for PCB<sub>2</sub> with 68  $\Omega$  terminated tracks.



# Chapter 5

## Implementation of EMC analysis into a design phase

### 5.1 Introduction

The EMC analysis presented in the previous chapters is suitable for incorporation in the PCB design phase of a product; a possible design-flow diagram is shown in Fig. 5.1. The most important objective is to avoid the large feedback loop from the prototype to the layout/placement process, since changes in the design after prototyping are expensive.

One option is to use cheap components, including the PCB itself, and to fix the EMC problems after prototyping. The cost per unit product of the redesign in high-volume electronics can be cheaper than the costs of the components. This approach is in general not advisable, since in the near future a redesign with cheap components may not be possible due to the increasing speed and complexity. Also, component variations can become a problem when a chip must be replaced by a newer and faster type. The proposed design flow in Fig. 5.1 is suitable for designing cost effective products, since the influence of the PCB topology and components can be calculated before any actual product has been built.

An important part of the diagram is the common-mode current calculation. Most PCB or chip designers concentrate on the radiated fields by the PCB itself, and omit the fields radiated by the attached cables. Only a few designers nowadays calculate the CM current by means of a full-wave analysis (FDTD or NEC) and to the best of our knowledge not by a rapid transmission-line approach. Therefore, it would be advantageous from an EMC point of view to incorporate our method into existing software.

In Section 5.2 we give a global description of the possible implementation as shown in Fig. 5.1. Section 5.3 concentrates on the CM current prediction during the placement/layout phase.

### 5.2 Global description

The design process starts with an idea (*a*)<sup>1</sup>, a functional design (*b*), and a functional simulation (*c*). The functional design and functional simulation can be further subdivided into, for example, modeling, requirement capture, validation, verification etc.; for more information see e.g. [Put97]. These steps are more or less independent of the board technology. After a successful functional simulation some initial choices have to be made (*d*), such as: PCB topology (number of layers, VCC/GND layers), logic type (HCT etc.), cabinet (metal, plastic), connector type etc. These choices are complex and depend on numerous factors. For

---

<sup>1</sup>The italic letters refer to the labeled blocks in the diagram

example, the cost effectiveness is one of the most important figures in consumer electronics. In general, the cheaper the components used (including board), the harder it becomes to obtain good EMC quality.

The physical design phase involves the component placement and routing (*e*); see for some placement and routing rules [Hen91]. The delays in the components and along the tracks should not exceed certain limits, as can be verified by a signal-integrity analysis SIA (*g*). It is advantageous to implement some EMC design rules and formulas (*j*) from the previous chapters already at this stage; for further details see Section 5.3. In addition to the SIA (*g*), also the CM current generation (*f*) must be considered, e.g. the CM current in the Bersier setup discussed in Chapter 3; in the next section we discuss the implementation of the current calculations during the routing process. The SIA and  $I_{CM}$ -prediction can be performed in parallel (blocks *f* and *g*). To achieve this one adds the CM circuit to the coupled TLs (*k*) for the interconnects which are also needed in the SIA. Even without a nearby plane the SIA must be extended with the DM-CM-DM conversion (*l*) as discussed in Section 4.6.4. Only if the SIA gives no problems AND the emission ( $3\ \mu\text{A}$ ) and immunity ( $10\ \text{mA}$ ) EMC requirements are fulfilled, an actual prototype can be considered. The limits for the emission and the immunity are based on standard tests; more severe or less stringent limits may be defined by the user if desirable. For frequencies where the EMC rules are critical, a further full-wave analysis (*i*) could be performed. However, the feedback from the time-consuming full-wave analysis (*i*) to the placement/routing process (*e*) is often not necessary.

The last step in the design process is building and testing the prototype (*h*). Practical experience shows that the product usually complies with the more elaborate regulatory EMC requirements when the simpler precompliance EMC rules are fulfilled.

### 5.3 Placement and layout phase

During the placement and layout phase it is advantageous to predict the CM current generated by DM currents through signal tracks; later on we will treat the immunity problem. Our proposed strategy for the emission problem is:

1. During routing estimate the CM current contribution generated by the DM current through an individual straight track;
2. Calculate the spectrum of the CM current generated by a complete net and store this spectrum for later use;
3. Add the stored spectra calculated of carefully selected bundles of transmission lines (e.g. data lines, address lines etc.) in the previous item for the complete PCB, this results in a worst-case CM current;
4. If this worst-case CM current is too high, calculate the design by the TL approach using only the ‘hot’ nets from item 2.

These items are explained below.

(1) The conducted emission treated in Section 3.3 is suitable for a first estimation of the CM current generation. For example, the digital waveform parameters of a DM current through a straight track are known either from data sheets or from the functional simulation. The mutual inductive coupling from any track to the CM circuit (Section 3.2) could be monitored permanently during the routing of that track. If the track does not run in parallel

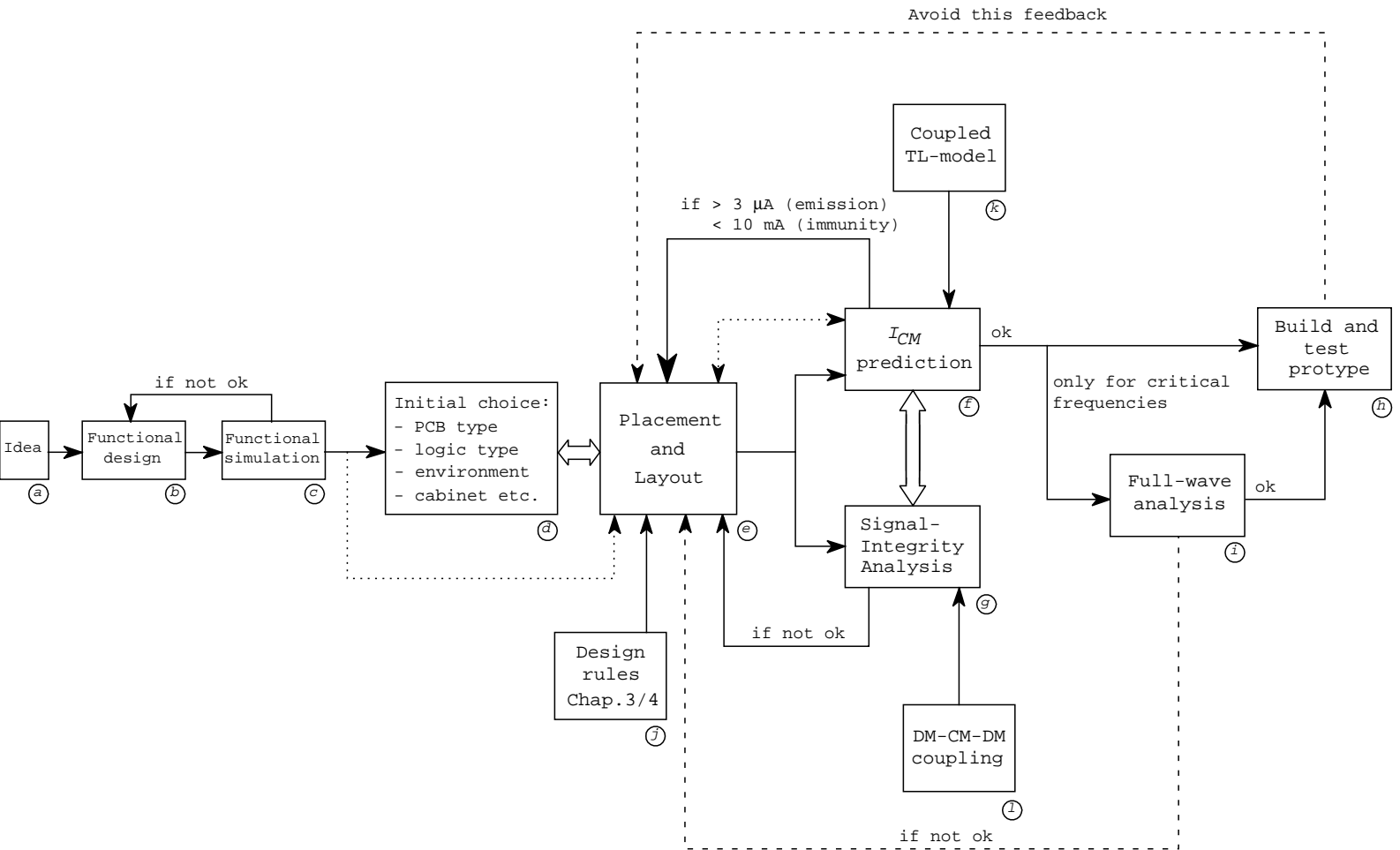


**Figure 5.1.** A flow diagram for the design process of a product. The italic letters by the blocks are explained in Section 5.2. The solid lines between the blocks refer to process steps and the dashed lines refer to process steps which should be avoided. Information exchange is indicated by the dotted lines.

with the CM circuit, it can be decomposed into a component parallel and a component orthogonal to the circuit; the same idea as is done with calculating the Manhattan distance. The upper boundary for the CM generated by the current is then estimated by Eq. (3.14). If the  $3\ \mu\text{A}$  emission rule is exceeded, a warning and/or possible solutions should be given.

The possible solutions depend strongly on the PCB type used. For single sided PCB's the best solution is using slower logic or reducing the supply voltage (when possible). Double sided PCB's without ground planes could be improved by adding extra grounding tracks or gridded grounds. With ground planes, the critical tracks should be moved to the middle of the GP's (Section 3.2); for multilayer PCB's these tracks can be buried between two GP's (Section 4.5) resulting in a tremendous decrease in CM current generation.

(2) The current distribution in a completely routed signal net can be calculated via the TL model, resulting in the prediction of the CM current. This is indicated by the bidirectional dotted line in Fig. 5.1 between the placement/layout block *e* and the  $I_{CM}$  prediction block *f*. In principle the source(s) and load(s) are available from the functional design; if not, a proper model should be selected from a library. The calculation (in the frequency or the time domain) of the current through the net should be done in the background while the PCB designer continue his work; the mutual interaction with other nets is neglected. The spectrum of the calculated CM current generation is stored for future purposes. Of course, if the CM current is too high a warning should be given. If the predicted CM current is below the limit, the process restarts with item 1 for other signal nets.

(3) If the board design is finished, the worst-case CM current generation results from the addition of the stored spectra of all routed signal nets. In this process bundles of transmission lines belonging to a group, such as data lines and address lines, should be considered in order to obtain a good guess. Apart from the total (worst-case) CM current, this rapid approach also gives the individual contributions of the nets.

(4) When the worst-case current exceeds the emission limit, the total timing should be taken into account. For this purpose only those nets which contribute the most to the CM current should be taken into account; these 'hot' nets are stored into memory. Therefore, time consuming calculations are avoided by minimizing the number of nets involved.

The current through supply nets could be treated in principle in the same manner. In practice, the high-frequency current through supply tracks depends strongly on the decoupling capacitors near IC's. Therefore, an estimation of the current through these tracks should be made; the TL method and corresponding CM current prediction are then applicable.

Up to now we concentrated on the emission problem. The reciprocal immunity problem is similar. The injected current is converted via the  $Z_t$  into disturbing voltages at the ends of a net. During routing these generated voltages can be calculated. For too high disturbing voltages a warning should be given.

# Chapter 6

## General conclusions

In practical cases disturbance currents or common-mode (CM) currents are often the main cause for interference. These currents through conducting structures belonging to devices generate interference voltages over sensitive terminals. The associated transfer impedance, defined by the ratio of the induced voltage and the disturbance current, describes the EMC quality of a device and turns out to be an excellent parameter to search for EMC solutions.

A new, simple, inexpensive, and sensitive workbench setup has been developed to determine the transfer impedance of shielded connectors. The main advantage over existing methods is the ease of mounting connectors in the setup. The injection current is measured by an inductive sensor integrated in the setup. The parameters of the current sensor can be calculated or measured. The transfer-impedance measurement does not require a calibration by means of a reference connector. The overall sensitivity of the workbench is  $3\ \mu\Omega$ . Transfer impedances down to  $0.1\ \text{pH}$  for connectors of maximum 3 cm length can be measured correctly for frequencies up to 1 GHz. Longer connectors can also be measured but at lower frequencies.

The common-mode currents generated by differential-mode (DM) circuits on a printed circuit board (PCB) with a continuous ground plane (GP) have been studied by means of a transmission-line (TL) model. These CM currents flow through the shields of attached cables; the electromagnetic-field emission from these cables often dominates the direct radiation from the board. The proposed method estimates the equivalent voltage source at the edge of the PCB by means of the TL approach. The measured and calculated CM current through an attached cable, modeled by a  $150\ \Omega$  impedance, agreed quite well.

The on board couplings or crosstalk between two DM circuits on a triple layer PCB with a continuous ground plane (GP) can also be expressed in terms of a transfer impedance. The induced voltage source at one end of a track caused by a differential-mode (DM) current through another track equals the transfer impedance times the disturbing DM current. General analytical expressions for this transfer impedance have been derived from the current distribution in the GP. The two-dimensional calculations for these expressions rely on different models, each adequate for a specific frequency range. The TL method extends the applicable range up to approx. 1 GHz, depending on the complexity of the board.

In both the CM-DM and the DM-DM couplings the high-frequency TL parameters are given by approximated values, applicable for a wide range. The rapid and efficient TL method with the analytical expressions is suitable for incorporation into a PCB design program. Such program should generate warnings for violations of EMC principles during the PCB design. The general analytical expressions are valuable to estimate the EMC properties of PCB's.





# Appendix A

## Conformal mapping

In this Appendix the high-frequency coupling from a circuit on a PCB with a continuous ground plane to another DM or CM circuit will be obtained by conformal mapping techniques. Sections A.1 and A.2 refer to the DM to CM coupling discussed in Chapter 3, where the PCB is placed above a metallic plane of infinite extent. The detailed derivation of the HF crosstalk treated in Chapter 4 is given in Sections A.3–A.6.

### A.1 Parallel plates

Suppose we have the parallel-plate system in the complex  $z$ -plane, see Fig. A.1a. The width of the plates is  $2w$  and their separation  $2h_{CP}$ . The transformation [Lov23]

$$z = \frac{2K'h_{CP}}{\pi} \left[ Z(s) + \frac{\pi s}{2KK'} \right], \quad (\text{A.1})$$

maps the upper side with cuts ABC and EFG of the  $z$ -plane onto the interior of a rectangle in the complex  $s = u + jv$ -plane (Fig. A.1b);  $K$  is the complete elliptic integral of the first kind of modulus  $k$ ,  $K'$  the same integral with modulus  $k' = \sqrt{1 - k^2}$ , and  $Z(s)$  Jacobi's Zeta function (see [Abr70]). Note that Abramowitz [Abr70] uses the parameter  $m = k^2$  in the definition of the integrals. This derivation remains the same for both definitions.

If  $h_{CP} \ll w$  the quotient of the integrals is given by [Lov23, pp. 342]

$$\frac{K'}{K} = \frac{w}{h_{CP}} \left[ 1 + \frac{h_{CP}}{\pi w} \left( 1 + \ln \frac{2\pi w}{h_{CP}} \right) \right]. \quad (\text{A.2})$$

Suppose now that the sensing wire resides near point  $G$  in the complex  $z$ -plane (Fig. A.1a), say at  $z = h_{CP} + h_1$ , then its image resides at  $s = K - u + jK'$ . We assume that  $h_1$  and  $u$  are small. When  $K'/K \gg 1$ , the  $q$ -series [Abr70, Eq. (17.4.38)] of the Zeta function yields

$$Z(s) = \frac{\pi}{K} \sum_{n=1}^{\infty} \frac{\sin \frac{n\pi s}{K}}{\sinh \frac{n\pi K'}{K}} \simeq \frac{2\pi}{K} \sum_{n=1}^{\infty} e^{-n\pi \frac{K'}{K}} \sin \frac{n\pi s}{K} \quad (\text{A.3})$$

The sine function in the summation simplifies for  $s = K - u + jK'$  to

$$\sin \frac{n\pi s}{K} \simeq \frac{j}{2} e^{n\pi \frac{K'}{K}} e^{-jn\pi \frac{K-u}{K}}, \quad (\text{A.4})$$

where the trigonometric sine-summation rule and  $\sinh p \simeq \cosh p \simeq e^p/2$  ( $p = n\pi K'/K \gg 1$ ) have been used. Substitution of Eq. (A.4) into Eq. (A.3) yields

$$Z(K - u + jK') \simeq -\frac{j\pi}{2K} \left[ 1 + j \tan \frac{\pi u}{2K} \right]. \quad (\text{A.5})$$

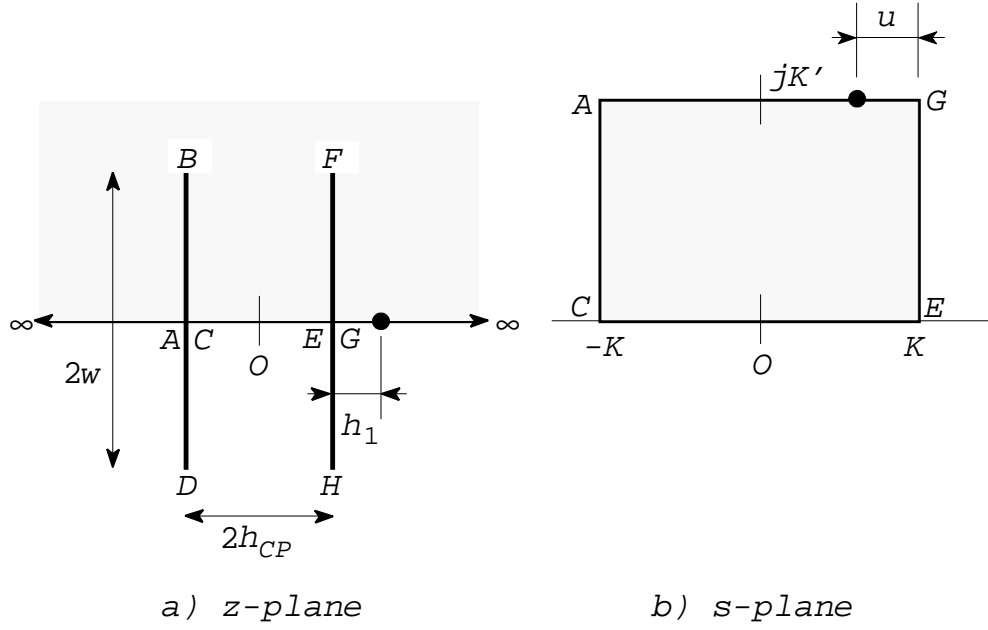


**Figure A.1.** The complex  $z = x + jy$  and  $s = u + jv$ -planes for the parallel plates  $BD$  and  $FH$ .

Substitution of  $z = h_{CP} + h_1$  and  $s = K - u + jK'$  in Eq. (A.1) finally results in the transcendental equation

$$h_{CP} + h_1 \simeq \frac{K'}{K} h_{CP} \left[ \tan \frac{\pi u}{2K} + \frac{K - u}{K'} \right]. \quad (\text{A.6})$$

Because  $K \simeq \pi/2$  and  $u \ll 1$ , the first-order approximation of the tangent can be used ( $\tan p \simeq p$ ), and so

$$u \simeq \frac{2K^2}{h_{CP}(K'\pi - 2K)} h_1. \quad (\text{A.7})$$

The mutual inductance  $M_s$  then simply follows from

$$M_s = \mu_0 \frac{u}{2K'} \simeq \mu_0 \frac{K}{K'} \frac{1}{\frac{K'}{K}\pi - 2} \frac{h_1}{h_{CP}}. \quad (\text{A.8})$$

With  $K'/K \simeq w/h_{CP} \gg 1$  one obtains the result presented in Section 3.2, Eq. (3.6).

## A.2 Approximate solution

A simpler but approximate derivation for the problem of the previous subsection can be found when  $h_{CP} \ll 2w$ . The transformation between  $z = x + jy$  and  $s = u + jv$

$$\frac{z}{z_0} = e^{s/s_0} - \frac{s}{s_0} - 1 \quad (\text{A.9})$$

maps the strip  $0 \leq v \leq \pi s_0$  in the  $s$ -plane on the  $z$ -plane with  $y > -\pi z_0$ ;  $s = 0$  is mapped onto  $z = 0$  (Fig. A.2). The origin of the coordinate system is now on the left edge of the GP. The image of the line  $v = j\delta$  with  $\delta \downarrow 0$  folds around the positive real axis in the  $z$ -plane.

In the  $s$ -plane we assume the parallel-plate transmission line of infinite extent in the  $u$ -direction. A first approximation  $\Phi_a$  of the flux per unit length between the plates is

$$\Phi_a = \mu_0 K_z h_{CP}, \quad (\text{A.10})$$

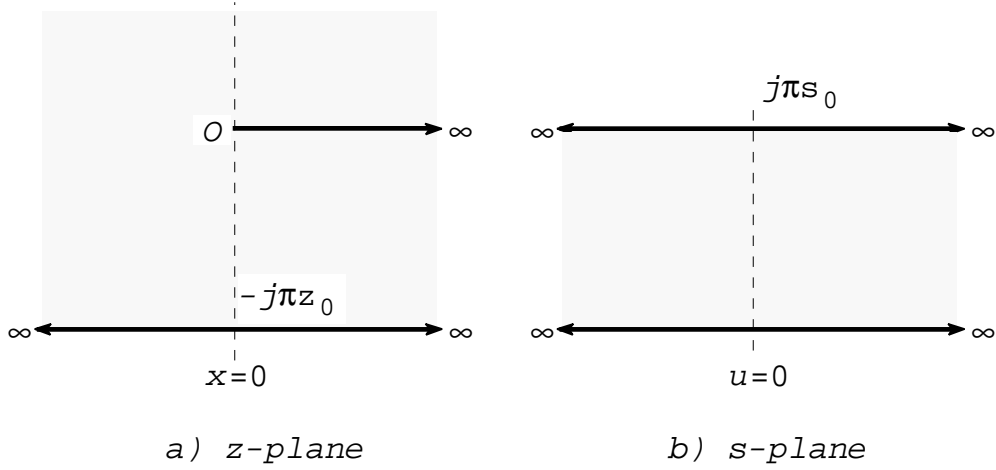


**Figure A.2.** The complex  $z = x + jy$  and  $s = u + jv$ -plane for the fringing field effects of a parallel plate system.

in which  $K_z$  is the sheet current density approximated by  $I/2w$ . The scaling factor  $s_0$  for the flux function  $v$  in the  $s$ -plane is  $\mu_0 K_z h_{CP}/\pi$ ; the scaling factor  $z_0$  for the  $z$ -plane is then  $h_{CP}/\pi$ . When we expand the exponential in Eq. (A.9) to the second degree, the first two terms cancel in the r.h.s. of Eq. (A.9). For a point  $jy$  near the edge of the PCB  $v/s_0 \simeq \sqrt{2|y|/z_0}$  holds approximately. The resulting  $M_s$  is presented as Eq. (3.7). Higher-order terms in the expansion soon become important. In Fig. A.3, we compare  $v$  from Eq. (A.9) to the second-order expansion with and without an additional correction term  $\Delta v$  fitted over the range  $-1 < y/z_0 < 1$ :

$$\Delta v/s_0 = \sum_{k=0}^2 c_k \left(\frac{y}{z_0}\right)^k \quad \text{with} \quad \begin{cases} c_0 &= +0.0023 \\ c_1 &= -0.3336 \\ c_2 &= +0.0568 \end{cases} \quad (\text{A.11})$$

where  $y$  is positive above the GP. This second-order fit in the least square sense is accurate to within 0.004 for  $v/s_0$ ; if restricted to the linear term only to within 0.06. The markers  $m_1$  and  $m_2$  on the horizontal axis in Fig. A.3 correspond to the height of the sensing wire; the markers  $m_1$  and  $m_2$  in Fig. 3.7a correspond to the same heights.

For a point  $z = w + jh_1$  above the middle line of the PCB,  $s$  is near the positive real axis; the exponential is the leading term in Eq. (A.9). One may then approximate the flux function by

$$v \simeq \text{Im} \log z = \arctan \frac{h_1}{w} \simeq \frac{h_1}{w}. \quad (\text{A.12})$$

The magnetic-field lines between the GP and the CP forms closed loops around the GP. The other edge of the PCB is taken into account by assuming that both edges contribute independently. For the position  $z = w + jh_1$  we multiply the flux function mentioned above by a factor of 2. Application the scaling for  $s$  and  $z$  results in Eq. (3.6) given in the main text, which was also obtained at the end of the Appendix A.1. For a point  $z = w - jh_1$  under the middle line of the PCB,  $s$  is close to the negative real axis; the exponential in Eq. (A.9) can be neglected. One easily verifies that the resulting  $M_s$  is equal to the one given in Eq. (3.3) of the main text.

In the comparison of the analytical values for  $M_s$  with the numerical and experimental values for sensing track positions close to the GP, the approximation of the total flux  $\Phi$  in

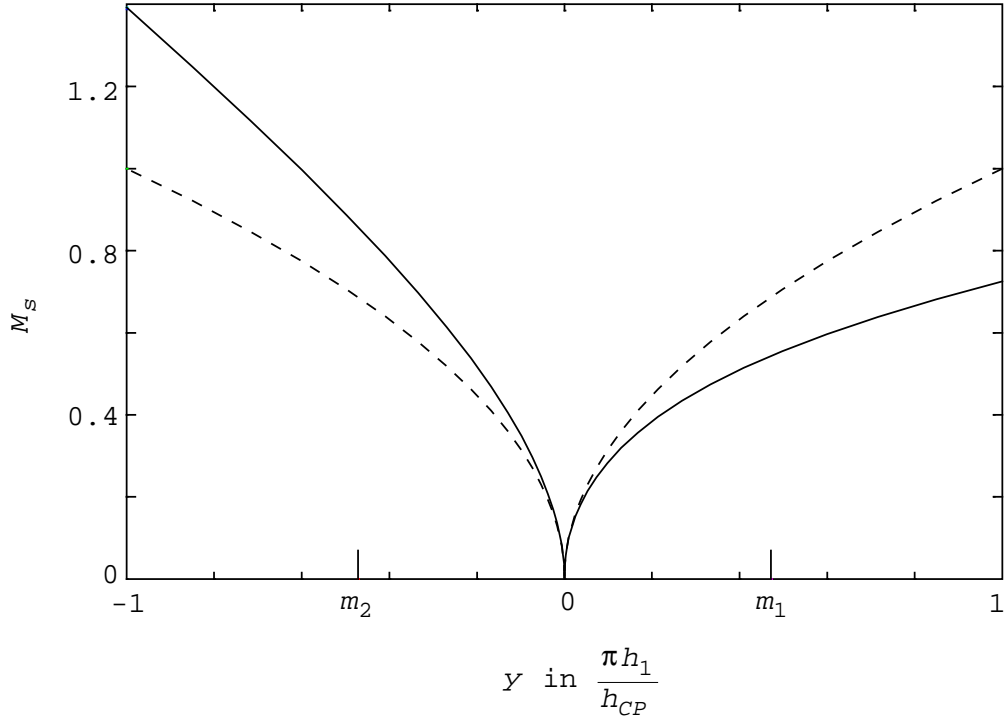


**Figure A.3.** The  $M_s$ -part of the CM to DM  $Z_t$  (—) in units  $\mu_0 h_{CP}/2\pi w$ , as function of height  $y$  of the sensing track at the edge of the GP. The approximation of Eq. (3.7) is also shown (- -). The markers  $m_1$  and  $m_2$  correspond to the height of the sensing wire.

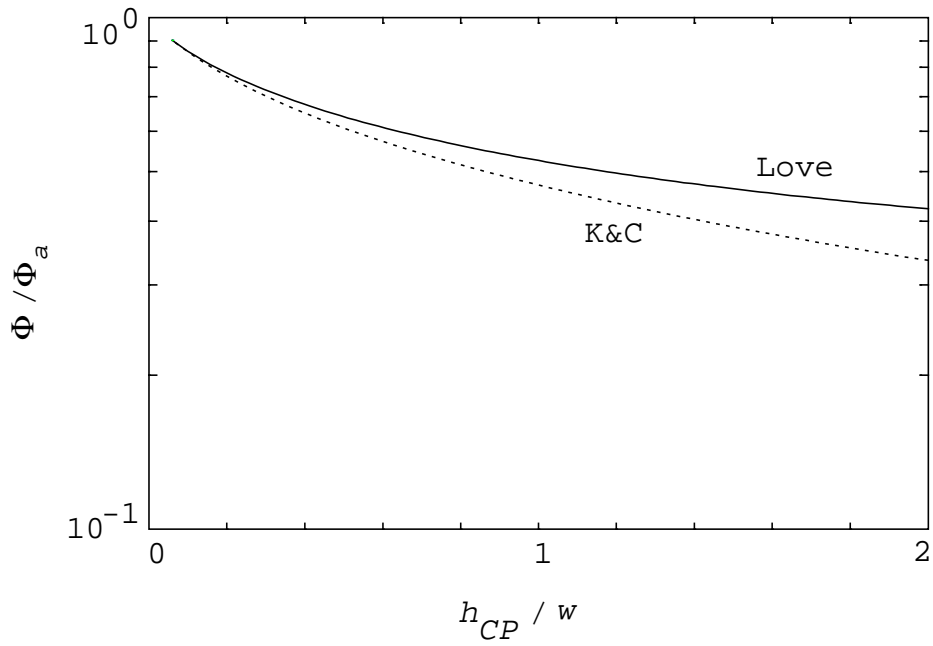


**Figure A.4.** The flux between a parallel-plate system as derived by Love, Eq. (A.13) and by Kuester and Chang (K&C), Eq. (A.14) compared to the simple approximation of a homogeneous field, Eq. (A.10).

Eq. (A.10) turned out to be too large even for small values of  $h_{CP}/w$ . Better approximations for  $\Phi$  are given by Love [Lov23, Section 3] and Kuester and Chang [Kue80, Eq. (14)] which are repeated here for convenience:

$$\Phi \simeq \frac{\mu_0 I_{CM} h_{CP}}{2w} \left[ 1 + \frac{h_{CP}}{\pi w} \ln \frac{2\pi w}{h_{CP}} \right]^{-1} \quad (\text{Love}) \quad (\text{A.13})$$

$$\simeq \frac{\mu_0 I_{CM}}{2} \left[ \frac{K[\text{sech}(\pi w/4h_{CP})]}{2K[\tanh(\pi w/4h_{CP})]} - \frac{h_{CP}^2}{2\pi w^2} \ln \left( 1 + \frac{4w^2}{ah_{CP}^2} \right) \right] \quad (\text{K\&C}), \quad (\text{A.14})$$

with  $K(k)$  being the complete elliptic integral and  $a = 2/\ln(4/\pi)$ . In Fig. A.4 we compare Eq. (A.10), (A.13) and (A.14); we used the last approximation for the  $M_s$ -curves in Fig. 3.7.

### A.3 Joukowski transformation

Suppose that the injection and sensing wire locate at coordinates  $z_1$  resp.  $z_2$  in the complex  $z = x + jy$ -plane (Fig. A.5). The infinitely thin GP is located on the real axis  $-w < x < w$ . The wire at  $z_1$  carries a current  $I_1$ , the GP a current  $-I_1$ . The Joukowski transformation [Kob57, pp. 58-60] and its inverse

$$\frac{z}{w} = \frac{1}{2} \left( t + \frac{1}{t} \right), \quad t = \frac{z}{w} + \sqrt{\left( \frac{z}{w} \right)^2 - 1}, \quad (\text{A.15})$$

map the outside of the GP in the  $z$ -plane and the outside of a unit circle in the complex  $t$ -plane onto each other, see Fig. A.5.

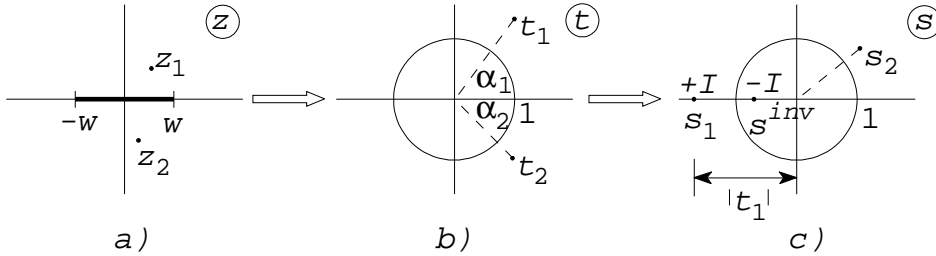


**Figure A.5.** a) The PCB structure of Fig. 4.1 is given in the complex  $z$ -plane by an infinitely thin GP of width  $2w$  located at the real  $x$ -axis. The tracks 1 and 2 are replaced by wires located at the positions  $z_1$  and  $z_2$ , respectively. b) The structure of a) transformed into the  $t$ -plane by means of a Joukowski mapping. c) The complex  $t$ -plane of b) rotated into the complex  $s$ -plane.

The square root in Eq. (A.15) is to be understood as principal value

$$\sqrt{p^2 - 1} := |p^2 - 1|^{\frac{1}{2}} e^{j(\arg(p-1) + \arg(p+1))/2}, \quad -\pi < \arg(p \pm 1) \leq \pi. \quad (\text{A.16})$$

This definition avoids the use of Riemann surfaces, because the upper/lower side of the GP is mapped onto the upper/lower side of the circle by means of Eq. (A.15). The transformation

$$s = te^{j(\pi - \alpha_1)}, \quad (\text{A.17})$$

rotates the transform  $t_1$  (injection wire) onto the negative real axis of the  $s = u + jv$ -plane, with  $\alpha_1$  being the principal value of the argument of  $t_1$ . The gradient of the real part of

the complex potential  $\Omega(s) = X(s) + j\Psi(s)$  gives the magnetic field  $\mathbf{H} = (\frac{\partial X}{\partial u}, \frac{\partial X}{\partial v})$ . The imaginary part of the potential represents the flux function at position  $s$ . The unit circle must be a flux tube. The required complex potential is the sum of the potential due to the wire 1 at  $s_1$  and of the potential due to a current  $-I_1$  at the inverse point  $s_1^{inv} = -|t_1|^{-1}$  of the injection wire (Fig. A.5) [Kad59]

$$\Omega(s) = -j\frac{I_1}{2\pi} \left[ \log(s + |t_1|) - \log\left(s + \frac{1}{|t_1|}\right) \right]. \quad (\text{A.18})$$

The principal value of the complex logarithm is used. The line dipole of strength  $I(s_1 - s_1^{inv})$  is centered at  $s = (s_1 + s_1^{inv})/2$ . The mutual inductance  $M$  is equal to the difference in the flux function between the transform of  $z_2$  and the unit circle

$$M = \frac{\Phi}{I_1} = \frac{\mu_0}{I_1} [\text{Im } \Omega(s_2) - \text{Im } \Omega(e^{j\phi_2})] = \frac{\mu_0}{I_1} [\Psi(s_2) - \Psi(e^{j\phi_2})], \quad (\text{A.19})$$

where  $\phi_2 = \arg(s_2)$ . The flux function on the circle is constant and is given by

$$\Psi(e^{j\phi_2}) = -\frac{I_1}{2\pi} \log |t_1|. \quad (\text{A.20})$$

Generally explicit real, closed forms for the mutual inductance cannot be calculated by means of Eqs. (A.15), (A.17), (A.18), and (A.19). Approximate analytical solutions for two limiting cases are given in the main text. However, the elementary functions used in the evaluation of  $M$  require little computational effort.

#### A.4 H-field lines for d.c.

A d.c. current  $I_1$  is homogeneously distributed over the GP. The complex potential, used to plot the d.c. field in Fig. 4.4a, is obtained by integration of the logarithmic potential due to the GP:

$$\Omega(z) = -j\frac{I_1}{2\pi} \left[ \log(z - z_1) + \frac{(z - z_3) \log(z - z_3) - (z - z_2) \log(z - z_2)}{z_3 - z_2} + 1 \right], \quad (\text{A.21})$$

in which  $z_{2,3}$  are the general end points of the GP. In our case  $z_2 = -w$  and  $z_3 = w$ . When the injection wire at  $z_1$  is close to the midpoint of the GP, the field lines assume the dipolar shape only at large distances  $|z|$ . The integral over the GP is identical to the expression given by Jaswon [Jas77, Chapter 11].

#### A.5 CM current

For a high-frequency common-mode current  $I_{CM}$  through a GP with its return far away, the complex potential takes the form:

$$\Omega(t) = -j\frac{I_{CM}}{2\pi} \log t. \quad (\text{A.22})$$

For any position on the unit circle  $|t| = 1$  and thus  $\text{Im}[\Omega(t)] = 0$ . For  $M$  one obtains:

$$M = \frac{\Phi}{I_{CM}} = \frac{\mu_0}{I_{CM}} [\text{Im } \Omega(t_1) - \text{Im } \Omega(t_c)] = \frac{\mu_0}{I_{CM}} \ln |t_1|, \quad (\text{A.23})$$

in which  $t_c$  is an arbitrary point on the unit circle.

### A.6 Track between two planes

In the  $z = x + jy$ -plane (Fig. A.2) the origin is at the leftmost edge of the top plane; assume the other plane at  $y = -2h_{PP}$  which also extends into the positive real direction. The plane  $y = -jh_{PP}$  is a symmetry plane in which the injection wire 1 resides at  $x_1 > 0$ . Wire 1 carries a current  $I_1$ . The transformation Eq. (A.9) and Fig. A.2 can only be used for the region  $y \geq -jh_{PP}$ , which suffices in our case. The scaling factor in Eq. (A.9) is  $z_0 = h_{PP}/\pi$ . Sensing wire 2 is at  $z_2 = x_2 + jy_2$  above the top plane.

Assume now the injection wire 1 in the  $s$ -plane at the position  $s_1 = u_1 + jv_1$  between two perfectly conducting planes at  $v = \pm\pi$ . The complex potential  $\Omega$  which describes the H-field between the planes and which satisfies the boundary condition  $\text{Im } \Omega = 0$  at these planes is:

$$\Omega(s) = \frac{-j\mu_0 I_1}{2\pi} \log \left[ \frac{\sinh[(s - s_1)/4]}{\cosh[(s - s_1^*)/4]} \right], \quad (\text{A.24})$$

with  $s_1^*$  being the complex conjugate of  $s_1$ . If  $s_1$  is halfway between the planes,  $v_1 = 0$ , and  $\text{Im } \Omega$  is symmetric with respect to the real axis.

For calculation of the mutual inductance,  $z_1/z_0$  and  $z_2/z_0$  are transformed by Eq. (A.9) with  $s_0 = 1$ . Both  $s_1$  and  $s_2$  are shifted over  $-j\pi$  before substitution in Eq. (A.24). The resulting  $M$  is shown in Fig. 4.13. A further simplification is possible when wire 1 is deeply buried between the planes, i.e.  $x_1 > h_{PP}$ , and  $z_2$  is above the top plane. Then  $|s_2 - s_1|$  is large and the argument of the logarithm in Eq. (A.24) is close to 1; the logarithm is then approximately  $-2e^{-(s_2 - s_1)/2}$ . The exponential in Eq. (A.9) can be neglected in the transformation for  $z_1$ . With these approximations  $M$  becomes

$$M(x_1, z_2) = -\frac{\mu_0}{\pi} \text{Im} \left[ \sqrt{\frac{z_0}{z_2}} e^{-(x_1 + z_0)/2z_0} \right]. \quad (\text{A.25})$$

This may be further simplified to Eq. (4.27) for the sensing wire at larger distances from the edges; note that in the main text the  $z$ -coordinate system is shifted.





# Appendix B

## Electrostatic potential theory and capacitance

Several approaches are possible for solving electromagnetic problems which involve perfectly conducting metallic structures and dielectrics. When only homogeneous dielectrics occur, the problem can be solved by means of equivalent sources; see Collin [Col91, Section 1.8] for a comprehensive overview. In this Appendix we will solve two-dimensional (2D) electrostatic problems. The small coupling capacitances involved are of main interest here. The analytical treatment and the numerical implementation are discussed in the first two subsections. Experiments show the importance of the discretization when the capacitances involved are small (of the order of fF/m), therefore the third subsection is devoted to the discretization. Finally, a comparison is made between the numerical solution and the analytical approximation (4.36) given in the main text.

### B.1 Analytical treatment

Electrical potential problems for finite two-dimensional structures have been solved in the past by several authors, see e.g. Harrington *et al.* [Har69], and more recently Venkataraman *et al.* [Ven85]. In this subsection a mathematical foundation for the resulting integral equations (IE's) over the conductor and dielectric-to-dielectric interfaces is given; for this and other methods see also [Atk97, Section 7.1]. In order to keep the derivation simple, i.e. avoiding a lot of bookkeeping, a simple structure is considered (see Fig. B.1). An extension to more complex structures is readily made.

Consider a two-dimensional dielectric body  $\mathcal{D}^+$  with relative permittivity  $\varepsilon_r$ , which is bounded by a simple smooth closed contour  $C = \cup C_k$  (see Fig. B.1);  $C_1$  and  $C_3$  are infinitely thin ideal conductors and  $C_2$  and  $C_4$  dielectric boundaries. The unbounded exterior region  $\mathcal{D}^-$  consists of a dielectric with relative permittivity  $\varepsilon_{r0}$ , e.g., vacuum. For convenience, we denote the dielectric-dielectric interfaces by  $C_d = C_2 \cup C_4$ .

The unit vector  $\mathbf{n}$  denotes the outward unit normal to  $C$ , and  $C$  is travelled counter-clockwise; the corresponding direction of the unit tangent  $\mathbf{u}$  to  $C$  is shown in Fig. B.1. The vector  $\rho$  denotes the position vector of the observation point  $(x, y) \in \mathbb{R}^2$ .

According to Harrington [Har69, Section 8.1], the potential at any point  $\rho \in \mathbb{R}^2 \setminus C$  can be represented by

$$\Phi(\rho) = \int_C \frac{\sigma_T(\rho')}{2\pi\varepsilon_0} \ln \frac{K}{|\rho - \rho'|} ds = \int_C \frac{\sigma_T(\rho')}{2\pi\varepsilon_0} \ln \frac{1}{|\rho - \rho'|} ds + K' \int_C \frac{\sigma_T(\rho')}{2\pi\varepsilon_0} ds, \quad (\text{B.1})$$

in which  $\rho' \in C$ ,  $s$  is the arc length along  $C$ ,  $\sigma_T$  is the total real-valued single-layer density

---

The author is indebted to prof. dr. J. Boersma from the Department of Mathematics and Computing Science, for carefully reading this appendix and the useful suggestions made.

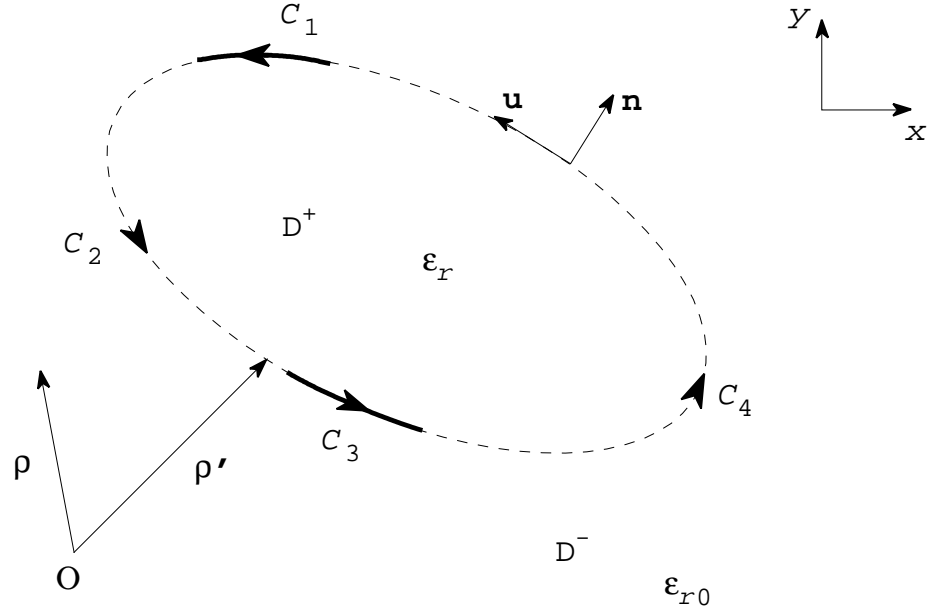


**Figure B.1.** Geometry of the problem.

and  $K > 1$  is an arbitrary constant; therefore  $K' = \ln K$  is also an arbitrary positive constant. Since  $\Phi(\rho)$  is harmonic for  $\rho \in \mathbb{R}^2 \setminus C$  and regular at infinity, the potential must be bounded for  $|\rho| \rightarrow \infty$ . This condition can only be satisfied when the total charge equals zero, i.e.

$$\int_C \sigma_T(\rho') ds = 0. \quad (\text{B.2})$$

The potential (B.1) of the single layer is continuous at all points on the curve  $C$ ; see e.g. Tikhonov and Samarskii [Tik90, Section IV.5]. Thus we are led to the integral equations

$$\int_C \frac{\sigma_T(\rho')}{2\pi\epsilon_0} \ln \frac{K}{|\rho - \rho'|} ds = V_1, \quad \rho \in C_1, \quad (\text{B.3})$$

$$\int_C \frac{\sigma_T(\rho')}{2\pi\epsilon_0} \ln \frac{K}{|\rho - \rho'|} ds = V_3, \quad \rho \in C_3, \quad (\text{B.4})$$

where  $V_1$  and  $V_3$  are the prescribed potentials at conductors  $C_1$  and  $C_3$ , respectively.

The electric field  $\mathbf{E}(\rho)$  is given by

$$\mathbf{E}(\rho) = -\nabla\Phi(\rho). \quad (\text{B.5})$$

The normal component of the electric flux density  $\mathbf{D}$  must be continuous at the dielectric-dielectric interface  $C_d$ , therefore

$$\epsilon_r \mathbf{n} \cdot \nabla\Phi(\rho^+) = \epsilon_{r0} \mathbf{n} \cdot \nabla\Phi(\rho^-), \quad (\text{B.6})$$

where  $\nabla\Phi(\rho^\pm) = \lim_{\delta \downarrow 0} \nabla\Phi(\rho \mp \delta \mathbf{n})$ , and  $\rho \in C_d$ . Since  $\mathbf{n} \cdot \nabla$  equals the normal derivative, the boundary condition (B.6) for  $\rho \in C_d$  yields [Tik90, Section IV.5]

$$\epsilon_r \left[ \frac{\partial\Phi(\rho)}{\partial n} + \frac{\sigma_T(\rho)}{2\epsilon_0} \right] = \epsilon_{r0} \left[ \frac{\partial\Phi(\rho)}{\partial n} - \frac{\sigma_T(\rho)}{2\epsilon_0} \right], \quad \rho \in C_d, \quad (\text{B.7})$$

with

$$\frac{\partial \Phi(\rho)}{\partial n} = - \int_C \frac{\sigma_T(\rho')}{2\pi\epsilon_0} \frac{d}{dn} \ln |\rho - \rho'| ds = \int_C \frac{\sigma_T(\rho')}{2\pi\epsilon_0} \frac{\cos \varphi}{|\rho - \rho'|} ds, \quad \rho \in C_d, \quad (\text{B.8})$$

where  $\varphi$  is the angle between  $\mathbf{n}$  and the direction from  $\rho$  to  $\rho'$ . Observe that the integral is proper since the  $\lim_{\rho' \rightarrow \rho} \cos \varphi / |\rho - \rho'|$  exists. The resulting integral equation for an observation point  $\rho \in C_d$  becomes

$$\frac{\epsilon_r + \epsilon_{r0}}{2\epsilon_0} \sigma_T(\rho) + \frac{\epsilon_r - \epsilon_{r0}}{2\pi\epsilon_0} \int_C \sigma_T(\rho') \frac{\cos \varphi}{|\rho - \rho'|} ds = 0, \quad \rho \in C_d. \quad (\text{B.9})$$

A frequently used method to solve the coupled IE's (B.3), (B.4), and (B.9) is the method of moments (MOM), see Harrington [Har69, Har93]. One of the simplest procedures expands  $\sigma_T$  in a series of pulse functions; see the next subsection. Point matching for testing yields a (non-singular) matrix equation from which  $\sigma_T$  follows.<sup>1</sup>

When the total single-layer density  $\sigma_T$  is known, the free-charge densities  $\sigma_F$  on the conductors are obtained by [Ven85, Section III]

$$\sigma_F(\rho) = \frac{\epsilon_r + \epsilon_{r0}}{2} \sigma_T(\rho) + \frac{\epsilon_r - \epsilon_{r0}}{2\pi} \int_C \sigma_T(\rho') \frac{\cos \varphi}{|\rho - \rho'|} ds, \quad (\text{B.10})$$

with  $\rho \in C_1$  and  $\rho \in C_3$  for conductors  $C_1$  and  $C_3$ , respectively.

When conductor  $C_1$  is energized with potential  $V_1 \neq 0$  and holding  $V_3 = 0$  at conductor  $C_3$ , the capacitance  $C_{13}$  between the conductors equals the quotient  $-Q_3/V_1$  with

$$Q_3 = \int_{C_3} \sigma_F(\rho') ds \quad (\text{B.11})$$

the total induced free-charge on conductor  $C_3$ . In this case  $Q_3$  equals the total free-charge  $-Q_1$  on conductor  $C_1$ .

## B.2 Numerical implementation

The numerical implementation is carried out in complex arithmetic. Let  $z = x + jy \in \mathbb{C}$  represent a point  $(x, y) \in \mathbb{R}^2$  in space, and let  $u = u_x + ju_y$  the complex representation of the unit tangent vector  $\mathbf{u} = (u_x, u_y)$  along  $C$ . The electric field  $\mathbf{E} = (E_x, E_y)$  is denoted by  $E = E_x + jE_y$  in the complex domain.

Consider finite structures (as in Fig. B.1) in which the boundary consists of straight lines. The structure consists of  $N_c$  conductors and  $N_d$  dielectric interfaces;  $N_c = N_d = 2$  for the structure given in Fig. B.1. The  $N_c$  conductors are subdivided into  $k$  straight-line segments and the  $N_d$  dielectric interfaces are subdivided into  $n$  straight-line segments. The set  $Sc = \cup_{i=1}^k S_i$  contains the  $k$  conductor segments, whereas the set  $Sd = \cup_{i=k+1}^{k_t} S_i$ ,  $k_t = k + n$ , contains the  $n$  dielectric segments. The total boundary then equals  $S = Sc \cup Sd = \cup_{i=1}^{k_t} S_i$ .

A segment  $S_j$  (see Fig. B.2) with vertices  $\{z_j, z_{j+1}\}$  has length  $l_j$ . We approximate the actual single-layer density  $\sigma_T$  by a uniform single-layer density  $\sigma_{Tj}$  on  $S_j$ . When the segment  $S_j$  is travelled from  $z_j$  to  $z_{j+1}$ , the relative permittivity is denoted by  $\epsilon_{rl,j}$  and  $\epsilon_{rr,j}$  as the left-hand and right-hand sides of  $S_j$ , respectively. The normal  $\mathbf{n}_j$  points to the right-hand side of  $S_j$  (see Fig. B.2), in accordance with Fig. B.1.

<sup>1</sup>In the mathematical literature the MOM is called a (discrete) projection method and MOM with point matching the collocation method [Atk97, Chap. 3].

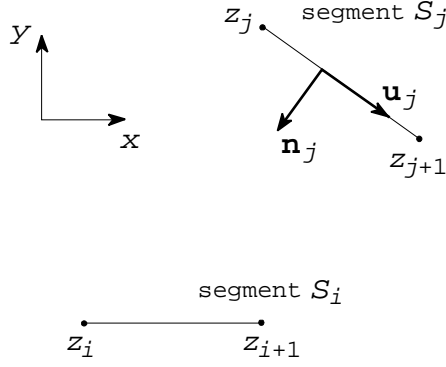


**Figure B.2.** Two line segments.

The complex potential  $\psi(z)$  at  $z \in \mathbb{C}$  in 2D due to a line charge at  $z' \neq z$  is given by  $\psi(z) = -\log(z - z')/2\pi\epsilon_0 + K_1$  ( $K_1$  arbitrary positive). The potential  $\psi_i(z)$  at  $z$  due to a constant single-layer density  $\sigma_{Ti}$  along a segment  $S_i$  with vertices  $\{z_i, z_{i+1}\}$  (see Fig. B.2) equals for  $z \notin S_i$  [Har69, Section 3]

$$\begin{aligned}\psi_i(z) &= \frac{\sigma_{Ti}}{2\pi\epsilon_0} \frac{1}{u_i} \int_{z_i}^{z_{i+1}} \log \frac{K_2}{z - z'} dz' \\ &= \frac{\sigma_{Ti}}{2\pi\epsilon_0} \left[ \frac{z - z_i}{u_i} \log \frac{z - z_{i+1}}{z - z_i} + l_i \left( 1 + \log \frac{K_2}{z - z_{i+1}} \right) \right],\end{aligned}\quad (\text{B.12})$$

with  $K_2 > 1$ . This complex function is made single-valued by introducing a cut along  $S_i$ .

For the electric field  $E$  at  $z \notin S_i$  we find

$$E(z)^* = E_x(z) - jE_y(z) = -\frac{d\psi_i(z)}{dz} = -\frac{\sigma_{Ti}}{2\pi\epsilon_0} \frac{1}{u_i} \log \left( \frac{z - z_{i+1}}{z - z_i} \right), \quad (\text{B.13})$$

which is single-valued due to the cut along  $S_i$ . The normal component  $E_n$  of the electric field on a segment  $S_j \neq S_i$ , becomes (see [Har69, Section 3])

$$E_n(z) = -\text{Re} \left[ n_j \frac{d\psi_i(z)}{dz} \right] = -\text{Im} \left[ u_j \frac{d\psi_i(z)}{dz} \right], \quad z \in S_j, \quad i \neq j, \quad (\text{B.14})$$

with  $n_j$  and  $u_j = jn_j$  the complex representations of the normal  $\mathbf{n}_j$  and tangent  $\mathbf{u}_j$  vectors on segment  $S_j$ , respectively. For  $i = j$  we have,

$$E_n(z) = -\text{Im} \left[ u_j \frac{d\psi_j(z)}{dz} \right] = -\frac{\sigma_{Tj}}{2\pi\epsilon_0} \text{Im} \left[ \log \left( \frac{z - z_{j+1}}{z - z_j} \right) \right] = \mp \frac{\sigma_{Tj}}{2\pi\epsilon_0}, \quad z \in S_j \in S, \quad (\text{B.15})$$

in which the minus sign is taken for the normal electric field at the left-hand side of  $S_j$  and the positive sign is taken for the right-hand side.

Let  $E_{nt,j}$  denote the ‘total’ normal component of the electric field at segment  $S_j$  due to the single-layer density  $\sigma_{Ti}$  at segments  $S_i$ , with  $i = 1, \dots, k_t$ , and  $i \neq j$ . By means of (B.14) we have

$$E_{nt,j}(z) = -\sum_{\substack{i=1 \\ i \neq j}}^{k_t} \text{Im} \left[ u_j \frac{d\psi_i(z)}{dz} \right], \quad z \in S_j \in S. \quad (\text{B.16})$$

The normal electric-field components at the left-hand and right-hand sides of  $S_j$  are denoted by  $E_{nl,j}$  and  $E_{nr,j}$ , which become by means of (B.15)

$$E_{nl,j}(z) = E_{nt,j}(z) - \frac{\sigma_{Tj}}{2\varepsilon_0} \quad \text{and} \quad E_{nr,j}(z) = E_{nt,j}(z) + \frac{\sigma_{Tj}}{2\varepsilon_0}, \quad (\text{B.17})$$

with  $z \in S_j \in S$ .

Since the conductors are imbedded in dielectrics, the conductor segment  $S_j \in Sc$  is contained in dielectrics. The total single-layer density  $\sigma_{Tj}$  can be split into its free component  $\sigma_{Fj}$  and the bounded polarization component  $\sigma_{Bj}$ . The normal component of the dielectric flux density  $\mathbf{D}$  is discontinuous over the conductor segment  $S_j$  and equals

$$\sigma_{Fj}(z) = D_{nr,r}(z) - D_{nl,r}(z) = \varepsilon_0 \varepsilon_{rr,j} E_{nr,j}(z) - \varepsilon_0 \varepsilon_{rl,j} E_{nl,j}(z), \quad z \in S_j \in Sc \quad (\text{B.18})$$

with  $D_{nl,j}$  and  $D_{nr,j}$  denoting the normal  $D$ -field components at the left-hand and right-hand sides of  $S_j$ , respectively. Observe that (B.18) also holds at a dielectric-interface segment  $S_j \in Sd$  because there  $\sigma_{Fj} = 0$ . Substitution of (B.17) in (B.18) yields

$$\sigma_{Fj}(z) = (\varepsilon_{rr,j} + \varepsilon_{rl,j}) \frac{\sigma_{Tj}}{2} + (\varepsilon_{rr,j} - \varepsilon_{rl,j}) \varepsilon_0 E_{nt,j}(z), \quad z \in S_j \in Sd. \quad (\text{B.19})$$

A matrix equation is obtained by using point matching; e.g. choose the midpoint  $z = z_{mj} = (z_j + z_{j+1})/2$  at every segment  $S_j$ ,  $j = 1, \dots, k_t$ . The electrical potential should be constant on the conductors. Let the potentials on the  $N_c$  conductors be denoted by  $V_p$ ,  $p = 1, \dots, N_c$ . On the conductor segment  $S_j$  that is part of the conductor  $p$ , the potential is given by  $V_{sj} = V_p$ . The complex potential due to a constant single-layer density  $\sigma_{Ti}$  along the segment  $S_i \in S$  is given by (B.12). The real part of (B.12) yields the electrical potential, which is continuous for  $z \in S_i$ . One obtains

$$\text{Re} \left[ \sum_{i=1}^{k_t} \psi_i(z_{mj}) \right] = V_{sj}, \quad j = 1, \dots, k. \quad (\text{B.20})$$

This may be written as a matrix equation

$$\Psi \sigma_{\mathbf{T}} = \mathbf{V}_{\mathbf{s}}, \quad (\text{B.21})$$

with  $\Psi$  a  $k \times k_t$  matrix,  $\sigma_{\mathbf{T}} = (\sigma_{T1}, \dots, \sigma_{Tk_t})^T$ , and  $\mathbf{V}_{\mathbf{s}} = (V_{s1}, \dots, V_{sk_t})^T$ .

Almost the same procedure can be used for the dielectric-interface segments  $S_i \in Sd$ . One obtains by means of (B.16), (B.19), and  $\sigma_{Fj} = 0$

$$(\varepsilon_{rr,j} + \varepsilon_{rl,j}) \frac{\sigma_{Tj}}{2} + (\varepsilon_{rr,j} - \varepsilon_{rl,j}) \varepsilon_0 E_{nt,j}(z_{mj}) = 0, \quad j = k+1, \dots, k_t. \quad (\text{B.22})$$

This system may be shortly written as

$$\Psi_{\mathbf{d}} \sigma_{\mathbf{T}} = \mathbf{0}, \quad (\text{B.23})$$

with  $\Psi_{\mathbf{d}}$  a  $n \times k_t$  matrix representing (B.22) and  $\mathbf{0}$  the  $n$ -zero vector.

The total matrix equation becomes

$$\begin{bmatrix} \Psi \\ \Psi_{\mathbf{d}} \end{bmatrix} \sigma_{\mathbf{T}} = \begin{bmatrix} \mathbf{V}_{\mathbf{s}} \\ \mathbf{0} \end{bmatrix}, \quad (\text{B.24})$$

from which  $\sigma_{\mathbf{T}}$  can be solved once the constant  $K_2$  in (B.12) is known. This constant vanishes when the first row of the matrix equation (B.21) is subtracted from the other rows. Since the total charge must be zero, this condition is forced explicitly by replacing the  $k_t$  elements of the first row of matrix  $\Psi$  by  $l_i$ ,  $i = 1, \dots, k_t$  and the first element of  $\mathbf{V}_s$  is made zero; see [Ven85]. Note that conductor  $p$  belonging to the first row is now at zero potential, therefore the potentials on the other conductors are relative to conductor  $p$ .

The free-charge density  $\sigma_F$  follows from (B.19). The free charge on a conductor  $p$  is the sum of  $\sigma_{Fi}l_i$  over the conductor segments  $S_i$  that belong to conductor  $p$ .

### B.3 Discretization

The discretization<sup>2</sup> method is applied to the three-layer PCB placed in vacuum (see Fig. B.3); the dielectric boundaries are given by the dashed lines. Our main interest is the small capacitive coupling  $C_{12}$  from track 1 to track 2; the self-capacitance  $C_1$  is also given. The middle layer was a  $2w = 10$  cm wide ground plane GP. The tracks of width  $b = 1.5$  mm were located at a distance  $h_1 = 1.5$  mm above and  $h_2 = 1.5$  mm below the GP. The epoxy layer (- - - in Fig. B.3) had a homogeneous dielectric permittivity  $\epsilon_r = 4.7$ . The position of both tracks resulted in a minimum coupling capacitance.

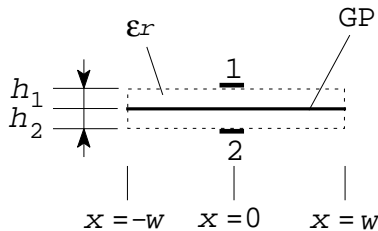


**Figure B.3.** Three layer PCB with an ideal ground plane (GP) of width  $2w$ . The ideal tracks of width  $b$  are located  $h_1$  and  $h_2$  above and below the GP, respectively.

We first consider the situation with the dielectric absent, i.e. only the conductors remain in vacuum. Later the dielectric is added.

#### No dielectric present

Without dielectric a first-order approximation of  $C_{12}$  is given by Kaden [Kad59, Eq. (I.10)]

$$C_{12}^a = \frac{h_1 h_2 C_1 C_2}{4\pi\epsilon_0 w^2}, \quad (\text{B.25})$$

in which  $C_1, C_2$  are the self capacitances (see expression (4.28) in the main text with  $\epsilon_{r,eff} = 1$ ); for our situation  $C_1 = C_2 = 26.8$  pF/m.

Numerically  $C_{12}$  and  $C_1$  were obtained by applying a potential  $V_1 = 1$  at track 1 with  $V_2 = V_{GP} = 0$ . The induced free-charges  $Q_2 (< 0)$  on track 2 and  $Q_{GP} (< 0)$  on GP were obtained by means of the method discussed at the end of the previous subsection. Then  $C_{12} = -Q_2/V_1$  and  $C_1 = -Q_{GP}/V_1$ .

<sup>2</sup>In mathematical literature an ‘optimal’ mesh is called a graded mesh. An error analysis of an IE with weakly singular kernel on a piecewise smooth planar boundary  $C$  has been developed around the mid 80’s. This analysis is carried out on Sobolev spaces and extensively uses functional analysis. The theory goes beyond this text and the interested reader is referred to [Atk97, Chapters 7 and 8].

Track 1, track 2, and the ground plane GP are divided into  $k_1$ ,  $k_2$ , and  $k_3$  segments; the total number of segments is denoted by  $k_t = k_1 + k_2 + k_3$ . In the homogeneous-discretization case all segments belonging to the same conductor have equal lengths. The lengths of these segments are not equal for the nonhomogeneous-discretization case, to be discussed below.

In Table B.1 the  $C_{12}$  and  $C_1$  sequences are given for a homogeneous (h) discretization. The first-order analytical approximation (B.25) leads to  $C_{12}^a = 5.81$  fF/m. The numerical  $C_{12}$ -sequence seems to converge to the exact value when the number of segments is increased. Observe also that the numerically and analytically obtained self-capacitance  $C_1$  agree within 3.5 percent.

**Table B.1.** Coupling capacitance  $C_{12}$  and self-capacitance  $C_1$  for the structure of Fig. B.3 without dielectric: results for a homogeneous (h) and a nonhomogeneous (nh) discretization (see text). The number of segments used in track 1 ( $k_1$ ), track 2 ( $k_2$ ), and GP ( $k_3$ ) is denoted by  $(k_1, k_2, k_3; k_t)$ , with  $k_t = k_1 + k_2 + k_3$  the total number of segments.

|                             | $(k_1, k_2, k_3; k_t)$ |                 |                 |                 |                 |
|-----------------------------|------------------------|-----------------|-----------------|-----------------|-----------------|
|                             | (10,10,50;70)          | (20,20,100;140) | (20,20,200;240) | (20,20,400;440) | (20,20,800;840) |
| $C_{12}(\text{h})$ in fF/m  | 52.76                  | 16.73           | 6.91            | 5.72            | 5.57            |
| $C_{12}(\text{nh})$ in fF/m | 5.46                   | 5.58            | 5.59            | 5.63            | 5.63            |
| $C_1(\text{h})$ in pF/m     | 25.87                  | 26.14           | 26.17           | 26.17           | 26.17           |
| $C_1(\text{nh})$ in pF/m    | 26.34                  | 26.37           | 26.37           | 26.37           | 26.37           |

Another approach is a nonhomogeneous (nh) discretization with a fixed number of segments per conductor. Since the tangential electric field  $E_{tan}$  of an ideal conductor is zero, the error  $\eta_j$  at segment  $S_j$ , defined by:

$$\eta_j = \sum_{i=1}^k \int_{S_j} |E_{tan,i}^j| |dz|, \quad (\text{B.26})$$

is a measure for the deviation of the calculated tangential-field compared with the physical ‘zero-field’;  $E_{tan,i}^j$  denotes the numerically calculated tangential field at  $S_j$  due to a single-layer density  $\sigma_{Fi}$  along a segment  $S_i$ .

In an iterative process the discretization is changed: the process starts with a homogeneous discretization. The next steps are: (1) The error  $\eta_j$  of segment  $S_j$ ,  $j = 1, \dots, k_t$  is determined by calculating the (real) potential at several additional points on each conductor segment by using the complex potential. (2) The cumulative sum of  $\eta_j$  for the segments  $S_j$  belonging to the same conductor is determined. (3) This cumulative sum is used to redistribute the segments over the conductor where they belong to: a finer discretization where the sum changes fast. The total number of segments per conductor is kept constant. (4) The process iterates from step (1) until every segment  $S_j$  belonging to same conductor contributes the same error  $\eta_j$  and the total error per conductor converges to within a certain percentage; in the calculations 2 percent was used.

Table B.1 shows the calculated  $C_{12}$  and  $C_1$  for this nonhomogeneous case; the total error of 2 percent per conductor was reached in 6 iterations. With relatively few segments (in this case 70) the coupling capacitance  $C_{12}$  can be accurately calculated. The numerically calculated self-capacitance  $C_1$  agrees within 2 percent compared to the analytically obtained value of 26.8 pF/m.



### Dielectric present

The dielectric boundaries (- - -, Fig. B.3) and the conductors of the PCB structure are divided into  $k_t$  segments. Again, track 1, track 2, and the ground plane GP are divided into  $k_1$ ,  $k_2$ , and  $k_3$  segments. The remaining  $k = k_t - k_1 - k_2 - k_3$  segments are distributed proportional to and equally spaced along the length of the eight straight dielectric interfaces. In the homogeneous-discretization case all segments belonging to the same dielectric-interface/conductor have equal lengths. The lengths of these segments varied for the nonhomogeneous-discretization case.

First results showed a large variation of the normal electric field  $\mathbf{E}_n$  along the dielectric interfaces. Therefore, (B.19) is integrated over a dielectric-interface segment  $S_j \in Sd$ . By means of

$$\int_{z_j}^{z_{j+1}} E_n |dz| = -\text{Im} [\psi_i(z_{j+1}) - \psi_i(z_j)], \quad (\text{B.27})$$

and  $\sigma_{Fj} = 0$  we have

$$(\varepsilon_{rr,j} + \varepsilon_{rl,j}) \frac{\sigma_{Tj}}{2} l_j - (\varepsilon_{rr,j} - \varepsilon_{rl,j}) \varepsilon_0 \sum_{\substack{i=1 \\ i \neq j}}^{k_t} \text{Im} [\psi_i(z_{j+1}) - \psi_i(z_j)] = 0, \quad j = k+1, \dots, k_t. \quad (\text{B.28})$$

Eq. (B.22) is replaced by (B.28) from which the elements of the new matrix  $\Psi_d$  follow.

Numerically  $C_{12}$  was obtained by applying a potential  $V_1 = 1$  at track 1 with  $V_2 = V_{GP} = 0$ . The free-charge  $Q_1 (> 0)$  on track 1 and induced free-charges  $Q_2 (< 0)$ , track 2) and  $Q_{GP} (< 0)$ , ground plane) were obtained by means of the method discussed at the end of the previous subsection. Then  $C_{12} = -Q_2/V_1$ .

The self-capacitance  $C_1$  showed a weak dependance on the discretization as in the case without dielectric (Table B.1). The numerical values agreed within 1.5 percent compared to the analytical value of 88.9 pF/m (see expressions (4.28) and (4.29) in the main text). Therefore, the  $C_1$ -sequence is not given.

**Table B.2.** Capacitance  $C_{12}$  for the structure of Fig. B.3 with  $\varepsilon_r = 4.7$ ; a homogeneous and nonhomogeneous discretization was used. The number of segments used in track 1 ( $k_1$ ), track 2 ( $k_2$ ), and ground plane GP ( $k_3$ ) is denoted by  $(k_1, k_2, k_3; k_t)$ , with  $k_t$  the total number of segments. The ratio of the total free-charge  $Q$  and the induced free-charge  $Q_2$  on conductor 2 is only calculated for the nonhomogeneous case.

|                        | $C_{12}$ in fF/m |                 |                  |                  |
|------------------------|------------------|-----------------|------------------|------------------|
| $(k_1, k_2, k_3; k_t)$ | (20,20,100;400)  | (20,20,200;700) | (20,20,400;1250) | (20,20,640;2000) |
| homogeneous            | 59.01            | 9.78            | 3.53             | 2.85             |
| nonhomogeneous         | 2.76             | 2.70            | 2.69             | 2.68             |
| $Q/Q_2$                | 15.1             | 4.4             | 1.4              | 0.7              |

In Table B.2 the  $C_{12}$ -sequence is given for a homogeneous discretization. The sequence converges very slowly. On physical grounds the total free-charge must be zero for this isolated system, but the numerically calculated free charge  $Q = Q_1 + Q_2 + Q_{GP} < 0$  is larger than

the machine precision; without dielectric  $Q$  was smaller than the machine precision. Also, the numerical value of  $Q$  is of the same order as the induced free-charge  $Q_2$  on conductor 2, which is used to obtain  $C_{12}$ . Since the convergence of  $C_{12}$  in Table B.2 is slow and  $Q$  is of the same order as  $Q_2$ , we changed the discretization.

On a dielectric-interface segment  $S_j \in Sd$  the normal dielectric-flux density  $D_{n,i}^j$  due to another segment  $S_i$  must be continuous. The error  $\zeta_j$  defined by

$$\zeta_j = \frac{1}{\varepsilon_0} \left| (\varepsilon_{rr,j} + \varepsilon_{rl,j}) \frac{\sigma_{Tj}}{2} l_j + (\varepsilon_{rr,j} - \varepsilon_{rl,j}) \varepsilon_0 \sum_{\substack{i=1 \\ i \neq j}}^{k_t} \int_{S_j} |E_{n,i}^j(z)| |dz| \right|, \quad (\text{B.29})$$

is a measure for the mismatch of the normal dielectric-flux density along segment  $S_j \in Sd$ ;  $E_{n,i}^j$  denotes the normal electric-field calculated by (B.14) at the dielectric-interface segment  $S_j$  due to a single-layer density along segment  $S_i$ .

The iteration procedure for the PCB problem without dielectric can be used, in which the error  $\eta_j$  over the conductor segments as well as the error  $\zeta_j$  over the dielectric-interface segments must be used. Table B.2 shows  $C_{12}$  for several segments used; the procedure converged within 6 iterations. The ratio  $Q/Q_2$  (see Table B.2) decreases and becomes less than 1 for  $k_t \approx 2000$  segments. From this ratio sequence and the  $C_{12}$ -sequence one can conclude that the error is not made in  $Q_2$ . If the error was made in  $Q_2$ , then  $Q/Q_2 \geq 1$ . Experiments showed that the largest error made is due to the insufficient approximation of the  $1/(x^2 + h_1^2)$  behavior of the charge density in the ground plane GP, rather than the edge divergence. Therefore,  $C_{12}$  converges to the exact value. Note that approx.  $k_t = 400$  segments suffice for practical accuracy.

To get a reasonably accurate value of  $C_{12}$ , the total number of segments,  $k_t$ , must be impractically large for a homogeneous discretization. The nonhomogeneous case needs much less segments. Therefore, the memory requirement is much less demanding for the latter case: 2000 segments stored in double precision use approximately 30 MB, whereas 400 segments need only approximately 1 MB. The nonhomogeneous-discretization algorithm can also be used on ‘simple’ computers such as a PC. The process saves memory of the computer, rather than CPU time.

The numerical values clearly show the importance of the discretization on the small coupling capacitance. When both tracks are on the same side the capacitive coupling is of the order pF/m. Also, when the cabinet panel (CP) is present (see Fig. 3.4 main text), the capacitive coupling from a track to CP is again of the order pF/m. Numerical experiments showed that for such ‘large’ values a homogeneous discretization is allowed.

#### B.4 Numerical and approximate analytical solution

Consider the PCB structure shown in Fig. B.3. The parameters used were again  $2w = 10$  cm,  $b = 1.5$  mm,  $h_1 = h_2 = 1.5$  mm, and  $\varepsilon_r = 4.7$ .

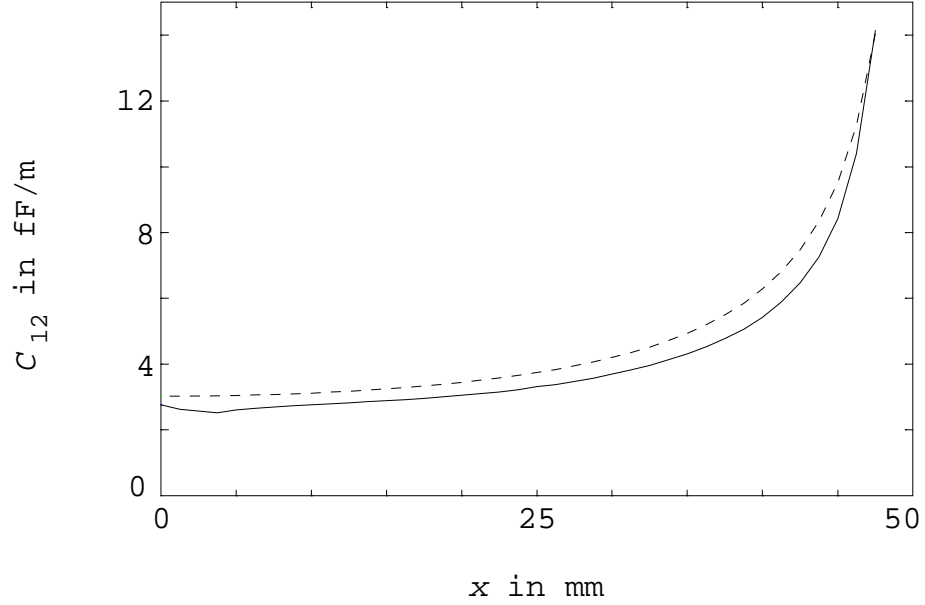


**Figure B.4.** Numerically (—) calculated coupling-capacitance  $C_{12}(x)$  of track 1 to track 2 in Fig. B.3. Track 1 was fixed at  $x = 0$  while the positioning of track 2 was varied. Curve (- - -) shows the analytical approximation (4.36) given in the main text.

Figure B.4 shows the numerically calculated  $C_{12}(x)$  with track 1 fixed at  $x = 0$  and the positioning of track 2 varied. In this configuration the capacitance involved has the lowest value. The analytical approximation (4.36) given in the main text is shown by curve (- - -). Both agree within 20 percent.

# Appendix C

## Fourier-transformation techniques

The derivation of the current distribution in a plane and a plate of infinite extent due to a wire above that plane or plate is given in Sections C.1 and C.2 by means of Fourier-transformation techniques. The results are discussed in Sections 4.2 and 4.3 of the main text. Section C.3 gives the current-distribution solution for a thin wire between two wide plates and is further discussed in Section 4.5.

### C.1 Carson's approach

A filamentary wire 1 is positioned at  $x = 0$  in a dielectric region at the height  $h_1$  above conductive ground which fills the lower halfspace  $y < 0$  (Fig. 4.6a). The wire carries a current wave  $I_1$  propagating as  $e^{j\omega t - \gamma|z|}$  in the positive  $z$ -direction. The propagation constant  $\gamma$  is taken small, as well as the displacement current in the ground. Then the equation

$$\nabla^2 E_z = j\omega\mu\sigma E_z \quad (\text{C.1})$$

holds for time-harmonic fields in the GP. Under the assumptions mentioned, Carson's solution [Car26] of Eq. (C.1) is the Fourier cosine integral with respect to  $x$

$$E_z(x, y) = - \int_0^\infty F(\alpha) \cos(\alpha x) e^{y\sqrt{\alpha^2 + j\omega\mu\sigma}} d\alpha. \quad (\text{C.2})$$

The  $x$  and  $y$ -components of the magnetic field  $\mathbf{H}$  in the ground stem from Maxwell's equation  $\nabla \times \mathbf{E} = -j\omega\mu\mathbf{H}$ , in which  $\mu = \mu_0\mu_r$ . Above ground the current  $I_1$  produces the familiar  $r^{-1}$ -field  $\mathbf{H}_1$  and the current distribution  $J_z(x, y) = \sigma E_z(x, y)$  produces a magnetic field  $\mathbf{H}_2$  with transverse components only. We expand both magnetic fields in Fourier cosine integrals ( $x$ -components) and Fourier sine integrals ( $y$ -components):

$$\begin{aligned} H_{1x} &= \frac{I_1}{2\pi} \frac{h_1 - y}{x^2 + (h_1 - y)^2} \\ &= \frac{I_1}{2\pi} \int_0^\infty \cos(\alpha x) e^{-\alpha(h_1 - y)} d\alpha, \\ H_{1y} &= \frac{I_1}{2\pi} \frac{x}{x^2 + (h_1 - y)^2} \\ &= \frac{I_1}{2\pi} \int_0^\infty \sin(\alpha x) e^{-\alpha(h_1 - y)} d\alpha, \end{aligned} \quad (\text{C.3})$$

$$\begin{aligned}
H_{2x} &= + \int_0^\infty [\phi(\alpha) + \frac{I_1}{2\pi} e^{-\alpha h_1}] \cos(\alpha x) e^{-\alpha y} d\alpha, \\
H_{2y} &= - \int_0^\infty [\phi(\alpha) + \frac{I_1}{2\pi} e^{-\alpha h_1}] \sin(\alpha x) e^{-\alpha y} d\alpha.
\end{aligned} \tag{C.4}$$

In these Fourier integrals the values of  $y$  are restricted to negative values for the argument of the exponent, i.e.  $y < h_1$  in Eq. (C.3) and  $y > 0$  in Eq. (C.4). The second term between the square brackets in Eq. (C.4) represents the image current at  $y = -h_1$  which has been added for convenience. The boundary conditions for the magnetic fields and inductions at the plane  $y = 0$  yields a linear system of equations, from which the unknown quantities  $F(\alpha)$  and  $\phi(\alpha)$  can be determined. The current distribution  $J_z(x, y)$  in the GP becomes

$$J_z(x, y) = -\frac{j\omega\mu\sigma I_1}{\pi} \int_0^\infty \frac{\cos \alpha x}{\alpha\mu_r + \sqrt{\alpha^2 + j\omega\mu\sigma}} e^{-\alpha h_1} e^{y\sqrt{\alpha^2 + j\omega\mu\sigma}} d\alpha. \tag{C.5}$$

For nonmagnetic materials ( $\mu_r = 1$ ) the integral Eq. (C.5) is the same as given by Carson [Car26].

## C.2 Ground plane of finite thickness

The GP is now a plate at  $-d < y < 0$ , still of infinite extent in the  $x$ -direction (Fig. 4.6b). Develop the electric field  $E_z$  in the GP in a Fourier cosine integral with respect to  $x$

$$E_z(x, y) = - \int_0^\infty \left[ F_+(\alpha) e^{y\sqrt{\alpha^2 + j\omega\mu\sigma}} + F_-(\alpha) e^{-y\sqrt{\alpha^2 + j\omega\mu\sigma}} \right] \cos(\alpha x) d\alpha. \tag{C.6}$$

The expression for the magnetic fields  $\mathbf{H}_1$  and  $\mathbf{H}_2$  above the GP remains as above. The magnetic field  $\mathbf{H}$  in the GP again stems from the Maxwell equation  $\nabla \times \mathbf{E} = -j\omega\mu\mathbf{H}$ . Below the GP we have to allow a magnetic field  $\mathbf{H}_3$  which satisfies Laplace's equation:

$$\begin{aligned}
H_{3x} &= \int_0^\infty \psi(\alpha) \cos(\alpha x) e^{\alpha y} d\alpha, \\
H_{3y} &= \int_0^\infty \psi(\alpha) \sin(\alpha x) e^{\alpha y} d\alpha.
\end{aligned} \tag{C.7}$$

The Fourier transforms of all these fields together with the boundary conditions at  $y = 0$  and  $y = -d$  yield a set of linear equations, from which  $F_+(\alpha)$ ,  $F_-(\alpha)$ ,  $\phi(\alpha)$  and  $\psi(\alpha)$  are determined. We have

$$F_+(\alpha) = + \frac{j\omega\mu I_1}{\pi} \frac{(\alpha\mu_r + \xi) e^{-\alpha h_1}}{D} \tag{C.8}$$

$$F_-(\alpha) = - \frac{j\omega\mu I_1}{\pi} \frac{(\alpha\mu_r - \xi) e^{-\alpha h_1 - 2d\xi}}{D} \tag{C.9}$$

$$\phi(\alpha) = - \frac{I_1}{\pi} \frac{\alpha\mu_r e^{-\alpha h_1} \{(\alpha\mu_r + \xi) - (\alpha\mu_r - \xi) e^{-2d\xi}\}}{D} \tag{C.10}$$

$$\psi(\alpha) = + \frac{I_1}{\pi} \frac{2\alpha\mu_r \xi e^{\alpha(d-h_1)-d\xi}}{D} \tag{C.11}$$

$$D = (\alpha\mu_r + \xi)^2 - (\alpha\mu_r - \xi)^2 e^{-2d\xi} \tag{C.12}$$

with  $\xi = \sqrt{\alpha^2 + j\omega\mu\sigma}$ . The current distribution in the GP becomes

$$\begin{aligned} J_z(x, y) &= \sigma E_z(x, y) \\ &= -\frac{j2\omega\mu\sigma I_1}{\pi} \int_0^\infty \frac{\alpha\mu_r \sinh[(d+y)\xi] + \xi \cosh[(d+y)\xi]}{(\alpha\mu_r + \xi)^2 - (\alpha\mu_r - \xi)^2 e^{-2d\xi}} \cos(\alpha x) e^{-(\alpha h_1 + d\xi)} d\alpha. \end{aligned} \quad (\text{C.13})$$

In the limiting case  $d \rightarrow \infty$ , this equation reduces to Eq. (C.5) as it should. In the ‘thin-plate limit’ we let  $d \downarrow 0$  while keeping the sheet resistance  $R_\square = 1/\sigma d$  constant. The resulting sheet current density is Eq. (4.10). The  $Z_t$  between the injection wire and a sensing wire can be calculated according to Eq. (4.1) from the flux  $\Phi(x)$  between the GP and the sensing wire and the electric field at the surface  $E_z = J_z/\sigma$  close to the sensing wire; see Fig. 4.2. It is more convenient to introduce a flux function or vector potential  $A_z$ . We choose to write the electric field  $E_z(x, y)$  in the material as  $-j\omega A_z(x, y)$  and require that  $A_z$  also correctly describes the magnetic field outside the GP:

$$A_z(x, y) = A_z^{dp}(x, y) + \mu_0 \int_0^\infty \cos(\alpha x) \frac{\phi(\alpha)}{-\alpha} e^{-\alpha y} d\alpha \quad (y > 0) \quad (\text{C.14})$$

with

$$A_z^{dp} = -\frac{\mu_0 I_1}{4\pi} \ln \frac{x^2 + (y - h_1)^2}{x^2 + (y + h_1)^2} \quad (\text{C.15})$$

and

$$A_z(x, y) = \mu_0 \int_0^\infty \cos(\alpha x) \frac{\psi(\alpha)}{\alpha} e^{+\alpha y} d\alpha. \quad (y < 0) \quad (\text{C.16})$$

The  $A_z^{dp}$  is the vector potential for a dipole of two line currents  $\pm I_1$  placed at  $y = \pm h_1$ . Because of the applied boundary conditions for the magnetic fields,  $A_z$  is continuous at both surfaces of the GP. Because of the exponentials in  $y$  in Eqs. (C.14) and (C.16), the vector potential vanishes at large distances; the current  $I_1$  fully returns through the GP. For  $Z_t$  we rewrite Eq. (4.1) as:

$$Z_t = j\omega A_z(x_s, y_s)/I_1 \quad (\text{C.17})$$

where  $(x_s, y_s)$  is the position of the sensing wire. In the thin-plate limit the integrals in Eqs. (C.14) and (C.16) reduce both to

$$\int_0^\infty \frac{\cos(\alpha x) e^{-\alpha h_t}}{\alpha + j\beta} d\alpha = -\frac{e^{j\beta h_t}}{2} \left[ e^{\beta x} \text{Ei}(-\beta x - j\beta h_t) + e^{-\beta x} \text{Ei}(\beta x - j\beta h_t) \right], \quad (\text{C.18})$$

where  $\beta = \mu_0\omega/2R_\square$ , Ei the exponential integral (see e.g. [Abr70]), and  $h_t = h_1 + h_2$ ,  $h_2$  the distance between sensing wire and GP; this  $h_t$  should be used when wire 1 and 2 are on the same side as well as on opposite sides. Bergervoet [Ber95] obtained a similar result by a different method based on the method of moving images developed by Maxwell [Max00]. The line dipole Eq. (C.15) explains why the current density is sensed more directly by a wire at the opposite side of the GP. This is also shown by the field plots in Fig. 4.4.

### C.3 Injection wire between two plates

Suppose injection wire 1 is placed between two plates which are located at  $y = \pm h_{PP}$  and which have a thickness  $d$ . Here we proceed via the vector potential as described in the

previous section. The Fourier coefficients for  $A_z$  are between both plates ( $-h_{PP} < y < h_{PP}$  and  $\mu_r = 1$ )

$$A_z(\alpha) = \frac{\mu_0}{\alpha} [\phi_+(\alpha) e^{\alpha y} + \phi_-(\alpha) e^{-\alpha y}], \quad (\text{C.19})$$

outside both plates

$$A_z(\alpha) = \begin{cases} \frac{\mu_0}{\alpha} \psi_-(\alpha) e^{-\alpha y} & y > h_{PP} + d \\ \frac{\mu_0}{\alpha} \psi_+(\alpha) e^{\alpha y} & y < -(h_{PP} + d) \end{cases} \quad (\text{C.20})$$

and inside both plates

$$A_z(\alpha) = \mu_0 [F_{i+}(\alpha) e^{y\xi} + F_{i-}(\alpha) e^{-y\xi}] \quad (\text{C.21})$$

with  $\xi = \sqrt{\alpha^2 + j\omega\mu_0\sigma}$  and  $i = 1, 2$  for the upper and lower plate respectively. The source term due to the current  $I_1$  through wire 1 at  $(0, y_1)$  is

$$\frac{\mu_0 I_1}{2\pi\alpha} e^{-\alpha|y-y_1|}. \quad (\text{C.22})$$

Continuity of  $A_z$  and  $\partial A_z / \partial y$  at the four surfaces  $y = \pm h_{PP}$  and  $y = \pm(h_{PP} + d)$  results in a set of equations. Of special interest are the solutions in the case where wire 1 is in the middle between the plates ( $y_1 = 0$ ):

$$F_{1+}(\alpha) = F_{2-}(\alpha) = -\frac{I_1}{\pi} \frac{(\alpha - \xi) e^{h_{PP}(\alpha - \xi)}}{D(\alpha)} \quad (\text{C.23})$$

$$F_{2+}(\alpha) = F_{1-}(\alpha) = +\frac{I_1}{\pi} \frac{(\alpha + \xi) e^{h_{PP}(\alpha + \xi) + 2d\xi}}{D(\alpha)} \quad (\text{C.24})$$

$$\psi_+(\alpha) = \psi_-(\alpha) = \frac{I_1}{\pi} \frac{2\alpha\xi e^{\alpha(2h_{PP}+d)+d\xi}}{D(\alpha)} \quad (\text{C.25})$$

$$\phi_+(\alpha) = \phi_-(\alpha) = \frac{-j\omega\mu_0\sigma (e^{2d\xi} - 1)}{D(\alpha)} \quad (\text{C.26})$$

$$D(\alpha) = e^{2\alpha h_{PP}} [e^{2d\xi} (\alpha + \xi)^2 - (\alpha - \xi)^2] + j\omega\mu_0\sigma (e^{2d\xi} - 1). \quad (\text{C.27})$$

For the  $Z_t$  at  $(x_s, y_s)$  above the top plate ( $y_s \geq h_{PP} + d$ ) we obtain

$$Z_t(x_s, y_s) = \frac{2j\omega\mu_0}{\pi} \int_0^\infty \frac{\cos(\alpha x_s) e^{\alpha(2h_{PP}+d-y_s)+d\xi}}{D(\alpha)} d\alpha. \quad (\text{C.28})$$

# Appendix D

## Method of Moments

A current  $I_1$  flowing in the positive  $z$ -direction through a filamentary wire at  $\mathbf{r}_1 = (x_1, h_1)$  (Fig. 4.6c) generates the vector potential at  $\mathbf{r} = (x, y)$

$$A_z^{(1)}(\mathbf{r}) = -\frac{\mu_0 I_1}{2\pi} \ln |\mathbf{r} - \mathbf{r}_1|. \quad (\text{D.1})$$

The  $K_z(x)$  through the strip causes the potential

$$A_z^{(s)}(\mathbf{r}) = -\frac{\mu_0}{2\pi} \int_{-w}^w K_z(x') \ln |\mathbf{r} - \mathbf{r}'| dx', \quad (\text{D.2})$$

with  $\mathbf{r}' = (x', 0)$  on the strip. The electric field is given by  $E_z(\mathbf{r}) = -j\omega(A_z^{(1)}(\mathbf{r}) + A_z^{(s)}(\mathbf{r})) - \nabla_z V(\mathbf{r})$ . The condition at the strip

$$E_z(x, 0) = K_z(x) R_\square \quad (\text{D.3})$$

results in a Fredholm integral equation of the second kind

$$K_z(x) - \lambda_f \int_{-w}^w K_z(x') \ln |x - x'| dx' = f(x) + c, \quad -w \leq x \leq w, \quad (\text{D.4})$$

where  $\lambda_f = j\omega\mu_0/2\pi R_\square$ ,  $c = -\nabla_z V/R_\square$  and

$$f(x) = -j\omega A_z^{(1)}(x, 0)/R_\square \quad (\text{D.5})$$

the excitation function due to the wire. The width of the GP is here finite, in contrast to Appendix C. Consequently the current through the GP is smaller than  $-I_1$  when  $c = 0$ . The constraint

$$\int_{-w}^w K_z(x) dx = -I_1 \quad (\text{D.6})$$

requires that some  $K_z$  should be added which is a solution of Eq. (D.4) with  $f(x) = 0$ . For an isolated PCB, reciprocity of  $Z_t$  can be applied to show that  $c = -Z_t(1\text{-CM})I_1/R_\square$ , in which  $Z_t(1\text{-CM})$  is the transfer impedance between the DM circuit of wire 1 and GP on one hand and the CM circuit formed by the GP and a far away CP on the other hand. Because the reference position  $x^*$  on the GP in Eq. (4.16) is chosen arbitrarily,  $E_z + j\omega(A_z^{(s)} + A_z^{(1)})$  is constant over the GP in the  $x$ -direction, as is  $\nabla_z V$ . When the difference of Eq. (D.4) is taken for two positions  $x$  and  $x^*$  on the GP,  $c$  is eliminated.



The CM current distribution is a solution of Eqs. (D.4) and (D.6) with  $f(x) = 0$ . A comparison with Eq. (A.22) shows that  $c$  is then equal to  $-I_1 [1/2w + (j\omega\mu_0/2\pi R_\square) \ln(2/w)]$

Similar to Eq. (C.17) we can rewrite the  $Z_t$  in Eq. (4.1) to

$$Z_t = [j\omega A_z(x_s, y_s) - cR_\square] / I_1 \quad (\text{D.7})$$

where  $A_z = A_z^{(s)} + A_z^{(1)}$  is the total vector potential taken at the sensing wire at  $(x_s, y_s)$ .

Equation (D.4) with constraint Eq. (D.6) can also be solved analytically by expanding  $K_z(x)$  and  $f(x)$  in a series of Chebyshev polynomials [But80]. The coefficients of the  $f(x)$  are difficult to obtain, and closed-form expressions have only been found when the injection wire resides at the middle position of the strip. The off-diagonal elements in the resulting infinite matrix decrease slowly with the distance from the diagonal. The solution still requires numerical inversion and truncation of the matrix.

## Bibliography

- [Abr70] M. Abramowitz and I. A. Stegun, Eds., *Handbook of Mathematical Functions*, 9th printing, New York: Dover, 1970.
- [And67] R. W. Anderson, "S-parameter techniques for faster, more accurate network design," *Hewlett-Packard J.*, vol. 18, no. 3, Feb. 1967.
- [Atk97] K. E. Atkinson, *The Numerical Solution of Integral Equations of the Second Kind*, Cambridge: Cambridge University Press, 1997.
- [Bal81] E. Ball and J. A. Staniforth, "Transfer impedance between circular coils separated by thick nonferrous metal sheets," *IEE Proc. A*, vol. 128, no. 1, pp. 64-67, Jan. 1981.
- [Bal97] C. A. Balanis, *Antenna Theory: Analysis and Design*, 2nd ed., New York: Wiley, 1997.
- [Bau78] C. E. Baum, T. K. Liu, and F. M. Tesche, *On the Analysis of General Multiconductor Transmission-Line Networks*, Kirtland AFB, NM: Air Force Weapons Laboratory, 1978, Interaction Note 350.
- [Ber83] R. Bersier and B. Szentkuti, "Rationale and new experimental evidence on the adequacy of conducted instead of radiated susceptibility tests," in *Proc. 5th Int. Symp. Electromagn. Compat.* (Zürich, Switzerland), March 1983, pp. 257-262.
- [Ber94] J. R. Bergervoet, "EMC measurements and models connecting the system level with the module level," *Philips J. Res.*, vol. 48, no's 1-2, pp. 63-81, Jan. 1994.
- [Ber95] J. R. Bergervoet, private communication, March 1995.
- [Ber96] J. R. Bergervoet, private communication, April 1996.
- [Ber97] J. R. Bergervoet, G. P. J. F. M. Maas, and M. J. C. M. van Doorn, "The common-mode skeleton model for assessment of electromagnetic compatibility at the system level," in *Proc. 12th Int. Symp. Electromagn. Compat.* (Zürich, Switzerland), Feb. 1997, pp. 657-662.
- [But80] C. M. Butler and D. R. Wilton, "General analysis of narrow strips and slots," *IEEE Trans. Antennas Propagat.*, vol. AP-28, no. 1, pp. 42-48, Jan. 1980.
- [Bla85] J. van Bladel, *Electromagnetic Fields*, revised printing, Bristol: Hemisphere, 1985.
- [Can96] V. Caniggia, V. Costa, and L. Vitucci, "Investigation of EMI on multilayer printed circuit boards: Radiated emissions," in *Proc. 1996 IEEE Int. Symp. Electromagn. Compat.* (Santa Clara, CA, USA), Aug. 1996, pp. 316-321.
- [Car26] J. R. Carson, "Wave propagation in overhead wires with ground return," *Bell Syst. Tech. J.*, vol. 5, pp. 539-554, 1926.
- [Car96] N. J. Carter and E. G. Stevens, "Bulk current injection (BCI): its past, present and future (?) in aerospace," in *IEE Colloquium on EMC testing for conducted mechanisms* (London, UK), Digist Ref. No. 1996/116, May 1996, pp. 2/1-2/12.
- [Cer93] G. Cerri, R. De Leo, V. M. Primiani, and A. Schiavoni, "Investigation of ground plane current distribution," in *Proc. 10th Int. Symp. Electromagn. Compat.* (Zürich, Switzerland), March 1993, pp. 195-200.
- [Clo94] R. du Cloux, G. P. J. F. M. Maas, and A. J. H. Wachtters, "Quasi-static boundary element method for electromagnetic simulation of PCBS," *Philips J. Res.*, vol. 48, no's 1-2, pp. 117-144, Jan. 1994.
- [Coe94] M. J. Coenen, "EMC workbench: Testing methodology, module level testing and standardization," *Philips J. Res.*, vol. 48, no's 1-2, pp. 83-116, Jan. 1994.

- [Coe96] M. Coenen, "Optimising IC decoupling, for performance and EMI levels," *Electronic Prod. Des.*, vol. 17, no. 1, pp. 26, 29-30, 33-34, Jan. 1996.
- [Col91] R. E. Collin, *Field Theory of Guided Waves*, 2nd ed., New York: IEEE, 1991.
- [Col92] R. E. Collin, *Foundations for Microwave Engineering*, 2nd ed., New York: McGraw-Hill, 1992.
- [Dav95] B. Davari, R. H. Dennard, and G. G. Shahidi, "CMOS Scaling for high performance and low power – The next ten years," *Proc. IEEE*, vol. 83, no. 4, pp. 595-606, April 1995.
- [Dem92] B. Demoulin, L. Klone, M. Boucheteau, and P. Degauque, "Measurement of transfer impedance of coaxial and multiwire shielded cables: A review of the recent developments," in *11th Int. Wroclaw Symp. Electromagn. Compat.* (Wroclaw, Poland), Sept. 1992, pp. 489-492.
- [Djo86] A. R. Djordjević, T. K. Sarkar, and R. F. Harrington, "Analysis of lossy transmission lines with arbitrary nonlinear terminal networks," *IEEE Trans. Microwave Theory Tech.*, vol. MTT-34, no. 6, pp. 660-666, June 1986.
- [Djo87a] A. R. Djordjević, T. K. Sarkar, and R. F. Harrington, "Time-domain response of multiconductor transmission lines," *Proc. IEEE*, vol. 75, no. 6, pp. 743-764, June 1987.
- [Djo87b] A. R. Djordjević and T. K. Sarkar, "Analysis of time response of lossy multiconductor transmission line networks," *IEEE Trans. Microwave Theory Tech.*, vol. MTT-35, no. 10, pp. 898-907, Oct. 1987.
- [Djo93] A. R. Djordjević and T. K. Sarkar, "An investigation of delta- $I$  noise on integrated circuits," *IEEE Trans. Electromagn. Compat.*, vol. EMC-35, no. 2, pp. 134-147, May 1993.
- [Djo94] A. R. Djordjević and T. K. Sarkar, "Closed-form formulas for frequency-dependent resistance and inductance per unit length of microstrip and strip transmission lines," *IEEE Trans. Microwave Theory Tech.*, vol. MTT-42, no. 2, pp. 241-248, Feb. 1994.
- [Doc93] R. W. Dockey and R. F. German, "New techniques for reducing printed circuit board common-mode radiation," in *Proc. 1993 IEEE Int. Symp. Electromagn. Compat.* (Dallas, TX, USA), Aug. 1993, pp. 334-339.
- [Don72] N. A. McDonald, "Electric and magnetic coupling through small apertures in shield walls of any thickness," *IEEE Trans. Microwave Theory Tech.*, vol. MTT-20, no. 10, pp. 689-695, Oct. 1972.
- [Dun90] S. Dunwoody and E. VanderHeyden, "Transfer impedance testing of multi-conductor shielded connectors," in *Proc. 1990 IEEE Int. Symp. Electromagn. Compat.* (Washington, DC, USA), Aug. 1990, pp. 581-585.
- [EEC89] EEC, "European Directive on EMC: 89/336/EEC of 3 May 1989," *Official EC Journal*, May 1989.
- [Eft78] A. E. Efthymiadis and L. M. Wedepohl, "Propagation characteristics of infinitely-long single-conductor lines by the complete field solution method," *Proc. Inst. Electr. Eng.*, vol. 125, no. 6, pp. 511-517, June 1978.
- [Eic85] B. Eicher and C. Stäger, "Extremely broadband RF-connector and cable screening measurements (up to 150 dB screening attenuation) for frequencies of 1 kHz to 10 GHz," in *Proc. 15th European Microwave Conf.* (Paris, France), Sept. 1985, pp. 887-894.
- [Eic92] B. Eicher and L. Boillot, "Very low frequency to 40 GHz screening measurements on cables and connectors; line injection method and mode stirred chamber," in *Proc. 1992 IEEE Int. Symp. Electromagn. Compat.* (Anaheim, CA, USA), Aug. 1992, pp. 302-307.
- [Far90a] R. Faraji-Dana and Y. L. Chow, "Edge condition of the field and a.c. resistance of a rectangular strip conductor," *IEE Proc. H*, vol. 137, no. 2, pp. 133-140, Apr. 1990.
- [Far90b] R. Faraji-Dana and Y. L. Chow, "The current distribution and ac resistance of a microstrip structure," *IEEE Trans Microwave Theory Tech.*, vol. MTT-38, no. 9, pp. 1268-1277, Sept. 1990.
- [Far91] R. Faraji-Dana and Y. L. Chow, "AC resistance of two coupled strip conductors," *IEE Proc. H*, vol. 138, no. 1, pp. 37-45, Feb. 1991.
- [Fow75] E. P. Fowler, "Screened coaxial connectors for high sensitivity systems," in *Proc. IEEE (region 8) Symp. Electromagn. Compat.* (Montreux, France), May 1975, pp. 291-296.
- [Fow92] E. P. Fowler, "Cables and connectors – Their contribution to electromagnetic compatibility," in *Proc. 1992 IEEE Int. Symp. Electromagn. Compat.* (Anaheim, CA, USA), Aug. 1992, pp. 329-333.

- [Fow94] E. P. Fowler, "Screening of cables and connectors," *Electron. Commun. Eng. J.*, vol. 6, pp. 93-102, April 1994.
- [Fra94] J. Franz and W. John, "An approach to determine decoupling effects of VCC and VGG structures in multilayer technique," in *1994 Int. Symp. Electromagn. Compat.* (Sendai, Japan), May 1994, pp. 56-59.
- [Gar97] J. Garrett, A. Ruehli, and C. Paul, "Recent improvements in PEEC modeling accuracy," in *Proc. 1997 IEEE Int. Symp. Electromagn. Compat.* (Austin, TX, USA), Aug. 1997, pp. 347-352.
- [Goe92] J. Goedbloed, *Electromagnetic Compatibility*, London: Prentice Hall, 1992.
- [Gra67] I. S. Gradshteyn and I. M. Ryzhik, *Table of Integrals, Series and Products*, New York: Academic Press, 1967.
- [Gra92] L. B. Gravelle and P. F. Wilson, "EMI/EMC in printed circuit boards – A literature review," *IEEE Trans. Electromagn. Compat.*, vol. EMC-34, no. 2, pp. 109-116, May 1992.
- [Gre90] H. E. Green and J. D. Cashman, "The transmission line antenna revisited," *IEEE Trans. Antennas Propagat.*, vol. AP-38, no. 4, pp. 575-578, April 1990.
- [Gup96] K. C. Gupta, R. Garg, I. Bahl, and P. Bhartia, *Microstrip Lines and Slotlines*, 2nd ed., Norwood, MA: Artech House, 1996.
- [Hal73] L. Halme and J. Annanpalo, "Use of magnetic materials for improvement of screening properties of different types of cables," in *Proc. 1973 IEEE Int. Symp. Electromagn. Compat.* (New York, N.Y., USA), June 1973, pp. 340-357.
- [Hal88] L. Halme and B. Szentkuti, "The background of electromagnetic screening measurements of cylindrical screens," *Technische Mitt. PTT*, no. 3, pp. 105-115, 1988.
- [Hal92] L. Halme, "Development of IEC cable shielding effectiveness standards," in *Proc. 1992 IEEE Int. Symp. Electromagn. Compat.* (Anaheim, CA, USA), Aug. 1992, pp. 321-328.
- [Har69] R. F. Harrington, K. Pontoppidan, P. Abrahamsen, and N. C. Albertsen, "Computation of laplacian potentials by an equivalent source method," *Proc. Inst. Electr. Eng.*, vol. 116, no. 10, pp. 1715-1720, Oct. 1969.
- [Har93] R. F. Harrington, *Field Computation by Moment Methods*, New York: IEEE, 1993.
- [Hel95] M. J. A. M. van Helvoort, *Grounding Structures for the EMC-Protection of Cabling and Wiring*, Ph. D. thesis Eindhoven University of Technology, 1995.
- [Hen91] R. Henke and D. Ohnstad, "A checklist for EMC-controlled printed circuit board designs: A checklist aids parties involved in the design process to learn from previous problems," *Printed Circuit Design*, vol. 8, no. 2, pp. 25-31, 34-35, Feb. 1991.
- [Hil96] D. A. Hill, D. G. Camell, K. H. Cavcey, and G. H. Koepke, "Radiated emissions and immunity of microstrip transmission lines: Theory and reverberation," *IEEE Trans. Electromagn. Compat.*, vol. EMC-38, no. 2, pp. 165-172, May 1996.
- [Hoc96] D. M. Hockanson, J. L. Drewniak, T. H. Hubing, T. P. Van Doren, F. Sha, and M. J. Wilhelm, "Investigation of fundamental EMI source mechanisms driving common-mode radiation from printed circuit boards with attached cables," *IEEE Trans. Electromagn. Compat.*, Vol. EMC-38, no. 4, pp. 557-566, Nov. 1996.
- [Hoc97] D. M. Hockanson, J. L. Drewniak, T. H. Hubing, T. P. Van Doren, F. Sha, C.-W. Lam, and L. Rubin, "Quantifying EMI resulting from finite-impedance reference planes," *IEEE Trans. Electromagn. Compat.*, vol. EMC-39, no. 4, pp. 286-297, Nov. 1997.
- [Hoe88] L. O. Hoeft and J. S. Hofstra, "Measured electromagnetic shielding performance of commonly used cables and connectors," *IEEE Trans. Electromagn. Compat.*, vol. EMC-35, no. 3, pp. 260-275, Aug. 1988.
- [Hoe91] L. O. Hoeft and J. S. Hofstra, "Electromagnetic shielding provided by selected DB-25 subminiature connectors," in *Proc. 1991 IEEE Int. Symp. Electromagn. Compat.* (Cherry Hill, NJ, USA), Aug. 1991, pp. 50-53.
- [Hoe92] L. O. Hoeft and J. S. Hofstra, "Measurement of surface transfer impedance of multi-wire cables, connectors and cable assemblies," in *Proc. 1992 IEEE Int. Symp. Electromagn. Compat.* (Anaheim, CA, USA), Aug. 1992, pp. 308-314.

- [Hor96a] F. B. M. van Horck, A. P. J. van Deursen, and P. C. T. van der Laan, *Coupling on a Multilayer Printed Circuit Board and the Current Distribution in the Ground Plane*, Eindhoven: Faculty of Electrical Engineering, Eindhoven University of Technology, 1996. EUT Report 96-E-300.
- [Hor96b] F. B. M. van Horck, A. P. J. van Deursen, and P. C. T. van der Laan, "Coupling effects on a multilayer printed circuit board," in *Proc. EMC'96 Roma* (Rome, Italy), vol. 2, Sept. 1996, pp. 596-601.
- [Hor96c] F. B. M. van Horck, A. P. J. van Deursen, P. C. T. van der Laan, and B. L. F. Paagman, "Simple measurement of the transfer impedance of a connector," in *Proc. EMC'96 Roma Int. Symp. Electromagn. Compat.* (Rome, Italy), vol. 2, Sept. 1996, pp. 733-737.
- [Hor97a] F. B. M. van Horck and A. P. J. van Deursen, *Prediction of Common Mode Currents on Cables Connected to a Multilayer Printed Circuit Board and Couplings on the Board*, Eindhoven: Faculty of Electrical Engineering, Eindhoven University of Technology, 1997. EUT Report 97-E-305.
- [Hor97b] F. B. M. van Horck, A. P. J. van Deursen, and P. C. T. van der Laan, "Prediction of common-mode currents through cables connected to a multilayer printed circuit board," in *Proc. Int. Conf. Electromagnetics for Advanced Applications (ICEAA)* (Torino, Italy), Sept. 1997, pp. 243-246.
- [Hor97c] F. B. M. van Horck, A. P. J. van Deursen, and P. C. T. van der Laan, "Prediction of common-mode currents on cables connected to a multilayer printed circuit board," in *Proc. ProRISC Workshop on Circuits, Systems and Signal Processing* (Mierlo, Netherlands), Nov. 1997, pp. 223-230.
- [Hou89] M. A. van Houten, E. J. M. van Heesch, A. P. J. van Deursen, R. G. Noij, J. N. A. M. van Rooy, and P. C. T. van der Laan, "General Methods for the Protection of Electronic Equipment against Interference, tested in High-Voltage Substations," in *Proc. 8th Int. Symp. on Electromagn. Compat.* (Zürich, Switzerland), March 1989, pp. 429-434.
- [Hou90] M. A. van Houten, *Electromagnetic Compatibility in High-Voltage Engineering*, Ph. D. thesis Eindhoven University of Technology, 1990.
- [Hub94] T. H. Hubing, T. P. Van Doren, and J. L. Drewniak, "Identifying and quantifying printed board inductance," in *Proc. 1994 IEEE Int. Symp. Electromagn. Compat.* (Chicago, IL, USA), Aug. 1994, pp. 205-208.
- [Hub95] T. H. Hubing, J. L. Drewniak, T. P. Van Doren, and D. M. Hockanson, "Power bus decoupling on multilayer printed circuit boards," *IEEE Trans. Electromagn. Compat.*, vol. EMC-37, no. 2, pp. 155-166, May 1995.
- [IEC90] IEC, *International Electrotechnical Vocabulary (IEV) – Chapter 161: Electromagnetic Compatibility*, IEC 60050(161), 1990.
- [Jas77] M. A. Jaswon and G. T. Symm, *Integral Equation Methods in Potential Theory and Elastostatics*, London: Academic press, 1977.
- [Kad59] H. Kaden, *Wirbelströme und Schirmung in der Nachrichtentechnik*, 2nd ed., Berlin: Springer, 1959.
- [Kam88] Y. Kami and R. Sato, "Analysis of radiation characteristics of a finite-length transmission line using a circuit-concept approach," *IEEE Trans. Electromagn. Compat.*, vol. EMC-30, no. 2, pp. 114-121, May 1988.
- [Kas94] T. Kasdepke and J. K. ter Haseborg, "Multiconductor transmission line theory for shielded cables under consideration of the environment," *Proc. EMC'94 Roma Int. Symp. Electromagn. Compat.* (Rome, Italy), vol. 1, Sept. 1994, pp. 257-262.
- [Kas96] T. Kasdepke and J. K. ter Haseborg, "The influence of the line parameters on the coupling to shielded multiconductor transmission lines," in *Proc. EMC'96 Roma Int. Symp. Electromagn. Compat.* (Rome, Italy), vol. 2, Sept. 1996, pp. 538-543.
- [Kob57] H. Kober, *Dictionary of Conformal Representations*, 2nd ed., New York: Dover, 1957.
- [Kue80] E. F. Kuester and D. C. Chang, "Closed-form expressions for the current or charge distribution on parallel strips or microstrip," *IEEE Trans. Microwave Theory Tech.*, vol. MTT-28, no. 3, pp. 254-259, March 1980.
- [Laa84] P. C. T. van der Laan, W. J. L. Jansen, and E. F. Steennis, "Design of shielded enclosures, in particular for high-voltage laboratories," *Kema Sci. Tech. Rep.*, vol. 2, no. 11, pp. 101-111, 1984.
- [Laa87] P. C. T. van der Laan, M. A. van Houten, and A. P. J. van Deursen, "Grounding philosophy," in *Proc. 7th Int. Symp. Electromagn. Compat.* (Zürich, Switzerland), March 1987, pp. 567-572.

- [Laa93] P. C. T. van der Laan, M. J. A. M. van Helvoort, and A. P. J. van Deursen, "New developments in grounding structures for the protection of micro-electronics," in *Proc. 10th Int. Symp. Electromagn. Compat.* (Zürich, Switzerland), March 1993, pp. 127-132.
- [Lan81] N. H. Langton, "The parallel-plate capacitor with symmetrically placed unequal plates," *J. Electrostatics*, vol. 9, pp. 289-305, 1981.
- [Ler96] E. Leroux, S. Caniggia, F. Canavero, and B. Demoulin, "Evaluation of radiated emissions from printed circuit boards and cables at post-layout level," in *Proc. EMC'96 Roma* (Rome, Italy), vol. 2, Sept. 1996, pp. 662-667.
- [Lin85] W. Lin, "Computation of the parallel-plate capacitor with symmetrically placed unequal plates," *IEEE Trans. Microwave Theory Tech.*, vol. MTT-33, no. 9, pp. 800-807, Sept. 1985.
- [Lip80] W. Lipinski, M. Gramz, and P. Krasen, "Ein Beitrag zur Berechnung der Stromverdrängung in einem Bandleiter," *Arch. Electrotech.*, vol. 62, pp. 51-55, 1980.
- [Lov23] A. E. H. Love, "Some electrostatic distributions in two dimensions," *Proc. London Math. Soc.*, Ser. 2, vol. 22, no. 1460, pp. 337-369, 1923.
- [Max00] J. C. Maxwell, "On the induction of electric currents in an infinite plane sheet of uniform conductivity," *Proc. Royal Soc. (London)*, vol. 20, pp. 160-188, Feb. 1872.
- [Nak89] T. Nakamura, K. Oda, and S. Yokokawa, "Equivalent transmission lines of wire antennas and the radiation mechanism," *Electron. Commun. Jpn.*, vol. 72, no. 8, pp. 85-94, 1989.
- [Nak95] T. Nakamura, N. Hayashi, H. Fukuda and S. Yokokawa, "Radiation from the transmission line with an acute bend," *IEEE Trans. Electromagn. Compat.*, vol. EMC-37, no. 3, pp. 317-325, Aug. 1995.
- [Oei94] S. Öing, W. John, and F. Sabath, "Computation of common mode radiation due to asymmetric coupling on printed circuit boards," in *EMC 1994 12th Int. Wroclaw Symp. Electromagn. Compat.*, (Wroclaw, Poland), June/July 1994, pp. 554-558.
- [Ols74] R. G. Olsen, *Electromagnetic Characteristics of Horizontal and Vertical Wires above a Dissipative Earth*, Ph. D. thesis University of Colorado, 1974.
- [Oly95] F. Olyslager and D. De Zutter, "High-frequency transmission line models for a thin wire above a conducting ground," *IEEE Trans. Electromagn. Compat.*, vol. EMC-37, no. 2, pp. 234-240, May 1995.
- [Osu97] C. B. O'Sullivan and M. Musladin, "Investigation of the effectiveness of DC power bus interplane capacitance in reducing radiated EMI from multi-layer PCBs," in *Proc. 1997 IEEE Int. Symp. Electromagn. Compat.* (Austin, TX, USA), Aug. 1997, pp. 293-297.
- [Ott79] H. W. Ott, "Ground – A path for current flow," in *Proc. 1979 IEEE Int. Symp. Electromagn. Compat.* (San Diego, CA, USA), Oct. 1979, pp. 167-170.
- [Ott85] H. W. Ott, "Controlling EMI by proper wiring board layout," in *Proc. 6th Int. Symp. Electromagn. Compat.* (Zürich, Switzerland), March 1985, pp. 127-132.
- [Ott88] H. W. Ott, *Noise Reduction Techniques in Electronic Systems*, 2nd ed., New York: Wiley, 1988.
- [Pau89] C. R. Paul, "A comparison of the contributions of common-mode and differential-mode currents in radiated emissions," *IEEE Trans. Electromagn. Compat.*, vol. EMC-31, no. 2, pp. 189-193, May 1989.
- [Pau92a] C. R. Paul, *Introduction to Electromagnetic Compatibility*, New York: Wiley, 1992.
- [Pau92b] C. R. Paul, "Effectiveness of multiple decoupling capacitors," *IEEE Trans. Electromagn. Compat.*, vol. EMC-34, no. 2, pp. 130-133, May 1992.
- [Puc68] R. A. Pucel, D. J. Massé, and C. P. Hartwig, "Losses in microstrip," *IEEE Trans. Microwave Theory Tech.*, vol. MTT-16, no. 6, pp. 342-350, June 1968. Correction in *IEEE Trans. Microwave Theory Tech.*, vol. MTT-16, no. 12, p. 1064, Dec. 1968.
- [Put97] P. H. A. van der Putten and J. P. M. Voeten, *Specification of Reactive Hardware/Software Systems: The Method Software/Hardware Engineering (SHE)*, Ph. D. thesis Eindhoven University of Technology, 1997.
- [Ram94] S. Ramo, J. R. Whinnery, and T. Van Duzer, *Fields and Waves in Communication Electronics*, 3rd ed., New York: Wiley, 1994.
- [Rue74] A. E. Ruehli, "Equivalent circuit models for three-dimensional multiconductor systems," *IEEE Trans. Microwave Theory Tech.*, vol. MTT-22, no. 3, pp. 216-221, March 1974.

- [Sch34] S. A. Schelkunoff, "The electromagnetic theory of coaxial transmission lines and cylindrical sheets," *Bell Syst. Tech. J.*, vol. 13, pp. 532-579, 1934
- [Ses71] S. R. Seshadri, *Fundamentals of Transmission Lines and Electromagnetic Fields*, Massachusetts: Addison-Wesley, 1971.
- [Smi85] C. E. Smith and R.-S. Chang, "Microstrip transmission line with finite-width dielectric and ground plane," *IEEE Trans. Microwave Theory Tech.*, vol. MTT-33, no. 9, pp. 835-839, Sept. 1985.
- [Swa90] A. J. G. Swainson, "Radiated emission, susceptibility and crosstalk control on ground plane printed circuit boards," in *Proc. Inst. Elec. Eng. 1990 EMC Symp.* (York, England), Aug. 1990, pp. 37-41.
- [Sze89] B. Szentkuti, "Give up radiation testing in favour of conduction testing!," in *Proc. 8th Int. Symp. Electromagn. Compat.* (Zürich, Switzerland), March 1989, pp. 221-226.
- [Sze92] B. T. Szentkuti, "Shielding quality of cables and connectors: Some basics for better understanding of test methods," in *Proc. 1992 IEEE Int. Symp. Electromagn. Compat.* (Anaheim, CA, USA), Aug. 1992, pp. 294-301.
- [Tay92] C. D. Taylor and C. W. Harrison, Jr., "On the coupling of microwave radiation to wire structures," *IEEE Trans. Electromagn. Compat.*, vol. EMC-34, no. 3, pp. 183-188, Aug. 1992.
- [Tes97] F. M. Tesche, M. V. Ianoz, and T. Karlsson, *EMC Analysis Methods and Computational Models*, New York: Wiley, 1997.
- [Tik90] A. N. Tikhonov and A. A. Samarskii, *Equations of Mathematical Physics*, New York: Dover, 1990.
- [Tro96] D. H. Trout, "Investigation of the bulk current injection technique by comparison to induced currents from radiated electromagnetic fields," in *Proc. 1996 IEEE Int. Symp. Electromagn. Compat.* (Santa Clara, CA, USA), Aug. 1996, pp. 412-417.
- [Van78] E. F. Vance, *Coupling to Shielded Cables*, Chichester: Wiley-Interscience, 1978.
- [Ven85] J. Venkataraman, S. M. Rao, A. R. Djordjević, T. K. Sarkar, and Y. Naiheng, "Analysis of arbitrarily oriented microstrip transmission lines in arbitrarily shaped dielectric media over a finite ground plane," *IEEE Trans. Microwave Theory Tech.*, vol. MTT-33, no. 10, pp. 952-959, Sept. 1985.
- [Web65] E. Weber, *Electromagnetic Theory.*, New York: Dover, 1965.
- [Wed78] L. M. Wedepohl and A. E. Efthymiadis, "Wave propagation in transmission lines over lossy ground: A new, complete field solution," *Proc. Inst. Electr. Eng.*, vol. 125, no. 6, pp. 505-510, June 1978.
- [Wil96] T. Williams, *EMC for Product Designers*, 2nd. ed., Oxford: Butterworth-Heinemann, 1996.
- [Wis31] W. H. Wise, "Effect of ground permeability on ground return conductors," *Bell Syst. Tech. J.*, vol. 10, pp. 472-484, 1931.
- [Zut97] D. De Zutter, "The FDTD-method for EMC-problems with application to electrostatic discharge and delta-*I* noise calculations," in *Proc. 1997 IEEE Int. Symp. Electromagn. Compat.* (Austin, TX, USA), Aug. 1997, pp. 226-230.

## List of symbols

| Symbol  | Unit          | Meaning   |
|---|---------------|---|
| $\mathbb{C}$  | —             | complex domain or complex number  |
| $\mathbb{R}^m$  | —             | $m$ th dimensional real domain; $m > 0$   |
| $\alpha_1$  | rad           | principal value of the argument of $t_1$  |
| $\beta$   | 1/m           | constant in ‘thin plate limit’; $\beta = \omega\mu_0/2R_\square$                        |
| $\gamma$  | 1/m           | propagation constant  |
| $\gamma_e$  | —             | Euler’s constant; $\gamma_e = 0.57721 \dots$  |
| $\delta$  | m             | skin depth; $\delta = \sqrt{2/\omega\mu_0\sigma}$                                       |
| $\Delta i$  | A             | amplitude of trapezoidal-waveform current   |
| $\Delta i_f, \Delta i_r$  | A             | amplitudes of triangular-waveform current   |
| $\Delta M_s$  | H/m           | mutual-induction correction in CM-DM coupling   |
| $\Delta v$  | —             | correction term   |
| $\varepsilon_0$   | F/m           | dielectric permittivity; $\varepsilon_0 = 8.854187 \cdot 10^{-12} = 1/\mu_0 c_0^2$      |
| $\varepsilon_r, \varepsilon_{r0}, \varepsilon_{rl,i}, \varepsilon_{rr,i}$ | —             | relative dielectric constants   |
| $\zeta_j$   | V             | mismatch measure along dielectric segment $S_j$   |
| $\eta$  | $\Omega$      | free-wave impedance; $\eta = 120\pi$  |
| $\eta_j$  | V             | mismatch measure along conductor segment  |
| $\lambda$   | m             | wave length   |
| $\lambda_f$   | 1/m           | parameter in Fredholm integral equation; $\lambda = j\omega\mu_0/2\pi R_\square$        |
| $\mu$   | H/m           | total permeability; $\mu = \mu_0\mu_r$  |
| $\mu_0$   | H/m           | permeability of vacuum; $\mu_0 = 4\pi \cdot 10^{-7}$                                    |
| $\mu_r$   | —             | relative permeability   |
| $\xi$   | 1/m           | term in Fourier integrals; $\xi = \sqrt{\alpha^2 + j\omega\mu\sigma}$                   |
| $\rho$  | m             | position vector of the observation point $(x, y) \in \mathbb{R}^2$                      |
| $\rho^\pm$  | m             | position vector inside (+)/outside (−) a 2D structure                                   |
| $\sigma, \sigma_t$  | 1/ $\Omega$ m | conductivity; $\sigma = 5.8 \cdot 10^7$ (copper) and $\sigma = 1.43 \cdot 10^7$ (brass) |
| $\sigma_F$  | C/m           | free-charge density   |
| $\sigma_{Fi}$   | C/m           | uniform free-charge density of segment $S_i$  |
| $\sigma_T$  | C/m           | total single-layer charge-density   |
| $\sigma_{Ti}$   | C/m           | uniform single-layer charge-density of segment $S_i$                                    |
| $\tau$  | s             | rise/fall time of current waveform  |
| $\phi$  | rad           | angular position in the complex domain  |
| $\phi_2$  | rad           | angular position of a transformed wire  |
| $\phi(\cdot), \phi_+(\cdot), \phi_-(\cdot)$                               | A             | expansion functions in the Fourier-integral integrand                                   |
| $\varphi$   | rad           | angle   |
| $\Phi, \Phi_e$  | Vs            | total flux through a surface bounded by a contour $\Gamma$                              |
| $\Phi_1, \Phi_a, \Phi_{GP}$   | Vs/m          | flux per unit length  |
| $\Phi(\cdot)$   | —             | complex potential   |
| $\psi(z)$   | —             | complex potential at $z \in \mathbb{C}$ due to a line charge                            |



|   |       |   |
|---|-------|---|
| $\psi_i(z)$   | —     | potential due to a constant single-layer density along a segment $S_i$  |
| $\psi(\cdot), \phi_+(\cdot), \phi_-(\cdot)$         | A     | expansion functions in vector potential $A_z$                           |
| $\Psi$  | —     | $\Psi$ -function  |
| $\Psi(\cdot)$                                       | —     | imaginary part of complex function $\Omega(\cdot)$                      |
| $\mathbf{\Psi}, \mathbf{\Psi_d}$                    | —     | matrices of discretized boundary value problem                          |
| $\omega, \omega_0$                                  | rad/s | angular frequencies   |
| $\Omega(\cdot)$                                     | —     | complex potential   |
| $\Omega^*(\cdot)$                                   | —     | conjugate complex potential $\Omega$                                    |
| $\nabla_z V$  | —     | gradient in $z$ -direction of the scalar function $V$                   |
| 2D  | —     | two dimensional   |
| 3D  | —     | three dimensional   |
| $a$   | —     | fraction of current returning through two ground planes                 |
| $a$   | —     | constant; $a = 2/\ln(4/\pi)$  |
| $a, \dots, d$                                       | —     | orthogonal tracks for PCB with bends                                    |
| $A_1$   | —     | field amplification for tube above a large plate                        |
| $A_2, A'_2$   | —     | ‘Kamin Dämpfung’ (chimney attenuation)                                  |
| $A_z, A_z^{(s)}, A_z^{(1)}$                         | Vs/m  | vector potential in $z$ -direction; per unit length                     |
| $b$   | m     | dimension of current sensor   |
| $b, b_1, b_2$                                       | m     | widths of a PCB tracks  |
| $B$   | —     | bounded set   |
| $c$   | A/m   | constant in Fredholm equation; $c = -\nabla_z V/R_\square$              |
| $c_0$   | m/s   | velocity of light in vacuum; $c_0 = 2.997925 \cdot 10^8$                |
| $c_i$   | —     | $i$ th coefficient in $\Delta v$ expansion                              |
| CM  | —     | Common Mode   |
| CP  | —     | Cabinet Panel   |
| $C, C_k$  | —     | (closed) countour in complex domain                                     |
| $C_g$   | F/m   | gap capacitance   |
| $C_i$   | F     | capacitance   |
| $C_1, C_s$  | F/m   | self capacitances of microstrip lines                                   |
| $C_{12}, C_{12,0},$                                 |       |   |
| $C_{CM}$  | F/m   | self capacitance of the CM circuit                                      |
| $\mathbf{C}, \mathbf{C_0}, \mathbf{C^*}$            | F/m   | capacitance matrix  |
| $d$   | m     | dimension of current sensor   |
| $d, d_p, d_t$                                       | m     | thickness   |
| DM  | —     | Differential Mode   |
| $D_{n,i}^j, D_{nl,j}, D_{nr,j}$                     | C/m   | normal electric flux density in $\mathbb{C}$                            |
| $\mathbf{D}$  | C/m   | electric flux density vector  |
| $E$   | V/m   | 2D electric field $\mathbf{E} = (E_x, E_y)$ represented in $\mathbb{C}$ |
| Ei  | —     | exponential integral  |
| $E_n, E_{nt,j}, E_{n,i}^j,$<br>$E_{nl,i}, E_{nr,i}$ | V/m   | normal electrical field in $\mathbb{C}$                                 |
| $E_{tan}, E_{tan,i}^j$                              | V/m   | tagential electric field in $\mathbb{C}$                                |
| $E_x, E_y, E_z$                                     | V/m   | $x, y,$ and $z$ component of $\mathbf{E}$ vector, respectively          |
| $\mathbf{E}$  | V/m   | 3D electric field strength; $\mathbf{E} = (E_x, E_y, E_z)$              |
| $f, f_0$  | Hz    | frequency   |
| $f_0$   | Hz    | fundamental frequency of a periodic signal                              |

|  |                  |  |
|--|------------------|--|
| $f_c, f_{cs}$  | Hz               | cross-over frequencies   |
| $f_{rDM}, f_{rCM}$                                     | Hz               | resonance frequency in DM and CM circuit   |
| $f(\cdot)$   | A/m              | excitation function in Fredholm equation   |
| $F, F_+, F_-, F_{1+},$<br>$F_{1-}, F_{2+}, F_{2-}$     | V/m              | expansion functions in the Fourier-integral integrand                                  |
| $g$  | m                | gap distance   |
| GP   | —                | Ground Plane   |
| $h$  | m                | height of sensor   |
| $h, h_1, h_2$  | m                | height of track above GP   |
| $h_t, h_{PP}$  | m                | height   |
| $h_{CP}$   | m                | height of ground plane above CP  |
| $H_e, H_\perp$   | A/m              | magnetic field strength  |
| $H(\cdot)$   | —                | transfer function  |
| $\mathbf{H}, \mathbf{H}_1, \mathbf{H}_2, \mathbf{H}_3$ | A/m              | 3D magnetic field strength   |
| $i_{CM}$   | A                | common-mode current in time domain   |
| $i_{DM}$   | A                | differential-mode current in time domain   |
| $I, I_s, I_t$  | A                | current  |
| $I_1, I_2, I_{inj}$                                    | A                | injected current in a PCB track  |
| $I_m^{CM}$   | A                | $n$ th expansion coefficient of the periodic CM current                                |
| $I_{DM}^m$   | A                | measured current with current sensor $s$   |
| $I_n^{DM}$   | A                | $n$ th expansion coefficient of the DM trapezoidal-waveform current                    |
| $I_{CM}$   | A                | common-mode current in frequency domain  |
| $I_{DM}$   | A                | differential-mode current  |
| $j$  | —                | solution of the equation $j^2 + 1 = 0$   |
| $J_z$  | A/m <sup>2</sup> | current density in $z$ direction   |
| $k$  | 1/m              | damped wave-propagation constant in vacuum; $k = (1 + j)/\delta$                       |
| $k, k'$  | —                | moduli in elliptic integrals; $k' = \sqrt{1 - k^2}$                                    |
| $k_i$  | —                | segment number $S_i$ ; $i = 1 \cdots k_t$  |
| $k_t$  | —                | total number of segments   |
| $K, K', K_1, K_2$                                      | —                | arbitrary positive constants   |
| $K(k), K(k')$  | —                | complete elliptic integrals of the first kind with modulus $k$ and $k'$ , respectively |
| $K_z$  | A/m              | sheet current density in $z$ direction   |
| $\ell, \ell_t, l_i, l_t$                               | m                | length   |
| $l_1, l_2$   | m                | dimensions of current sensor   |
| $L, L_s$   | H                | inductance   |
| $L_s$  | H/m              | self inductance of a microstrip line   |
| $L_{CM}$   | H/m              | self inductance of the CM circuit  |
| $\mathbf{L}, \mathbf{L}^*$                             | H/m              | inductance matrices  |
| $m$  | —                | parameter; $m = k^2$   |
| $M$  | H                | total mutual inductance  |
| $M_1, M_2, M_h$  | H                | mutual inductances of a hole in a tube   |
| $M_c, M_g, M_m$  | H/m              | mutual inductance of a track to a CM circuit   |
| $M_{ng}, M_s, M_t$                                     |                  |  |
| $M_{sens}$   | H                | mutual inductance of sensor $s$  |
| $n$  | —                | number of dielectric segments  |

|                               |                    |   |
|-------------------------------|--------------------|---|
| $n, n_j$                      | m                  | complex representation of the normal $\mathbf{n}, \mathbf{n}_j$ vectors |
| $\mathbf{n}, \mathbf{n}_j$    | m                  | outward unit normal vector in $\mathbb{C}$                              |
| $N$                           | —                  | total number of unknowns  |
| $N_c, N_d$                    | —                  | number of conductor/dielectric segments                                 |
| $q, Q, Q_1, Q_2, Q_{GP}$      | C/m                | charge; per unit length   |
| $r_h, r_i, r_o$               | m                  | radius of circular structure  |
| $R$                           | $\Omega$           | characteristic termination; $R = 50 \Omega$                             |
| $R$                           | m                  | radius of a large cylinder  |
| $R_0$                         | $\Omega$           | termination of CM circuit; $R_0 = 150 \Omega$                           |
| $R_{CM}$                      | $\Omega/\text{m}$  | series resistance of GP and CP  |
| $R_{DC}$                      | $\Omega$           | d.c. resistance   |
| $R_{DC}$                      | $\Omega/\text{m}$  | d.c. resistance of the microstrip line                                  |
| $R_{GP}$                      | $\Omega/\text{m}$  | resistance of ground plane; per unit length                             |
| $R_s$                         | $\Omega/\text{m}$  | skin-effect resistance of the microstrip line                           |
| $R_t$                         | $\Omega$           | resistance of tube  |
| $R_{\square}$                 | $\Omega$           | sheet resistance; $R_{\square} = 1/\sigma d$                            |
| $s$                           | m                  | distance between two tracks   |
| $s$                           | —                  | currents sensor on digital board  |
| $s, s_0, s_1, s_1^{inv}, s_2$ | —                  | complex numbers   |
| $s_{ij}, S_{ij}$              | —                  | S-parameters  |
| $S_i$                         | m                  | straight segment in $\mathbb{C}$  |
| $t$                           | m                  | thickness   |
| $t, t_1$                      | —                  | complex numbers   |
| $t_r, t_f, t_r^*, t_f^*$      | s                  | rise and fall times of current waveforms                                |
| $u$                           | —                  | complex number  |
| $u, u_j$                      | m                  | complex representation of the normal $\mathbf{u}, \mathbf{u}_j$ vectors |
| $v, v_1$                      | —                  | complex numbers   |
| $v^{ind}$                     | V                  | induced CM voltage in time domain                                       |
| $V_{CM}$                      | V                  | common-mode voltage   |
| $V_{DM}, V_{DMj}$             | V                  | differential-mode voltage   |
| $V_g, V_s, V_{sj}, V_{sens}$  | V                  | voltage   |
| $V_1, V_2, V_3$               |                    |   |
| $x$                           | m                  | cartesian coordinate  |
| $x_1, x_2$                    | m                  | $x$ position of tracks  |
| $x_s$                         | m                  | $x$ postion of sensing wire   |
| $x^*$                         | m                  | reference position  |
| $X(\cdot)$                    | —                  | real part of complex potential $\Omega(\cdot)$                          |
| $y$                           | m                  | cartesian coordinate  |
| $y_s$                         | m                  | $y$ postion of sensing wire   |
| $\mathbf{Y}$                  | $1/\Omega\text{m}$ | admittance matrix   |
| $Y_t$                         | $1/\Omega\text{m}$ | transfer admittance   |
| $z$                           | m                  | cartesian coordinate  |
| $z, z_1, z_2$                 | —                  | complex numbers   |
| $z_i, z_{i+1}$                | —                  | corners in $\mathbb{C}$ of segment $S_i$                                |
| $z_{mi}$                      | —                  | collocation point at segment $S_i$ ; $z_{mi} = (z_i + z_{i+1})/2$       |
| $\mathbf{Z}$                  | $\Omega/\text{m}$  | impedance matrix  |
| $Z(\cdot)$                    | —                  | Jacobi's Zeta-function  |

|                     |                   |  |
|---------------------|-------------------|--|
| $Z_0$               | $\Omega$          | characteristic impedance                                     |
| $Z_{0m}$            | $\Omega$          | characteristic impedance of track above a wide plane         |
| $Z_{Ai}, Z_{Bi}$    | $\Omega$          | termination impedances                                       |
| $Z_{CM}$            | $\Omega$          | total impedance of CM circuit                                |
| $Z_{CM}$            | $\Omega/\text{m}$ | impedance of CM circuit; per unit length                     |
| $Z_g$               | $\Omega$          | generator input-impedance                                    |
| $Z_{ij}$            | $\Omega$          | $Z$ parameters   |
| $Z_{in}$            | $\Omega$          | input impedance  |
| $Z_m$               | $\Omega$          | characteristic impedance of microstrip line                  |
| $Z_s$               | $\Omega/\text{m}$ | series impedance of microstrip line                          |
| $Z_t$               | $\Omega/\text{m}$ | per unit length transfer impedance                           |
| $\mathbf{Z}_t$      | $\Omega/\text{m}$ | $Z_t$ matrix with zeros on diagonal                          |
| $Z_t(1-2)$          | $\Omega/\text{m}$ | transfer impedance between circuits 1 and 2                  |
| $Z_t(1-2,c)$        | $\Omega/\text{m}$ | $Z_t$ between DM circuits 1 and 2 with closed CM circuit     |
| $Z_t(1-2,o)$        | $\Omega/\text{m}$ | $Z_t$ between DM circuits 1 and 2 with opened CM circuit     |
| $Z_t(\text{CM-DM})$ | $\Omega/\text{m}$ | $Z_t$ between DM and CM circuit                              |
| $Z_t(\text{DM-CM})$ | $\Omega/\text{m}$ | $Z_t$ between DM and CM circuit                              |
| $Z_t(i\text{-CM})$  | $\Omega/\text{m}$ | transfer impedance between circuits $i$ and CM               |
| $Z_T$               | $\Omega$          | transfer impedance   |
| $Z_T(i-j)$          | $\Omega$          | transfer impedance between circuits $i$ and $j$ ; $i \neq j$ |
| $Z_T(\text{DM-CM})$ | $\Omega$          | $Z_T$ between DM and CM circuit                              |



# Acknowledgement

One of the first pages read by many people is probably this one, even though I put it on the end. Those who have read this thesis, or just parts of it, will appreciate that it is almost impossible to complete this work by my own in approximately four years without help of many other people.

First of all I would like to thank all present and past members of our High-Voltage and EMC group. I especially appreciate all contributions made by my coach and copromotor Lex van Deursen. His enthusiastic approach and critical look at both the models and the measurements helped me to acquire much experience and insight. The ‘open door’ policy and the attentively listening of my professor and first promotor Piet van der Laan was encouraging. His physical insight and observations stimulated me in the discussions we had.

Most of the practical technical work was carried out by Peter Bruins, whose skills were indispensable and whose happy attitude was a real pleasure. I also thank ‘pulsed corona’ Erwin Smulders for his practical contributions in the last part of my work. The start of a working day with strong 8 o’clock coffee and a chat with Peter and Erwin was a good beginning.

Our practically oriented group seems to be attractive to students, among them were Ewald van Dorst, Anthonie Kaland, Peter van der Wielen, and Harm Zwier; they all did a ‘hell’ of a job by carrying out many of the measurements. I would like to thank them for their work.

Further, I appreciate the stimulating discussions with and valuable suggestions of Jos Bergervoet from Philips Research Laboratories. The initial work by Ben Paagman from Berg Electronics led to the test setup of Chapter 2; I hope someday the ‘world’ will value our simple setup. A lot of other people contributed in some way to this thesis, among them were Mart Coenen and Stef Worm of Philips and the members of the Dutch Technology Foundation (STW) utilization committee, in particular dr. P.A. Beeckman and dr. J.J. Goedbloed (Philips Research Laboratories), dr. S. Öing and dr. W. Rissiek (INCASES Engineering GmbH), and dr.ir. H.W. Piekaar (STW).

Finally, I would like to thank all my colleagues who regularly visited our morning and afternoon coffee breaks. This also holds for Paul Blom who was for a few years my roommate at the university.



## Curriculum vitae

Frank van Horck was born on March 30, 1967 in Grubbenvorst. In 1973 he went to the Roman Catholic primary school “De Bottel” in Lottum. From 1979 to 1983 he followed secondary education at “MAVO De Bisweide” in Grubbenvorst. In 1983 he began his electrotechnical education at the MTS in Venlo and went in 1987 to the HTS, also in Venlo. In 1991 he began to study at the Eindhoven University of Technology. In April 1994 he obtained his M.Sc. degree *cum laude* in the High-Voltage and EMC group of prof. P.C.T. van der Laan. During the next five months of research work in the same group, he developed the connector measuring setup presented in Chapter 2. In October 1994 he began his investigations on EMC and printed circuit boards funded by the Dutch Technology Foundation (STW), which led to this Ph.D. thesis.





STELLINGEN

behorende bij het proefschrift

# **Electromagnetic Compatibility and Printed Circuit Boards**

door

Frank B.M. van Horck

4 juni 1998

1. De stroomverdeling in een dun aardvlak van eindige breedte heeft een gecompliceerd verloop voor hoge frequenties. Een onschuldige lijkende benadering van deze stroomverdeling bij het berekenen van twee-dimensionale velden blijkt te resulteren in significante afwijkingen in koppelingsparameters.

D. M. Hockanson *et al.*, “Quantifying EMI resulting from finite-impedance reference planes,” *IEEE Trans. Electromagn. Compat.*, vol. EMC-39, no. 4, pp. 286-297, Nov. 1997.

2. De berekende resonanties in het differential-mode (DM) circuit moeten goed overeenstemmen met de werkelijke resonanties, anders is het niet zinvol om voor die frequenties de koppeling met de omgeving te berekenen.

Dit proefschrift, hoofdstuk 3.

3. De uitspraak “radiation tests have even worse correlation to radiation tests” door Szentkuti geeft treffend de grote invloed van bekabeling op de totale straling van een apparaat weer.

Storingen van een apparaat meet men volgens de norm met een antenne op 3, 10 of zelfs 30 m afstand. Een analogie: de automonteur kijkt met een verrekijker onder de motorkap. Daarmee blijven de handen schoon maar de problemen onopgelost.

B. Szentkuti, “Give up radiation testing in favour of conduction testing!,” in *Proc. 8th Int. Symp. Electromagn. Compat.* (Zürich, Switzerland), March 1989, pp. 221-226.

4. Aangezien stromen *altijd* in gesloten lussen lopen, is het fysisch gezien onjuist om aan *één* geleider of *één* aardvlak een (partiële) zelfinductie toe te kennen.

Dit proefschrift, hoofdstuk 3.

5. De huidige programmatuur voor EMC analyse tijdens de layout-fase van een printplaat is te ingewikkeld voor praktische toepassingen.

6. Volgens Smolders zal het vakgebied Elektromagnetisme ook in de computertechniek een steeds belangrijkere rol gaan spelen indien de trend om steeds hogere klokfrequenties te gebruiken zich voortzet. Niet alleen voor de hier bedoelde “signal integrity” maar ook zeker voor de EMC van de bedoelde schakelingen is het essentieel om het vakgebied Elektromagnetisme te begrijpen en te kunnen toepassen, voor vele frequenties.

Stelling 3 bij proefschrift van A. B. Smolders, *Microstrip Phased-Array Antennas: A Finite-Array Approach*, Ph. D. thesis Eindhoven University of Technology, 1994.

7. De stortvloed van gereviseerde computerprogramma's met nog meer toeters en bellen lijkt niet te stoppen. De meeste gebruikers zitten echter niet te wachten op de minder essentiële utilities met bijbehorende fouten, wanneer de huidige versie van een programma met zijn bekende onvolmaaktheden voldoet.
8. Ondanks de informatisering van onze huidige maatschappij zal het sociale aspect van de samenleving belangrijk blijven.
9. Verdergaande flexibilisering van de arbeid zal een negatieve invloed hebben op kennis-intensieve bedrijven.
10. De politiek staat te ver af van de burgers, aldus een veel gehoorde stelling van politici. Een voorstel voor de oplossing van dit probleem is het districtenstelsel:  $\frac{2}{3}$  van de 150 tweede kamerleden worden verkozen uit hun district en  $\frac{1}{3}$  van de leden via landelijke lijsten. Dit voorstel zal waarschijnlijk niet veel effect hebben, gezien het laagterecord van de opkomst voor de gemeenteraadsverkiezingen afgelopen maart.

J. A. van Schagen, “Het personele element in ons kiesstelsel moet sterker,” *NRC Handelsblad*, 11 Maart 1998.

11. Fietsvriendelijke verkeerslichten (hoewel stoplichten meestal een beter woord is) in steden zullen het gebruik van de fiets stimuleren.
12. Het IQ van een “meedenkende” kopieermachine heeft een verdacht lage waarde: regelmatig neemt zo'n machine de onjuiste beslissing.